Prediction of Temperature Distribution in a Drinking Water Network

Delft University of Technology
Faculty of Civil Engineering and Geosciences
Department of Water Management
Section of Water Resources Management
Stevinweg 1
2628 CN Delft
The Netherlands

www.citg.tudelft.nl

Lucyna Magda

Prediction of Temperature Distribution in a Drinking Water Network

Lucyna Magda

June 2010

TU Delft Delft University of Technology

waternet

Challenge the future

Delft University of Technology

Faculty of Civil Engineering and Geosciences
Department of Water Management
Section Water Resources

Prediction of Temperature Distribution in a Drinking Water Network

Master of Science Thesis in Civil Engineering

Lucyna Magda
June 2010

Members of the Graduation Committee:

Prof.dr.ir. Nick van de Giesen	Delft University of Technology Chair of the Water Resources Section
Prof.dr.ir. Luuk Rietveld	Delft University of Technology Sanitary Engineering Section
Ir. Martine Rutten	Delft University of Technology Water Resources Section
Dr. Marco Dignum	Waternet Research and Development Section
Drs.ing. Sonja Viester	Waternet Research and Development Section

Abstract

According to the Dutch Drinking Water Directive the temperature of drinking water should remain below 25°C at the customers' taps to prevent microorganisms proliferating in the distribution mains and to ensure a supply of water that is qualitatively and aesthetically stable. However, the water temperature in a distribution network is difficult to control as it depends on multiple factors including: climatic conditions, surface conditions, soil characteristics and drinking water discharges.

Recent studies demonstrate that the rising global mean temperatures as projected by the International Panel on Climate Change are likely to be manifested in an increase of the temperature of the surface water systems and of the soil. Therefore, it is likely that also the temperature of drinking water will increase and drinking water supply companies may find themselves in a situation of temperatures approaching legally imposed standards.

The principal goal of this research was to explore how network hydraulic influences the temperature of the drinking water. The secondary aim was to establish linkages between climate conditions, network characteristics and the drinking water temperature. To achieve these goals, we have used a model instrument consisting of two heat transfer models representing weather and soil conditions, and two network models calculating hydraulics and water quality. In order to validate the models' an experiment was organised. An experiment was conducted to observe the soil at the three different depths below the surface simultaneously with the drinking water temperature. The observation unit was repeated at four different locations in a network, that featured different surface covers and pipe characteristics.

The evaluation of a capability of a combined weather and soil-diffusion models to estimate pipe wall temperatures has led to inaccurate results; however the models we have used carried useful information for network calculations. Secondly, numerical network simulations at the heat wave conditions, indicate importance of the residence time and gradient between the soil and drinking water temperatures. However results from this case study

demonstrated that the gradient between the soil, pipe wall and the drinking water, during the measuring period (autumn-winter), was small. It was difficult to determine a clear influence of the hydraulic on the diurnal cycle of the drinking water-soil temperature exchange.

This study proved an applicability of the model instrument to predict a temperature of the drinking water. However, heat transfer modelling approach requires additional improvements towards models' accuracy, and an account of precipitation and soil moisture. The reliability of the methodology used in this thesis, should be verified for summer conditions when the air, net global radiation and soil temperature exhibit stronger diurnal fluctuations.

To obtain information on a large-scale network variability local or point measurements should be contrasted with groundwater, soil temperatures and surface conditions (GIS analysis). Drinking water companies, in order to address the overheating problem, should start to monitor water temperature near the small diameter pipes at the peripheral parts of a network which, seemingly, are most vulnerable to extraneous heat surges.

Acknowledgements

Over the last year it has been my good fortune to encounter many people from Waternet who have contributed greatly to the content of this work. I would first of all like to thank Prof Luuk Rietveld and Joost Kappelhof, who where both initiators of this thesis and my primary supervisors in the early stage, for giving me the opportunity to follow this research. I greatly appreciate the support of Waternet, which facilitated this research financially, for agreeing and utilising the experiment in Diemen Noord. I would like to thank my project co-workers and supervisors from Waternet: Eric Baars, Marco Dignum, Sonja Viester for their unique brand of enthusiasm, supervision and support when encouragement was needed. Sonja, thanks to you I have never been without a desk, a computer and a friendly ear. Arne Bosh and Ralf de Groot, thank you for tutoring, correcting and advising me in my hydraulic calculations. I would like to thank Prof Theo Olsthoorn and Frank Smits for sharing their excellent modelling skills with me and for being interested in the course and a good end of this research.

Many thanks to Prof Nick van de Giesen and Martine Rutten, from the Water Resources Section at Delft University of Technology, for the scientific support and ideas that form the bedrock on which much of this thesis was built. Special thanks to Jan Vreeburg for introducing me to Mirjam Blokker and Mirjam Blokker herself, whose work and advise have been instrumental in the modelling part of this thesis, for giving me more of her time, professional help, and above all: patience.

Moving towards more personal acknowledgements, I would like to thank my parents, family and Matteo Fiori, for constant support. My special gratitude goes to four of my friends, who made great efforts to proof read parts of this text: Robin Harder, Tina Laparidou, and Marnix Maas.

Finally, I would like to acknowledge my co-students and dispuut members, that I have worked, talked, and lunched with over the three years while I was pursuing a Master degree at Water Resources at Delft University of Technology.

Contents

1

Introduction

1.1 Drinking Water Temperature: a Problem?

Waternet [1] produces on average $26 \cdot 10^4 \mathrm{m}^3$ drinking water per day. One of the sources for drinking water is water from the dune area 'Amsterdamse Waterleidingduinen' at Leiduin, where pre-treated Rhine water is infiltrated. The second source is water from the Bethunepolder near Loosdrecht.

The treated water is distributed without using chlorine to more than a million clients (households and industries of Amsterdam and surrounding areas) in the distribution network with a total length of about $2000\mathrm{km}$.

Waternet verified that mainly the drinking water from the Bethunepolder, but also the water coming from Leiduin is subject to significant changes in temperature. During summer the distribution network encounters intensified formation of biofilm at the pipe walls and water quality problems, like an increased incidence of *Aeromonas*. It has been demonstrated that these problems are directly related to high temperatures of drinking water (see Figure 1.1). Biofilm formation on the drinking water pipe walls continuously deteriorates the water quality as the occasional abrupt changes in water flow can cause re-suspension of the sediment deposed on the biofilm, as a result of which viable bacteriae, such as coliform *Klebsiella*, chlorine resistant *Microbacterium* strains and heat tolerant *Legionella* can be released into the main flow of water (De Moel et al., 2006), (Geldreich, 1996).

To prevent microorganisms proliferating in the distribution mains and to ensure a supply of water that is qualitatively and aesthetically stable, the Dutch Drinking Water Directive (Waterleidingbesluit,

[1] Waternet is a company in the Netherlands that combines water services such as supply of drinking water, waste water, managing the surface water and safety behind the dykes around the Amsterdam area. Source: Waternet website: http://www.waternet.nl/. Retrieved: 19.03.2010

1960) prescribes the temperature of the water at the customers' taps below 25°C. However, the water temperature in a distribution network is difficult to control as it depends on an array of complex elements.

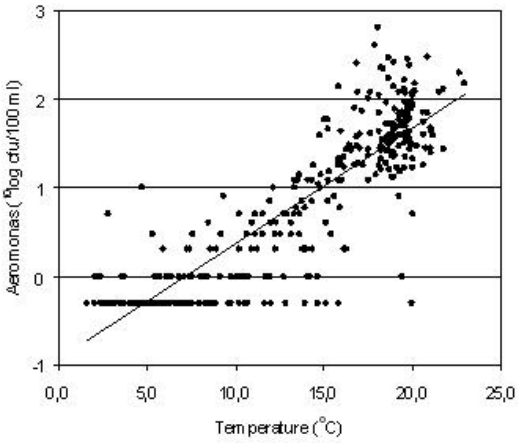

Figure 1.1: Correlation between *Aeromonas* counts and temperature; Weesperkarspel, Waternet. - The *Aeromonas* counts and temperature were registered at Weesperkarspel drinking water production station. Source: Waternet.

The distribution mains are buried in the soil[1], below the frost line[2], still the pipes are constantly influenced by the climatic conditions. The influence of the Urban Heat Island Effect[3] extends down beneath the frost line, and effectuates much stronger diffusive exchanges of heat between surface and deep soil layers (WMO, 2008). Cities that have been paved with impervious fabrics do not receive the benefit of natural cooling effects from vegetation (Akbari et al., 2001). Without virtually any cooling, the temperature of the soil at the pipe-wall may manifest long-duration amplifications which is reflected especially during persistent and extreme weather conditions. Groundwater temperature isotherms clearly reflect the inhomogeneous character of the subsurface temperatures (see Figure 1.2).

Van Der Molen et al. (2008) exemplified that one of the reasons for this situation is that the temperature at the pipes is easily phased with the soil temperature. As Van Der Molen et al. (2008) substantiated, heat-absorbing surface coverings, such as asphalt, intensify heat conduction from the upper to the lower

[1]Pipes in Amsterdam are buried at a depth of approximately 1 m, where the soil is mostly sandy. The groundwater level is around 50-90 cm below ground level, thus most pipes are situated below the groundwater table.

[2]Freezing depth is the depth to which the groundwater in soil is expected to freeze. The frost line depth depends on the location and the climate. Source: Wikipedia, the free encyclopaedia. Retrieved on 01.10.2009, from http://en.wikipedia.org/wiki/Frostline.

[3]An area of urban development which exists at a higher temperature than surrounding suburban and rural areas. The temperature difference, as much as 4°C, is manifested mainly at night and in cold weather. It is due in part to the wind protection afforded by buildings and in part to the heat emission from the surface and buildings (Slesser, 1982) (see Appendix 3).

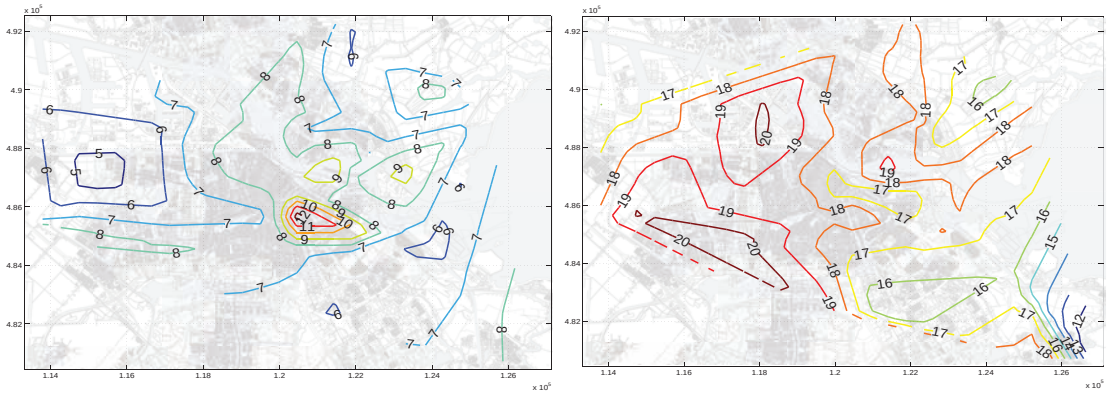

Figure 1.2: Isotherms interpolated from the groundwater temperatures measured with divers, sparsely deployed at around 2m depths in Amsterdam. Values are averaged for the period February-March 2009 (left picture) and August-September 2009 (right picture); (reported in [°C]).

soil layers as a result of temperatures at deep soil layers which increase fast especially during the heatwaves[1] or long summer periods.

Similarly, Blokker and Pieterse-Quirijns (2009) indicate, drinking water distribution practices influence greatly drinking water temperature, especially when the travel time of the drinking water from the production station to the customers' taps is much longer than the time needed for the drinking water to reach the soil temperature. Accordingly, in the network, where low demands and long residence times prevail, the temperature in the conveyed drinking water adopts quickly to the soil temperature.

Analysing the climate change projections (see Appendix 1 and (IPCC, 2007)) demonstrates convincingly that the rise in global mean temperatures is likely to be manifested in an increase of the temperature of the surface water systems, the soil and possible groundwater. Several publications (Schwartz, 2007); (De Graaf and Van De Ven, 2008), have reported that summery temperatures of the surface waters in the Netherlands, including sources for drinking water production, may rise by some 0.8 up to 2.8°C in the future. The trigger for the rise is a combined effect of a growing demand for electricity (Rutten, 2006) and increasing global mean temperatures (IPCC, 2007). Van Der Molen et al. (2008) and Zwolsman (2008) stipulate that the increased soil and surface temperatures will also cause an increase in the temperature of drinking water.

Several relevant findings and hypotheses revealed in the Van Der Molen et al. (2008) and Blokker and Pieterse-Quirijns (2009) articles form base of this research:

[1] Defined by KNMI, Royal Netherlands Meteorological Institute, as a period of 5 consecutive days where the air temperature exceeds 25°C.

(1) Relation between Soil and Drinking Water Temperature During experiment conducted for the purpose of Van Der Molen et al. (2008), it has been noted that measurements of the soil and the water temperature at the nearest pumping station were correlated (see Figure 1.3).

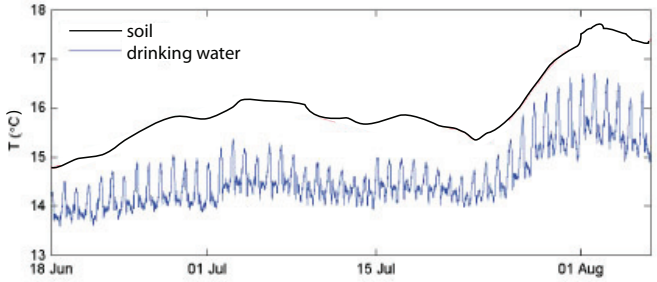

Figure 1.3: Comparison of measurements of the temperature in the soil and drinking water from the pumping station. - The black line represents the soil temperature, the blue line the drinking water temperature as measured at the pumping station. Source: (Van Der Molen et al., 2008).

(2) Sensitivity of Drinking Water Temperature to Hydraulics Van Der Molen et al. (2008) have observed, that during low flows, at nights, water temperature is almost equal to the soil temperature. It has been stipulated that the degree of warming up depends on the transit time of the water and on contact time with the warm environment.

(3) Drinking Water Temperature and Different Pavement Types As shown in Figure 1.4, the registered temperature of the soil under the grass and park was on average 1-2.8°C cooler than under the tiles. During the warmer days that difference reached a maximum of 3.5°C.

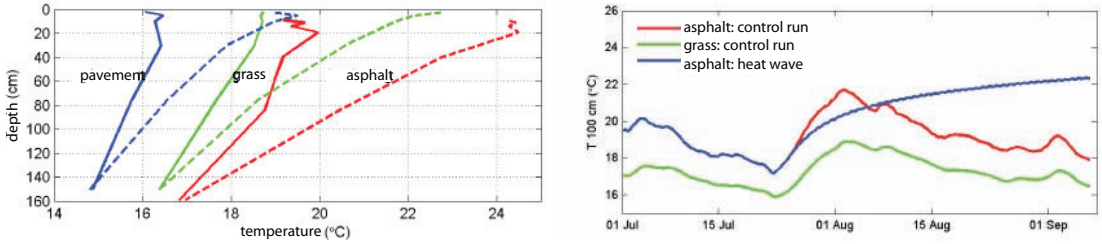

Figure 1.4: Simulation of the heat wave (left graph: 26th June-29th September 2008: continuous line; 23rd July-3rd August 2008: dashed line). The same run showing the possible difference in the temperature distribution under the 3 different pavement types at the control and heat wave runs. Source: (Van Der Molen et al., 2008).

(4) Heat Wave Conditions A simulation of the heat wave (repeated application of a temperature above 23°C) applied to the soil covered with different materials proved that it takes more than a week for the temperature of the soil to reach the air temperature at the heat wave conditions (see Figure 1.4 and 1.5). Thus, the chances that the drinking water temperature exceeds 25°C during the hot wave days are large.

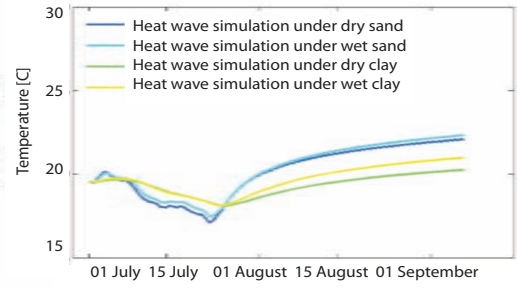

Figure 1.5: Heat Wave simulation applied to different soil types. - Simulation under the different soil types. From the figure it can be seen that the sand soil is more sensitive to the heat intrusion during the heat-wave conditions than clay. The degree of saturation is not as significant in case of sand as in case of clay soils. The heat have was simulated in starting from 1st of August. Source: (Van Der Molen et al., 2008).

(5) The Layer with the Largest Thermal Resistance Blokker and Pieterse-Quirijns (2009) report, that the 1m layer of soil constitutes the largest thermal resistance element in the vertical heat flux from the atmosphere to the drinking water. It means that the heat capacity of water in a network is much bigger than the soil. Thereby, the soil temperature will ultimately determine the drinking water temperature.

(6) Dependency of Pipe Heating Time on Water Flow According to Blokker and Pieterse-Quirijns (2009), in highly conductive pipes, the flow rate determines the pipe heating time. The lower the flow rate, the lower the convective heat transfer and the longer it takes for the water to heat up. However, the lower the flow rate, the longer the residence time and the longer the water is subjected to the conduction from the pipe walls. The resulting heat transfer is determined by the Nusselt number, which combines the impact of the two conduction and convection heat transfer modes.

(7) Relation Between Drinking Water Temperature and the Outside Temperature There is a strong relation between the average outside temperature and the temperature of the sampled water in taps. This is especially true when outside temperatures is above 5°C. Blokker and Pieterse-Quirijns (2009), indicate that the tap water in the Netherlands exceeds the standard level of 25°C in 0.001% of the total sampled water at the customers' taps per year. The biggest exceedance was observed in a relatively warm year of 2006.

Consequently, on the authority of the cited references (especially (4), (6) and (7)), it is likely that more Dutch drinking water supply companies find themselves in a situation of drinking water temperature approaching legally imposed standards and water quality problems such as the microorganisms regrowth in a supply network will become more apparent. The issue that applies particularly but not solely [1] to those water supply companies who have chosen a disinfection method alternative to chlorination (ozonation or UV disinfection).

Nevertheless, temperature elevation problem is not taken as necessarily endorsing a future threat to drinking water as there is little evidence of the linkages between the climate conditions and the drinking water temperature, and it is difficult to asses how the drinking water companies could address the problem. Measurements, if any available, could verify the possible linkages if they show that the drinking water temperatures can be influenced by the climate changes or Urban Heat Island Effect.

1.2 Heat and Cold Extraction: a Solution?

One interesting alternative to deal with the temperature problem in a distribution network is extracting excessive heat from the drinking water for sustainable energy production.

The idea is rather simplistic: during summer days, some parts of a drinking water supply network serve already as heat collectors. This heat, instead of deteriorating the water quality, could be extracted, and stored or diverted to a heat exchanger[2], by means of which the drinking water temperature would be regenerated and its temperature would decrease. However, it is questionable if such heat extraction at one point could retain the sought lower water temperature at the remaining parts of a supply network.

Waternet is currently researching on a best counter measure to prevent drinking water overheating. Heat extraction is one of the idea considered[3]. The concept is a thought provoking one, given the assumptions made (extraction will positively influence the temperature distribution in a network) and gaps in information provided (lack of factual information on temperature gradients in a network).

Before thermal efficiency of drinking water in a network to provide heat could be analysed, it is necessary to get more insight into temperature distribution in a network to specify at which points in the distribution grid distinctly high temperature changes could occur. Having identified the hot and cold

[1] In chlorinated water temperature affects chlorine decay, disinfection efficiency and formation of disinfection by-products, which are potentially harmful for humans Blokker and Pieterse-Quirijns (2009). The chlorine decay coefficient in bulk water increases more than threefold, when temperature increases from 10 to 20°C.

[2] There are several ways of cooling water, the highest efficiency would be probably achieved in water-water heat exchangers, in which tubes containing the hot water are cooled by an external flow of cold water, the temperature of which is raised (Slesser, 1982).

[3] This thesis is a part of a project, initiated at Waternet entitled 'Use Of Heat And Cold From A Drinking Water Network', which is a feasibility study on extracting heat from the drinking water during hot summer months when the temperature is most extreme.

spots, we can estimate the amount of heat available for the extraction and define a feasibility of the heat extraction concept.

1.3 Research Scope

The objective of the thesis is therefore to analyse and measure the temperature distribution in a drinking water supply network, especially at locations where climate alternations can be observed, in order to investigate what are the possibilities to cool down drinking water in summer, with a special attention given to the heat extraction method.

The two central research questions investigated in this thesis are: (i) which parameters most strongly determine the heat exchange between a pipe and the atmosphere, (ii) how may cooling or heating of drinking water at one location influence the temperatures in the other parts of the drinking water supply network.

In this thesis, the drinking water temperature alternations in a distribution system are estimated by models representing the heat fluxes between atmosphere, soil, a pipe and drinking water. Through a literature study two research projects were found that deal with heat-transfer pertinent to drinking water networks, namely a numerical model of heat diffusion in the soil developed by Van Der Molen et al. (2008) and an analytical model calculating the time of drinking water overheating, developed by Blokker and Pieterse-Quirijns (2009). The two models are applied in Epanet 2 a water distribution simulation software distributed by the United States Environmental Protection Agency (Rossman, 2000).

The interpretation of the modelling results require a validation. The experimental validation of the two selected models was based on the temperature data set obtained during a measuring campaign in a selected section of Waternet drinking water supply network. While we sought for a general applicability of the models and theories investigated in this thesis, it was only practical to focus our attention on a smaller, representative area of Waternet supply grid. We have chosen west part of Diemen Noord section as our focus.

The model simulations were also calibrated based on measured temperatures collected during the experimental session. We have analysed each model separately to define which one produces the biggest error and used this information to test different scenarios in the network. The scenarios tests allowed to define the time and pipe length needed to adjust to the soil temperature during the heat wave conditions and the time needed to cool down substantial parts of the network due to one-point heat extraction. The tests at the specific situation in west part of Diemen Noord, could help to select timely measures

preventing temperature elevations in Waternet network. This information could be extrapolated to the rest of Waternet supply network with a limited credibility.

1.4 Document Outline

This document is organized in 7 chapters. The content and the purpose of each chapter is listed below.

Chapter 1, 'Introduction', covers aspects and the background information on water temperature problems, specifically its impact on the water quality and the maintenance of a supply network. A number of relevant recent publications are summarised. Finally, the details on the scope and goals of the research are presented.

Chapter 2, 'Theoretical Framework', locates the issue of temperature modelling and heat and mass transfer within a broader approach of conservation laws and physical principles anticipated in the system. It includes the relevant findings obtained via literature research and basic modelling formulations.

Chapter 3, 'Materials and Methods', includes a description of an experiment at west part of Diemen Noord, the Netherlands, describes the particularities of the monitoring site, its characteristics and role in the Waternet supply network. It also includes the arguments on the choice of sampling locations and outlines the observational methodology. More specifically, issues such as the instrumentation, monitoring period, measurements frequency and accuracy are being discussed in this chapter.

Chapter 4, 'Measurements Analysis', is an analysis of the measurements obtained from the experiment. The major factors, that influence the heat fluxes and water temperature variations, are depicted by means of time series, signal spectrum analysis and correlation plots.

Chapter 5, 'Model Validation', is an analysis of the heat-flux models described in chapter 3. The major factors, that influence the heat fluxes and water temperature variations, are depicted by means of model validation and error propagation.

Chapter 6, 'Discussion', briefly discusses the result analysis in a background of the previous studies made in the same region.

Chapter 7, 'Conclusions and Recommendation', summarises the result analysis and concludes to the research findings with analysis of different potentialities and scenarios.

2

Theoretical Framework

2.1 Introduction

A purpose of this thesis is to understand, model and measure the heat transfer processes entailing drinking water temperature in a network. This theoretical framework therefore begins with a discussion on relevant empirical formulations, materials and methods to quantify the vertical energy transit through the air layer, soil and a pipe. Along with the description of the methods, the parameters of main importance to the heat transfer modelling are being revealed.

Next, a description of the physical processes associated with internal flow and physical parameters that are significant to concurrent mass and heat transfer in the pipes, will be given. This should give us an impression of how the local heat convection coefficient can be obtained and how the heat can be generated in the fluid conveyed in a pipe and what processes determine the change in temperature of drinking water. We go into some of the issues concerning the process of forced convection and hydraulics. But because of its complexity of relations and derivations, the governing formulations for continuity and momentum pertaining to the forced convection are left to the literature (Incropera and De Wit, 2002).

2.2 Energy Budget

Sources of thermal energy influencing the drinking water temperature include: climatic conditions, surface conditions, soil characteristics and drinking water discharges. Drinking water does not directly come in contact with the atmosphere or the soil enclosure but the heat fluxes resulting from the both layers constitute a major heat source at the drinking water pipe wall. The energy budget can be therefore illustrated as in Figure 2.1.

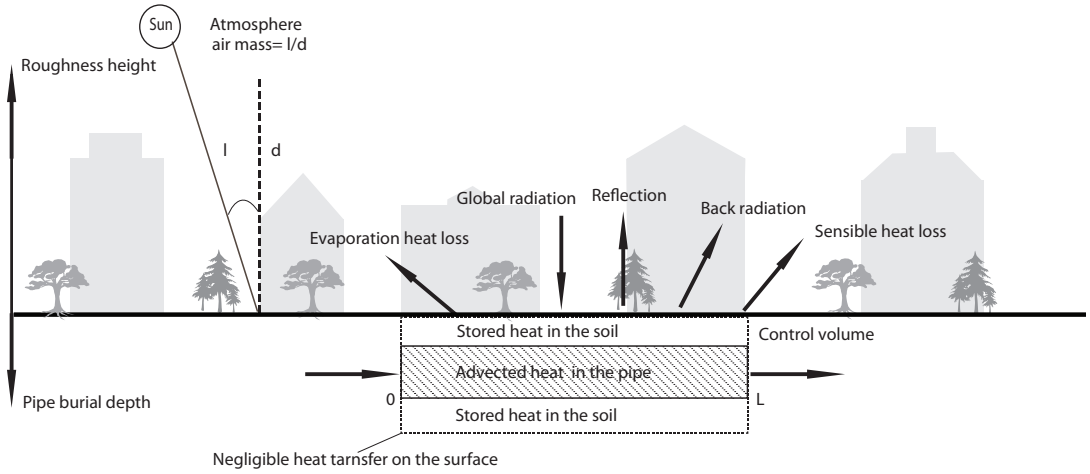

Figure 2.1: Overview of the thermal processes encountered at the surface of a pipe control volume. - The scheme depicting a principal partitioning of the incoming solar radiation into fluxes.

The total energy budget of a pipe , as depicted in Figure 2.1, during passage of water can be obtained from the following components:

$$\dot{E}_g + \dot{E}_{in} - \dot{E}_{out} = \dot{E}_{st} \tag{2.1}$$

where $\dot{E}_{st}$ is thermal energy generation, $\dot{E}_g$ is thermal and mechanical energy transport across the pipe volume. All terms are measured in joules. A dot indicates a rate.[1]. All the energy terms can be reported over interval of time and in one dimension. Energy generation, E_{st}, [W] is associated with the heat capacity of the pipe $\rho c_p \frac{\Delta T}{\Delta t}$. The energy budget $E_{in} - E_{out}$, [W], can be elaborated from Fourier's law of cooling. This energy term is related to a vertical heat flux at the pipe wall interface. E_g, [W], is a horizontal heat flux that represents heat and mass transport due to bulk motion of the drinking water.

Almost all energy available to the city surface and atmosphere is emitted by the sun in the form of solar radiation.[2]. However, due to the complexity of an urban situation[3], more energy is stored in the

[1]Details on the energy generation are given in Appendix A.3

[2]The intensity of this energy depends on the emissive power and spectrum. The solar radiation is strongest at short wavelengths, 0.4-0.6 [μm], and is therefore often referred to as short-wave radiation. The earth also emits heat. The terrestrial radiation is strongest at the longer wavelengths , 6-10 [μm], and is therefore often referred to as long wave radiation.

[3]Essentially, there is a number of parameters influencing the energy partition. Firstly, the solar inclination greatly influences the density of a maximum solar power; the smaller the inclination, the further the sun is from the normal and the grater the thickness of atmosphere which must be traversed and the more photons are scattered and absorbed (Neville, 1995). Secondly, the urban architecture affects the total energy balance and partitioning of the fluxes of energy, moisture and momentum. Thirdly, the energy balance of an urban air volume includes the heat source from solar radiation and the anthropogenic emissions, such as combustion or heating from buildings.

city and less is released to the atmosphere[1]. Normally, the city's energy budget within such layer, as depicted in Figure 2.1, is divided into heat fluxes (see equation 2.2, (Oke, 1982)):

$$Q^* + Q_f = Q_e + Q_h + \Delta Q_s + \Delta Q_a \tag{2.2}$$

where Q*, $[\mathrm{W/m^2}]$, Q_f[2] is the anthropogenic emission heat emission, $[\mathrm{W/m^2}]$, Q_e is the latent heat flux, $[\mathrm{W/m^2}]$, Q_h is the sensible heat flux, $[\mathrm{W/m^2}]$, ΔQ_s is the net city's storage, $[\mathrm{W/m^2}]$ and ΔQ_a is the net advection in and out of the city, $[\mathrm{W/m^2}]$.

The net all-wave radiation is a sum of the net solar radiation, K*, $[\mathrm{W/m^2}]$ and net atmospheric radiation L*, $[\mathrm{W/m^2}]$. The net all-wave radiation is a difference between the thermal energy that is released due to emission and the energy absorbed from all incident radiation. Net solar radiation, K* is a difference between $K\downarrow$ and $K\uparrow$. The net atmospheric radiation, L* is a difference between $L\downarrow$ and $L\uparrow$.

The time-scale of the urban surface energy fluxes is normally less than a day. There is a shift in the strength of the long and short wave radiative exchanges during a daytime and night. During night long wave radiation prevails and the surface is cooling. During daytime the surface is heating, see Figure 2.2. Cooling in cities is impaired as warmer surfaces promote greater thermal emission of energy vertically upward from the city, particularly at night (in Figure 2.2: flux 5).

Essentially, the energy heat transfer from the air to the drinking water is modelled through the following processes : (i) radiation from the sun to the earth's surface, (ii) sensible heat from the roughness layer to the atmosphere, (iii) sensible heat from the soil surface to the roughness layer, (iv) conduction from the surface to the deeper soil layers, (v) convection, in case of wind, from the air to the soil surface.

The soil surface temperature is normally estimated from the energy balance at the roughness layer and the energy balance at the soil surface. The surface heat balance of the solar radiation determines a density of ground heat flux, which constitutes the heat transfer rate at the pipe wall –soil interface. The amount of heat that penetrates into the soil at specified distance depends on the soil diffusivity and initial soil temperature. In the following sections of this chapter we will describe how those fluxes can be modelled[3].

[1] Buildings, trees, unnatural surface cover, waste heat and water vapour from human activities in a city affect the natural air-flow and radiation exchange between the atmosphere and the Earth surface. Additionally, in cities a vertical exchange of momentum, heat and moisture do not occur at a plane surface, but in a layer of a significant thickness, called the urban canopy layer, (WMO, 2008).

[2] Q_f is highly city-dependent and seasonally variable, It ranges from 0 to 300% of Q*, and depends on the degree of industrialization (Q_f is high in more industrialized cities), latitude (Q_f is high in higher-latitude cities), and season (Qf is higher in winter). More details can be found in (Oke, 1997)

[3] Components of the surface energy balance are reported in units of $[\mathrm{W/m^2}]$.

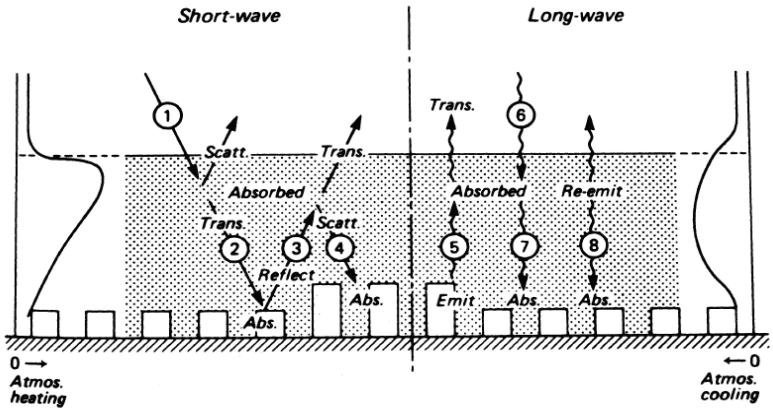

Figure 2.2: Radiative exchanges in a polluted urban boundary layer. - The scheme includes generalized profiles of short-wave radiative heating (left) and long wave cooling (right) due to the existence of an urban aerosol layer (shaded). Numbered fluxes are referred to in the text. Source: (Oke, 1981)

2.3 Heat Exchange in the Atmosphere

The drive for the energy flow between the roughness layer and the atmosphere and between the soil surface and the roughness layer is a sensible flux. The total heat flux is calculated as a sum of the sensible fluxes within the two layers. To model this flux parameters that represent the atmospheric stability such as drag coefficient, Richardson's bulk number, friction temperature and velocity, are used.

The gradient that drives the sensible flux is the ratio of the potential temperature T_p to the air temperature T_a. In many practical near-surface applications T_p is replaced by T_a because the difference in pressure between near-surface and the reference measurement levels is negligible.

2.3.1 Sensible Heat Flux

Under neutral conditions the turbulence is almost only caused by the wind shear. The sensible heat flux equation then yields

$$Q_h = \kappa \cdot u_* z \rho_a c_p \frac{\partial T_a}{\partial z} \tag{2.3}$$

where u_* is a friction velocity, [m s], κ is the Von Karman[1] constant [-], z is the wind measurement

[1]The Von Karman constant (or Karman constant) is a dimensionless constant describing the logarithmic velocity profile of a turbulent fluid flow near a boundary with a no-slip condition. The equation for such boundary layer flow profiles is: $U = u_* \kappa ln \frac{z}{z_0}$ where U is the mean flow velocity at height z above the boundary. The roughness height z_0 is where u appears to go to zero. Further κ is the Von Karman constant (typically equals the value of 0.41), and u_* is the friction velocity which depends on the shear stress τ at the boundary of the flow:$u_* = \sqrt{\frac{\tau_w}{\rho}}$ with ρ the fluid density. Source: Wikipedia, the free encyclopaedia. Retrieved on 20.06.2009, from http://en.wikipedia.org/wiki/Theodore von Karman.

level above surface [m], ρ_a is the density of air [$\mathrm{kg/m^3}$], c_p is the specific heat of air [$\mathrm{J/kg\ K}$].

Profile of Wind Velocity

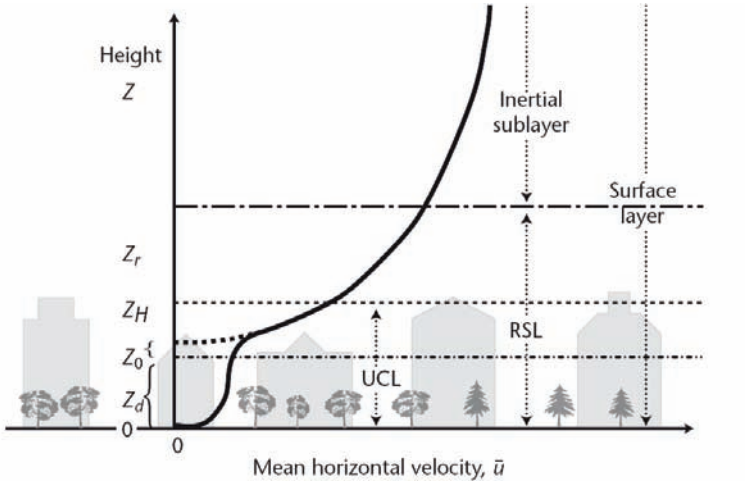

Figure 2.3: A wind velocity (u) profile in a densely developed urban area - A scheme represents a general wind mean including the location of sub layers of the surface layer. The measures on the height scale are the mean height of the roughness elements (z_H) the roughness sub layer (z_r, or the blending height), the roughness length (z_0) and zero plane displacement length (z_d). The dashed line represents the profile extrapolated from the inertial sub layer, the solid line represents the actual profile. Source: (WMO, 2008)

The value of u_* is related to the wind shear and can be used as a scale for how wind evolves in the verticals (see Figure 2.3). The value of a wind shear can be obtained from a comparison of two wind measurements in the vertical according to :

$$u_* = \frac{\kappa(u(z1) - u(z2))}{ln\left[\frac{z_1}{z_2}\right]} \tag{2.4}$$

or, assuming that there is one point in the vertical, where u becomes zero (so $z_2 = 0$ and $z_2 = z_{om}$ or $z_2 = z_H$) the friction velocity can be calculated from:

$$u_* = \frac{\kappa u(z)}{ln\left[\frac{z}{z_H}\right]} \tag{2.5}$$

Aerodynamic Resistance

Parameters that represent the thermal resistance can be lumped into one coefficient termed the aerodynamic resistance, r_{ah}. The aerodynamic resistance coefficient represent the effect of turbulence on the

heat fluxes. Its value between two arbitrary levels in the vertical (e.g. the surface roughness height z_H and any upper level, z) and in case of the stable atmospheric conditions, can be obtained from:

$$r_{ah} = \frac{1}{k \cdot u_*} ln \left[\frac{z}{z_H} \right] \tag{2.6}$$

Stability of Atmosphere

Neutral conditions occur when the atmosphere is stable. A stable state occurs when there is a downward movement of eddies (at a cold cloudless night) and unstable when eddies move up from the surface (at a warm cloudless day, when the air close to the surface warms up very easily) (Savenije, 2007)[1]. Stable conditions do not occur very often (Savenije, 2007).

Richardson's Bulk Number

The Richardson's bulk number R_{i_b} is related to the stability of the atmosphere and defines whether air convection is free or forced. If R_{i_b} is bigger than zero then the air temperature increases with height and the atmosphere is stable otherwise unstable conditions prevail. The Richardson's bulk number can be obtained from the following equation (Blokker and Pieterse-Quirijns, 2009):

$$R_{i_b} = \frac{g \cdot z}{1/2 \left(T_a(z) + T_a(z_H) \right)} \frac{\left(T_a(z) - T_a(z_H) \right)}{u^2} \tag{2.7}$$

where g is the gravitational constant, $T_a(z)$ is the atmospheric temperature and $T_a(z_H$ is the roughness layer temperature (see Figure 2.3).

2.3.2 Stable Atmospheric Conditions

If we substitute the wind shear value into equation 2.6 then the sensible heat during the stable atmospheric conditions can be expressed as:

$$Q_h = \rho_a c_p \left(\frac{T_a(z) - T_a(z_H)}{r_{ah}} \right) \tag{2.8}$$

$T_p(z_H)$ is the temperature at a level called roughness height z_H, which is a certain displacement level at which the heat exchange with the surface may be neglected[2]. Because at the roughness height

[1] There is a constant exchange of the fluxes between the roughness boundary layer and the land surface (Savenije, 2007). Due to heating up the surface by the sun and buoyancy the boundary roughness layer grows in the morning and shrinks in the evening. Turbulent flux exchanges into atmosphere are typically driven by wind shear, buoyancy and a temperature gradient. This turbulence causes the vertical movement of air parcels that cater for heat fluxes.

[2] According to Blokker and Pieterse-Quirijns (2009) the roughness height oscillates between $0\ 001\mathrm{m}$ for the land cover typical at the sea and $10\mathrm{m}$ for the densely built city district.

there is no heat exchange, the temperature at this height may be approximated as equal to the surface temperature value.

2.3.3 Unstable Atmospheric Conditions

Van Der Molen et al. (2008) proposes to calculate the sensible heat flux as a sum of the sensible heat exchange between the atmosphere and the roughness layer and the sensible heat between the soil surface and the roughness layer as follows:

$$Q_h = \rho_a c_p \left(\frac{T_a(z) - T_a(z_H)}{r_{ah}} \right) + \rho_a c_p C_D \left(T_a(z_2) - T_a(z_H) \right) \psi_h \tag{2.9}$$

where $T_p(z)$ is the temperature of the atmosphere, $T_p(z_H)$ is the temperature at the roughness layer and $T_p(z_2)$ is the temperature at the surface. Thereby, Blokker and Pieterse-Quirijns (2009) distinguishes a drag coefficient; a separate parameter which is strongly associated with the aerodynamic resistance coefficient.

$$C_D = \left(\frac{\kappa}{ln\left(z/z_H\right)} \right)^2 \tag{2.10}$$

2.3.4 Atmospheric Stability Coefficients

The values of the aerodynamic resistance and wind shear are corrected according to the state of the atmosphere by correction functions for the heat and momentum, ψ_m and ψ_h, respectively. These functions depend on the dimensionless factor $\frac{z}{L}$ where L is the MoninObukhov length [1] and z is the reference height, where the measurements are taken. The value of the functions depend on the empirical formulations. The commonly used is the one proposed by Brutsaert (1982):

$$u_* = \frac{\kappa u(z)}{ln\left[\frac{z}{z_H}\right] - \psi_m(\frac{z}{L}) + \psi_m(\frac{z_H}{L})} \tag{2.11}$$

$$r_{ah} = \frac{1}{k \cdot u_*} \left[ln\left(\frac{z}{z_H}\right) - \psi_h(\frac{z_1}{L}) + \psi_h(\frac{z_2}{L}) \right] \tag{2.12}$$

where according to (Blokker and Pieterse-Quirijns, 2009) ψ_m for stable conditions equals:

[1] A length where the :$L = -\frac{u_*^3 \bar{\theta}_v}{kg(\overline{w'\theta'_v)_s}}$; where $\bar{\theta}_v = T_a(z_1) - T_a(z_2)$ which is the mean virtual potential temperature, $(\overline{w'\theta'_v})_s$ is the surface virtual potential temperature flux. When L is negative with a small magnitude, $\frac{z}{L}$ is negative with a large magnitude. Such values of $\frac{z}{L}$ correspond to large instability due to buoyancy. Positive values of $\frac{z}{L}$ correspond to stable stratification. Source: Wikipedia, the free encyclopaedia. Retrieved on 25.06.2009, from en.wikipedia.org/wiki/Monin Obukhov Length

$$\psi_m = \frac{1}{1 + 10R_{i_b}/\sqrt{1 + 5R_{i_b}}} \tag{2.13}$$

for unstable:

$$\psi_m = 1 - \frac{10R_{i_b}}{1 + 75C_D\sqrt{z/z_H}\sqrt{|R_{i_b}|}} \tag{2.14}$$

Similarly, the momentum function, for stable conditions, can be calculated from:

$$\psi_h = \frac{1}{1 + 15R_{i_b}\sqrt{1 + 5R_{i_b}}} \tag{2.15}$$

for unstable conditions:

$$\psi_h = 1 - \frac{15R_{i_b}}{1 + 75C_D\sqrt{z/z_H}\sqrt{|R_{i_b}|}} \tag{2.16}$$

2.3.5 General Formulation for Sensible Heat Flux

The sensible heat flux equation, according to (Blokker and Pieterse-Quirijns, 2009) yields

$$Q_h = \rho_a c_p \left(\frac{T(z) - T(z_H)}{r_{ah}}\right) + \rho_a c_p C_D \left(T(z_2) - T(z_H)\right)\psi_h \tag{2.17}$$

2.4 Heat Exchange at the Soil-Air Interface

Using the sensible heat flux obtained from the calculations at the roughness layer and the measurements of the global solar radiation, the ΔQ_s ground heat flux is calculated from a balance of the following components:

$$\Delta Q_s = K^* + L^* - Q_h \tag{2.18}$$

where $K^* = K\downarrow - K\uparrow$where $K\downarrow$ is measured by the nearest synoptic station and $K\uparrow = K\downarrow \alpha_g$, while $L\downarrow = \epsilon_a\sigma(T_a)^4$. α_g and ϵ_a are taken either from the literature or measurements.

A positive value of the net short (K^*) and long wave (L^*) indicate that energy is being transferred from the air to the surface, a negative value indicates the opposite [1]. More detailed study of relevant

[1] According to Arnfeld and Grimmond (1997), the bigger thermal inertia, a property related to the thermal conductivity and volumetric heat capacity of the receiving material, the more energy from the global radiation is channelled to the soil storage. Thermal inertia is a parameter which is often used to determine temperature variations that propagate with depth to a soil or to estimate the prevalent dynamic effects in a model. Thermal inertia is measured in $\mathrm{J/m^2\ K\ s}$ yields:

$$I = \sqrt{\kappa \cdot C} \tag{2.19}$$

fluxes is important in predictions of a heat transfer to the pipe.

Global Radiation

The global radiation $K\downarrow$ represents a mix of scattered and diffused fluxes (S and D, respectively) (see Appendix A.2). The $K\downarrow$ is measured and can be obtained from measurements made by a standard synoptic station (WMO, 2008).

Oke (1982) estimates that depletion of global (short wave) radiation in cities is less than 10%, whereas Medrano (2008) posited that in the urban context the direct solar radiation can be attenuated by 70% when the solar elevation angle is lower than the building's shaddow angle.

Reflected Solar Radiation

Density of the reflected solar radiation $K\uparrow$ depends on albedo. Albedo relates to the rate at which the irradiation is absorbed, α ($1 \geq \alpha \geq 0$). When absorptivity is smaller than 1 the surface is opaque and the portions of irradiation are reflected. At the semitransparent surfaces the portions of irradiation can be transmitted to the deeper layers. The variation of albedo within the city depends on the percentage of vegetative cover, the variation in building material and composition of roof material as well as land-use characteristics, the albedo of a surrounding terrain and the season (Oke, 1982).

Greater absorption of solar radiation, during daytime, is due to darker surface materials and due to effects of trapping of short wave radiation by the vertical walls and the urban canyon-like morphology.

The regional albedo for the Netherlands amounts to 0.1, according to Van Mazijk (2004). Remaining albedo values for particular surfaces are given in standards and books, such as (Incropera and De Wit, 2002).

Atmospheric Emissivity

The downward long wave radiation $L\downarrow$ depends on the temperature of the atmosphere. Since the temperature varies according to the condition in the sky, presence of clouds (see Appendix A.2) the temperature is often corrected by emissivity factor which differs from one covering to another. Generally, it depends on the surface emissive power, which is always close to unity, can be described as:

$$E = \epsilon\sigma T_s^4 \tag{2.20}$$

The downward long wave radiation $L\downarrow$ can be then calculated as follows:

where k is the thermal conductivity, and C is volumetric heat capacity. The temperature of a material with high thermal inertia changes significantly during a day, while the temperature of a material with low thermal inertia does not change as drastically.

$$L \downarrow = \epsilon_a \sigma (T_a)^4 \tag{2.21}$$

where ϵ's value has been empirically defined by Brutsaert (1982) and is directly proportional to the e_o, vapour pressure hPa and inversely to the air temperature [K], as follows:

$$\epsilon_a = 1.24 \left(\frac{e_o}{T_a} \right)^{\frac{1}{7}} \tag{2.22}$$

Atmospheric Back Radiation

Long-wave back radiation $L \uparrow$ is bigger in cities than in rural areas due to city's pollution and warmer surfaces. This is especially discernible during night, at the clear and calm sky (Oke, 1981). At this time the rate of surface cooling is driven by net long wave radiation loss. The magnitude of this loss is proportional to its exposure to the sky, which is measured by the sky view factor. Warmer surfaces promote greater thermal emission of energy vertically upward from the city surface compared to rural areas (flux 5 in Figure 2.2). Some long wave radiation is re-radiated by urban aerosols back to the surface and also from the warmer urban air layer(in Figure 2.2: fluxes 7 and 8). The estimation of upward long wave radiation was calculated in (Rutten, 2006) as

$$L \uparrow = L \downarrow \cdot \alpha \tag{2.23}$$

where Rutten (2006) reports $\alpha_a = 0.16$.

Surface Evaporation Heat Loss

If any water, bare soil or vegetation is present at the surface, the heat is also lost from the surface by the latent heat flux. Latent heat flux Q_e is a generic therm for evaporation and condensation depending on the wind speed, climate and relative humidity. In the urban canyons due to the waterproofing of the pavements (see Figure 2.4) latent heat flux is negligible. Therefore, the latent heat flux is not included in the urban energy balances. As a result of negligible latent heat flux, more Q_h and ΔQ_s is promoted (Offerle et al., 2003) and (Arnfeld and Grimmond, 1997).

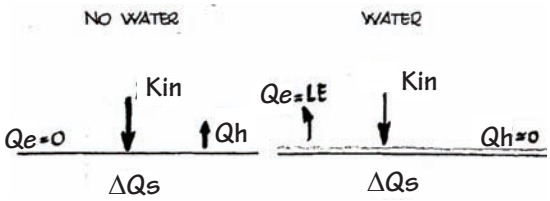

Figure 2.4: The energy balance at the dry urban canyon. - The latent heat flux of vaporization occurs only in the presence of water or vegetation.

2.5 Heat Exchange in the Soil Layer

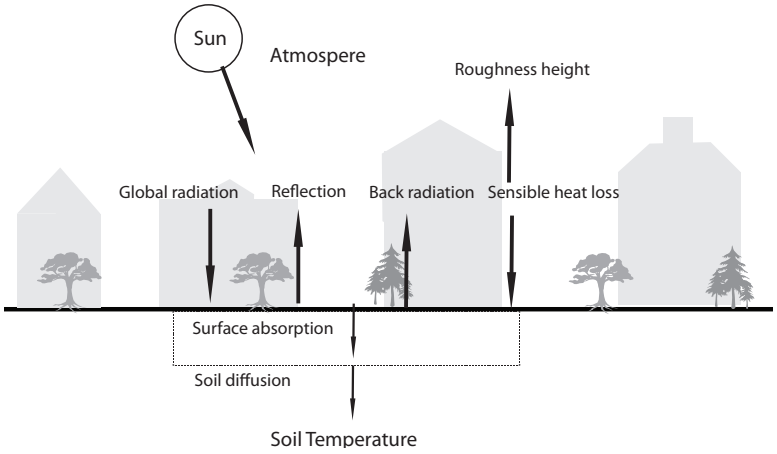

Figure 2.5: The scheme based on the soil temperature model developed by Van Der Molen et al. (2008). - The calculated vertical heat-flux in the soil is based on the soil diffusivity which has been calibrated from the experimental values.

The temperature available at the pipe burial depth can be quantified from the ground heat flux. The heat transfer from the surface to the deeper soil layers can be calculated from diffusion equation, which is based on the Fick's equation[1]:

$$\Delta Q_s = \frac{k}{\rho \cdot C_p} \cdot \left(\frac{\delta^2 T_{SS}}{\delta z^2} \right) = D \left(\frac{\delta^2 T_{SS}}{\delta z^2} \right) \tag{2.25}$$

where D is the soil diffusivity, k is the soil conductivity and $\rho \cdot C_p$ is the soil capacity.

[1] Fick (1855) has shown the importance of the gradients and resistance in his research on diffusion.

$$F = D \cdot \frac{\nabla S}{r} \tag{2.24}$$

where f is some flux through medium over some distance, D is the diffusion constant (depends on the medium), gradient S is the driving gradient of some state and r is an effective resistance, depend on for example on the distance in the potential field.

The rate of this transmission depends on the mass and molecular arrangement of a receiving solid, the soil volumetric water content, volume fraction of air[1] and heat capacity of the soil. Soil's heat capacity and conductivity determine how much energy will be lost due to the diffusive transport via the soil layer (see a scheme of this process in Figure 2.5).

Abu-Hamdeh (2003) substantiated a functional dependency of the thermal diffusion coefficient value of the sandy and clay soils on the water content is important in determining a diffusivity coefficient. In the Figure 2.6 it can be seen that sandy soils exhibit sharp jumps in the diffusivity value as the water content increase whereas clay soils' diffusivity changes are more stable.

The differences in the a functional dependency of sandy and clay soils diffusivity on water content, are due to the character of water transport process in the sand and clay. During rainfall events, while the soil becomes wetter, a film at the soil particles increases conductivity between solid parts of the sand. This causes a sharp increase in thermal conductivity and thus diffusivity (Steele-Dunne et al., 2010).

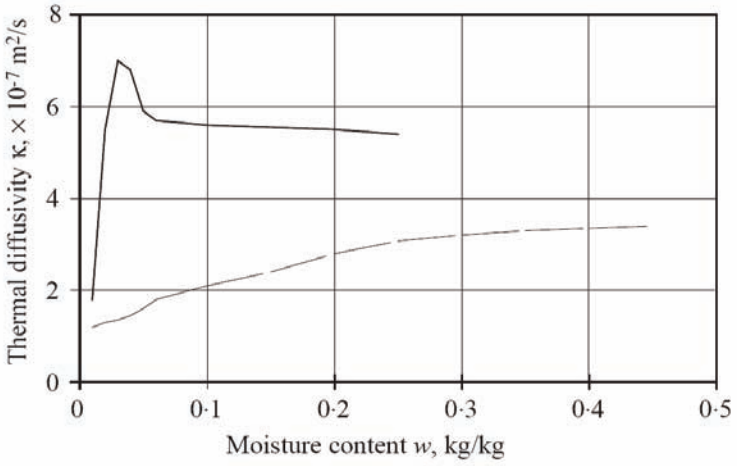

Figure 2.6: Thermal diffusivity as a function of a soil moisture content. - Dotted line is a diffusivity of clay and solid line represents sandy soils. Source:(Abu-Hamdeh, 2003)

2.5.1 Soil Thermal Conductivity

Soil thermal conductivity increases proportionally to the level of saturation but it depends also on lattice mineral composition (particularly quartz content[2], porosity, dry density and temperature. Peters-Lidard

[1] Air is a poor thermal conductor $(0, 026\mathrm{W/m/K})$ and reduces the effectiveness of the solid and liquid phases to conduct heat. While the solid phase has the highest conductivity it is the variability of soil moisture that largely determines thermal conductivity (Korevaar et al., 1983).

[2] Transport of thermal energy in solids is due to two effects: the migration of free electrons and lattice vibrational waves. These effects are additive, such that thermal conductivity k is the sum of the electronic component k_e and the lattice component k_l, such as $k = k_e + k_l$. The regularity of the lattice arrangement has an important effect on k_l. The well ordered (crystalline) materials like quartz, have a higher thermal conductivity than amorphous materials like glass.

(1998) suggest calculation of the thermal conductivity of a soil, as a function of its saturation, porosity, quartz content, dry density and phase of water (frozen or unfrozen). By the Jahansen75 method, thermal conductivity k as a combination of the dry k_{dry} and saturated k_{sat} thermal conductivities, weightier by a normalized thermal conductivity (K_e, known as a Kersten number) can be calculated. More details can be found in (Peters-Lidard, 1998) (see MATLAB code in Appendix A.12).

2.5.2 Soil Thermal Capacity

A product of soil's density and specific heat ρc_p, $[\mathrm{J/m^3\ K}]$ commonly termed the volumetric heat capacity, measures its ability to store thermal energy. Substances of large density are typically characterized by small specific heats, many solids and liquids, which are very good energy storage media, have comparable heat capacities $\rho c_p > 1$ $[\mathrm{MJ/m^2\ K}]$. The soil thermal capacity may be written (Steele-Dunne et al., 2010)as

$$C = \rho_m c_m = \frac{V_a}{V_t}\rho_a c_a + \frac{V_w}{V_t}\rho_w c_w + \frac{V_s}{V_t}\rho_s c_s \tag{2.26}$$

where: C is the heat capacity of soil, equal to the product of the soil density, ρ_s and the mass specific heat of the soil, c; subscripts m, a, t, w, and s represent the bulk soil, air, total, water and soil solids. V and ρ are the volume fractions and density of volume components (e.g, water, solid, gas phase). Gas volume fraction is negligible.

2.5.3 Principles of Soil Temperature Modelling

The solve the soil diffusion equation a numerical or analytical model can be used. The analytical model assumes how the temperature changes with depth without having any temperature data available. The numerical model provides an accurate two-dimensional (time and space) distribution of soil temperature.

Analytical Model

The analytical model is based on the assumption that temperature at the surface of the soil is phased with the air temperature and oscillates depending on a season. At soil depths temperature variations are transferred lagged and reduced relative to the surface temperature. The amplitude of fluctuations within the soil decays exponentially with distance from the surface (Incropera and De Wit, 2002). Those temperature variations are short-lived diurnal (day-night) oscillations and annual (seasonal) cycles. Therefore, the analytical model, termed also the transient heat diffusion model, calculates the temperature changes

over time assuming a sinus temperature function (see equation 2.27). Korevaar et al. (1983) realizes the soil temperature at depth d has a constant average temperature as follows:

$$\frac{\delta T_{SS}}{\delta t} = T_{av} + A_o exp(\frac{-d}{\delta}) sin(\omega \cdot \frac{t-d}{\delta}) \tag{2.27}$$

where $\frac{\delta T_{SS}}{\delta t}$ is the soil temperature at depth d and time t, A_o is the amplitude of the sinusoidal temperature variation at the soil surface, ω is the angular frequency of the temperature variation (wave), t is time and δ is the damping depth.

The angular frequency of the temperature variation can be obtained from:

$$\omega = 2 \cdot \frac{\pi}{t_c} \tag{2.28}$$

where t_c is the time needed to complete one cycle of the wave. The amplitude of the heat wave decreases with soil depth with the ratio $\frac{-d}{\delta}$.

The damping depth, termed also the thermal penetration depth, depends on the thermal properties of soil, such as diffusivity and on the angular frequency of the temperature variation according to:

$$\delta = \sqrt{\frac{2 * D_h}{\omega}} \tag{2.29}$$

where δ is the damping depth [m], D_h is the diffusion coefficient and ω is the angular frequency of the temperature variation. Typically it is assumed the pipe burial depth is below the damping depth as formulated by 2.29.

Numerical Model

The numerical model can be based on a number of schemes. Most commonly a mid-point rule is used for soil temperature calculations. According to the mid-point rule the continuous models and equations can be represented by the following discrete counterparts. For every m (=1:M) between surface and soil at pipe depth and time t, the temperature will be:

$$T_{m,t+1} = D_{soil} \left((T_{m+1,t} - T_{m,t}) - (T_{m,t} - T_{m-1,t}) \right) \frac{\Delta t}{(\Delta z)^2} + T_{m,t} \tag{2.30}$$

where m = 1:M is calculated for time t before time t+1 is calculated. N.B. for numerical stability $(\delta t / \delta z^2) \leq \frac{1}{2}$ (Incropera and De Wit, 2002).

Principles of the model are shown in the figure 2.7. The initial values given at t_{n-1} and boundary values at z_{m+1} and z_{m+i} are necessary to start up the model. After the initialization, the model uses the

calculated values at t_n as a new input.

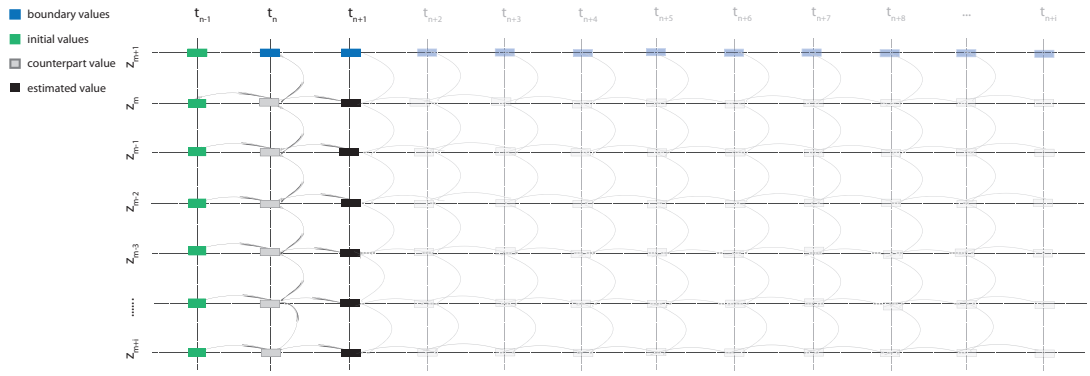

Figure 2.7: A numerical scheme to calculate a ground heat flux into a soil. - The calculation scheme is according to the mid-point rule.

The soil model of Van Der Molen et al. (2008) uses the mid–point scheme[1]. At the heart of the Van Der Molen et al. (2008) model is an extrapolation routine which calculates new input from the calculated values at every model time step. To start up model needs the state and boundary values, initial temperature values at the surface layer and in the different stratum of the soil are needed (see Figure 2.7).

The numerical diffusion model of Van Der Molen et al. (2008) calculates the propagation of the heat to the lower soil layers according to the imposed state variables such as soil heat capacity and conductivity.

The model is first order accurate and therefore needs a significant initiation time in order to reduce the impact of the imposed initial values on simulation results.

2.5.4 Heat Exchange at the Pipe-Soil Interface

The soil temperature is reduced at the pipe wall due to surface roughness effects. At the soil–pipe wall interface the gasps filled with air impair the heat transfer and temperature drop between materials may be appreciable. This effect attributed to thermal contact resistance is shown in Figure 2.8 and can be defined as:

[1] A numerical model representing the transfer of heat to the soil was developed on the basis of weather and soil measurements conducted during three months, from June till August 2008 in Brabant Water, a drinking water company in Breda, the Netherlands. The model simulates the heat flux as a function of weather, different surface and soil thermal conditions. The calibration of model parameters was done to obtain the best match with the measurements. The report summarized the findings appeared in H2O (H_2O 7/2009), a Dutch magazine for water management, in April 2009. The article written by Van der Molen et al. from the VU University Amsterdam (abbreviation here used: VUA) and the KWR, Dutch Watercycle Research Institute, concerned researching the temperature of the drinking water in the distribution network in Breda (Brabant Water), the Netherlands.

$$R_{t,c} = \frac{T_A - T_B}{q_x} \tag{2.31}$$

Contact spots are interspersed with gasps that are, in most instances filled with air. Heat transfer is therefore due to conduction across the actual contact area and to conduction and/or radiation across the gasps.

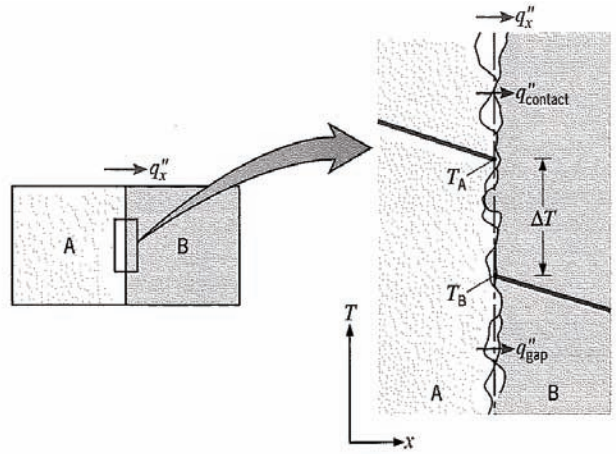

Figure 2.8: Schematic representation of a thermal resistance due to gasp at the interface of two different surfaces. - The thermal contact resistance is due principally to surface roughness effects. Source: (Incropera and De Wit, 2002)

2.6 Heat and Mass Transfer in a Pipe

This section in major parts is based on (Incropera and De Wit, 2002).

At inner pipe wall, the heat transfer has two modes: convection and conduction. The convection occurs between a surface and a moving fluid or gas when they are at different temperatures, whilst conduction exists in a stationary medium, like a pipe wall (Incropera and De Wit, 2002).

A convection heat transfer comprises of two mechanisms: random molecular motion (diffusion) and a bulk motion of the fluid (advection). In a pressurized pipes a bulk motion prevails and a collective movement of a large number of molecules contribute to a heat transfer.

The rate of conduction is determined by the conductivity of the pipe material ($k_{pipewall}$) and the thickness of the pipe wall ($D_{pipewall}$). The convective heat transfer coefficient (h) is a function of the flow rate, liquid properties, geometry of the pipe and its roughness, density, conduction coefficient and heat capacity which can be characterised by dimensionless numbers: Reynolds, Nusselt and Prandtl.

Heat Transfer Indices

Nusselt number is equal to the dimensionless temperature gradient at the surface and provides a measure of the convective heat transfer occurring at the surface. Nusselt number is a ratio of convection to pure conduction heat transfer mode. At the same time, Nuseelt number is a function of a distance, Reynolds number and Prandtl number. The high Nusselt number indicates good convection situation. The relevant equations, for the Nusselt number, will be reported in the proceeding sections.

Prandtl number is a ratio between kinematic viscosity and thermal diffusivity. The ratio indicates the efficiency of fluid to transport momentum to the efficiency to heat transfer. The higher the Prandtl number the more viscous is the fluid. More details on the specificity of this number are given in (Incropera and De Wit, 2002).

Reynolds number depends on the velocity. The Reynolds number can be calculated from $Re_D = \frac{\rho u_m D}{\mu}$[1] or at a given cross section A_c, from:

$$Re_D = \frac{4\dot{m}}{\pi \mu D} \tag{2.34}$$

The Thermal Entry Length

If fluid enters the tube at the uniform temperature T (r,0), that is less than surface temperature T_s the heat convection occurs and at the inner pipe wall a thermal boundary layer, δ_t begins to develop. Eventually, a thermal fully developed condition is reached (see Figure 2.9).

Reynolds and Prandtl numbers determine the length to fully developed conditions. When the laminar flow prevails ($Re_D \leq 2300$), the thermal entry length can be calculated from the following relation:

$$\left(\frac{x_{fd,t}}{D}\right)_{laminar} \cong 0.05 Re_D \cdot Pr \tag{2.35}$$

[1] It is assumed that in the radial direction the velocity profile inside a pipe has a parabolic shape. Thus, velocity is zero near the inner pipe wall therefore there is no advection of thermal energy through the surfaces in the radial direction. The only advection occurs in the axial direction, so along the pipe length. This advection originates from the vertical heat flux.

For the calculations the velocity profile in a pipe can be obtained from the total mass flowing integrated over the tube at any axial location x yields

$$u_m = \frac{2}{r_0^2} \int_0^{r_0} u(r,x) r dr \tag{2.32}$$

where:

$$\dot{m} = \rho \cdot u_m \cdot A_c \tag{2.33}$$

where $\dot{m}$ and u_m are flow mass and velocity, respectively and $A_c = \frac{\pi D^2}{4}$ is a cross section, which is assumed uniform over control volume.

where, $x_{fd,t}$ is the entry region length, $[\mathrm{m}]$, D is the diameter, $[\mathrm{m}]$, Re is the Reynolds number and Pr is a Prandtl number.

If Pr $>$1 the thermal entry region is longer then the hydrodynamic entry region, which is defined as: $\left(\frac{x_{fd,h}}{D}\right)_{laminar} \cong 0.05 Re_D$, if Pr$<$1 the inverse is true.

At turbulent flow, thermal conditions are almost independent from Prandtl number and a value of $\frac{x_{fd,t}}{D} = 10$ can be assumed (Incropera and De Wit, 2002).

The radial profile of the temperature will differ according to the imposed boundary conditions (see how the difference between heat flux and constant temperature conditions determine temperature profile Figure 2.9).

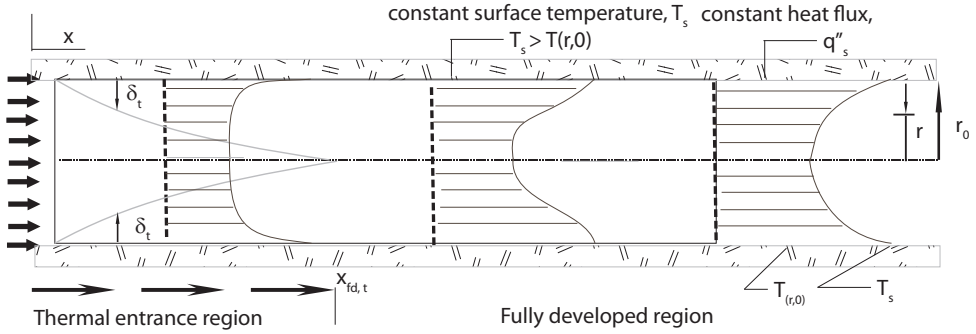

Figure 2.9: Realisation of a thermal boundary layer in a circular tube. - The shape of the fully developed temperature profile, T(r,x) differs accordingly to the imposed conditions: constant temperature (a) or constant heat flux (b). For both profiles the temperature exceeds the entrance temperature with increasing x. Adopted from (Incropera and De Wit, 2002).

The Water Mean Temperature in Fully Developed Conditions

The mean temperature, in the fully developed conditions, also called the bulk temperature, changes according to the Newton's law of cooling (see Figure 2.9). The mean temperature depends on the rate of the thermal energy advection integrated over cross section, as in equation 2.36:

$$T_m = \frac{2}{u_m r_0^2} \int_0^{r_0} uTrdr \tag{2.36}$$

where T_m is the mean temperature, [K], u_m is the mean velocity,$[\ \mathrm{m/s}]$, r_0 is the geometrical radius, $[\mathrm{m}]$, r is the thermally relevant radius, $[\mathrm{m}]$ (see Figure 2.9). T_m provides the rate at which thermal energy is advected with the fluid as it moves along the tube.

2.6.1 Local Convection Coefficients

If the soil temperature at the pipe wall does not change in time, the mean water temperature adopts to the soil temperature with an increasing length (x coordinate) and in the flow direction. If the heat transfer occurs, the value of T_m increases as the energy from the outside surface to the pipe wall continues to flow, ($T_s > T_m$); it decreases with x when the opposite is true ($T_s < T_m$). The rate of changes will depend on the local convection coefficient:

$$q_{dw,s} = h(T_s - T_m) \tag{2.37}$$

where q'' is a heat flux due to convection, $[\mathrm{W/m^2}]$, h is a convection heat transfer coefficient, $[\mathrm{W/m\ K}]$. Figure 2.9 shows that in the thermally fully developed conditions the relative shape of the temperature profile T(r) remains the same.

The convection heat transfer coefficient varies significantly with length at the entrance region, where its value is large. After passing that region, convection heat transfer coefficient decays rapidly to achieve a constant value in the thermally fully developed conditions.

Constant Pipe Wall Temperature

If the pipe wall temperature varies negligibly for the longer time interval, we can assume a constant surface temperature. The heat transfer in such conditions is calculated from the formulae

$$\frac{T_s - T_m(x)}{T_s - T_{m,i}} = exp\left(-\frac{Px}{\dot{m}c_p}\bar{h}\right) \tag{2.38}$$

where T_s is constant, $\bar{h}$ is an average value of convective heat transfer coefficient. From the inlet to the arbitrary point in the x the temperature decays exponentially as shown in Figure 2.10. The total heat transfer due to convection is calculated from:

$$q''_{dw,conv} = \bar{h}A_s\Delta T_{lm} \tag{2.39}$$

where T_{lm} is a log-mean average temperature difference, calculated from

$$T_{lm} = \frac{\Delta T_o - \Delta T_i}{ln(\Delta T_o/\Delta T_i)} \tag{2.40}$$

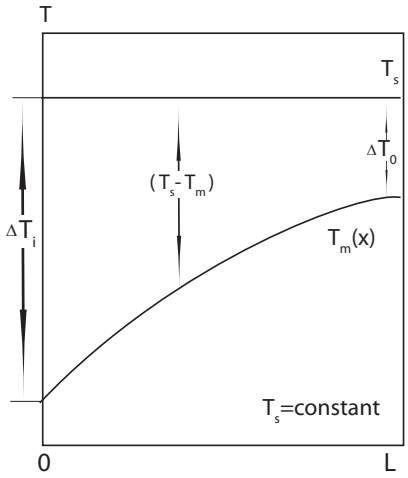

Figure 2.10: A variation in temperatures in a tube subjected to a constant surface temperature. - The temperature difference between a surface and bulk of water encountered at x axes. Adopted from (Incropera and De Wit, 2002).

Stagnant Water in a Pipe

When water resides longer in a pipe, we deal with two different heat transfer coefficients at inner and outer sides of the pipe wall. The temperature distribution through the pipe wall is logarithmic, as sketched in figure 2.11.

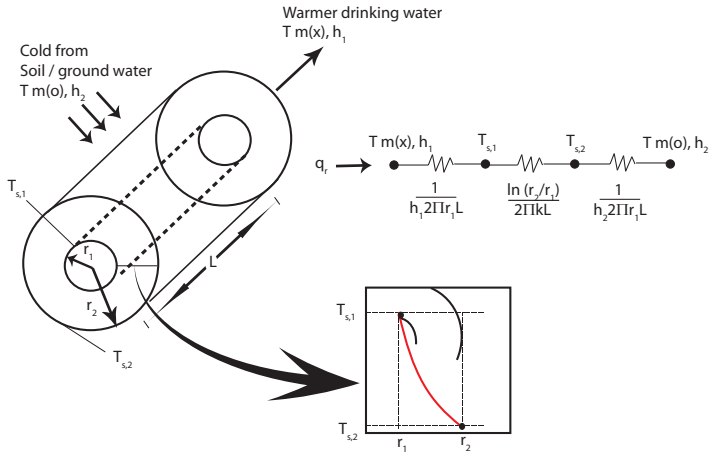

Figure 2.11: The thermal resistance due convective and conductive surface conditions in a pipe. - The thermal resistance due different heat transfer coefficients and surface interface. The heat flux is in radial direction. Adopted from (Incropera and De Wit, 2002).

The resulting heat transfer rate is given in equation 2.41:

$$q_{dw,stag} = \frac{2\pi Lk(T_{s,1} - T_{s,2})}{ln(r_2/r_1)} \tag{2.41}$$

where T_s is pipe wall outside and inside temperature, [K], h is convection coefficient of the fluid outside and inside of the pipe, $[\mathrm{W/m\ K}]$, k is conduction coefficient, $[\mathrm{W/m\ K}]$ (obtained from the Fourier's law of cooling). Both parameters are defined by 1,2 subscripts, respectively for outside and inside.

At laminar flow the heat transfer rate yields

$$q_{dw,lam} = \frac{(T_{s,1} - T_{s,2})}{R_{tot}} \tag{2.42}$$

where T_s is pipe wall outside and inside temperature, [K], h is convection coefficient of the fluid outside and inside of the pipe, $[\mathrm{W/m\ K}]$, k is conduction coefficient, $[\mathrm{W/m\ K}]$ (obtained from the Fourier's law of cooling). Both parameters are defined by 1,2 subscripts, respectively for outside and inside of the pipe. The thermal resistance for radial conduction during laminar flow yields

$$R_{tot} = \frac{1}{2\pi r_1 L h_1} + \frac{ln(r_2/r_1)}{2\pi Lk} \tag{2.43}$$

If the groundwater is present at the outer surface of the pipe:

$$R_{tot} = \frac{1}{2\pi r_1 L h_1} + \frac{ln(r_2/r_1)}{2\pi Lk} + \frac{1}{2\pi r_1 L h_2} \tag{2.44}$$

2.6.2 Heat Transfer at Laminar Flow in a Pipe

In the laminar flow, where the velocity profile is constant, (see Figure 2.9), assumptions relevant to the thermal fully developed region apply. Namely, there is no axial conduction and no radial advection and we can estimate the total heat transfer based on the Nusselt number. The Nusselt number for the fully developed thermal conditions is constant, as it is independent on Reynolds and Prandtl number. At constant surface temperature conditions it equals:

$$Nu_D = 3.66 \tag{2.45}$$

This value can be used to determine the local convection coefficient, h, at the entrance region, considering the average water temperature $T_m = (T_{m,i} + T_{m,o})/2$ and using dependence: $\overline{Nu}_D \equiv \overline{h}D/k$.

Namely, there is a direct relationship between the Nusselt number Nu and h, convection coefficient:

$$N_u = \frac{h \cdot D}{k} \tag{2.46}$$

with D the diameter. For pipes with a smooth wall N_u can be described as a function of the Graetz number (Gz), Reynolds number (Re) and Prandtl number (Pr).

At the entry region conditions the temperature and velocity profiles develop simultaneously. The Nusselt number in theory is infinite at x=0 and decays asymptotically with increasing x. In this conditions the Nusselt number depends on viscosity and on the Prandtl number. In such case, the Nusselt number decreases with increasing Pr until the fully developed thermal conditions prevail. The average convection coefficient can be calculated using Kays and Perkins (1985) correlation:

$$\overline{Nu}_D = 3.66 + \frac{0.0668(D/L)Re_D Pr}{1 + 0.04[(D/L)Re_D Pr]^(2/3)} \tag{2.47}$$

However, according to Incropera and De Wit (2002), at the entry region it is more suitable to use the Sider and Tate (1936) correlation:

$$\overline{Nu}_D = 1.86 + \left(\frac{Re_D Pr}{L/D}\right)^{1/3} \left(\frac{\mu}{\mu_s}\right)^{0.14} \tag{2.48}$$

for $0.60 \leq Pr \geq 5$ and $0.0044 \leq \left(\frac{\mu}{\mu_s}\right) \geq 9.75$, provided that $\overline{Nu}_D \leq 3.66$.

2.6.3 Heat Transfer at Turbulent Flow in a Pipe

At the turbulent flow in a pipe the Equation 2.56 is still valid but a new definition of Nusselt number is needed. The Dittus-Boelter equation is a preferred expression for computing the local Nusselt number in fully developed (thermally and hydrodynamically) turbulent flow for a smooth circular pipe (Winterton, 1998).

$$Nu_D = 0.023 Re_D^{4/5} Pr^n \tag{2.49}$$

where n=0.4 for heating ($T_s > T_m$) and 0.3 for cooling ($T_s < T_m$). The expression has been applied in the range of $0.7 \leq Pr \geq 160$ and $Re_D \geq 10'000$, provided that $\frac{L}{D} \geq 10$. This relation works well for small temperature differences. For larger property variations, Incropera and De Wit (2002) suggest using Sider and Tate (1936) relation:

$$Nu_D = 0.027 Re_D^{4/5} Pr^{1/3} \left(\frac{\mu}{\mu_s}\right)^{0.14} \tag{2.50}$$

The equation introduces error as large as 25% in flows where the bigger Reynolds number prevails. For such conditions error can be reduced to less than 10% by using Gnielinski (1976) formulae, which also can be applied to the transition region:

$$Nu_D = \frac{(f/8)(Re_D - 1000)Pr}{1 + 12.7(f/8)^(1/2)(Pr^{2/3} - 1)} \tag{2.51}$$

where f, the friction factor can be obtained from the Moody diagram or calculated for smooth pipes. In turbulent flow the heat transfer coefficient increases with increasing roughness of a pipe wall. The f increase is proportionally larger then h. The correlation is valid for $0.5 \leq Pr \geq 2000$ and $3000 \leq Re_D \geq 5x10^6$ and can be applied for both constant surface temperature and uniform heat flux.

If entry region is short and the turbulent flow prevails it is reasonable to assume the average values of the Nusselt number for the entire tube. The typical error introduced by this assumption is less than 15%.

2.6.4 Drinking Water Temperature in a Pipe Model

If the water discharges are at a fixed lower temperature then changes in the resulting drinking water temperature can be calculated as follows:

$$\frac{\delta T}{\delta t} = \frac{2 \cdot U}{\rho \cdot r \cdot C_p} \cdot (T_{wall} - T) \tag{2.52}$$

with r the pipe radius (= 0.5 pipe diameter D), [m] and the U,[-], the lumped heat transfer coefficient. The lumped heat transfer coefficient is obtained from a superposition of the partial heat transfer coefficients of a pipe wall and water (similarly, as was shown in Figure 2.11). The lumped heat transfer coefficient yields:

$$U = \frac{1}{\frac{D_{pipewall}}{k_{pipewall}} + \frac{D_{pipe}}{k_{water} \cdot N_u}} \approx \frac{1}{D_{pipe} \cdot \left(\frac{1}{k_{pipewall} \cdot 10} + \frac{1}{k_{water} \cdot N_u} \right)} \tag{2.53}$$

with the thickness of the pipe wall D pipe wall, which is $\approx 10\%$ of the pipe diameter D_{pipe}. Therefore the l ratio yields

$$l = \frac{k_{water}}{10 k_{pipewall}} \tag{2.54}$$

Equation 2.52 yields the heating time of the drinking water in the pipe

$$\frac{\delta T}{\delta t} = \frac{h}{r^2 \cdot \left(l + \frac{1}{N_u}\right)} \cdot (T_{wall} - T) \tag{2.55}$$

At the condition that T(t=0) = T_0 and T(t=T) = T_{wall}, there is an analytical solution for the heating by convection in a pipe[1]:

$$T_t = T_{wall} - (T_{wall} - T_0) \cdot e^{\frac{h}{r^2 \cdot \left(l + \frac{1}{N_u}\right)} \cdot t} \tag{2.56}$$

2.6.5 Principles of Drinking Water Temperature Modelling

In this chapter, we have introduced the two main research and models that will be referred to frequently in this thesis: the soil model developed by Van Der Molen et al. (2008) and the piped water temperature model developed by Blokker and Pieterse-Quirijns (2009). The soil model (Section 2.5.3 Equation 2.30) analyses the impact of weather interventions on a pipe within a drinking water supply system. The model uses a one dimensional, vertical heat flux to predict the heat available at the pipe burial depth by calculating the density of heat that has been transferred from the upper to the deeper soil layers.

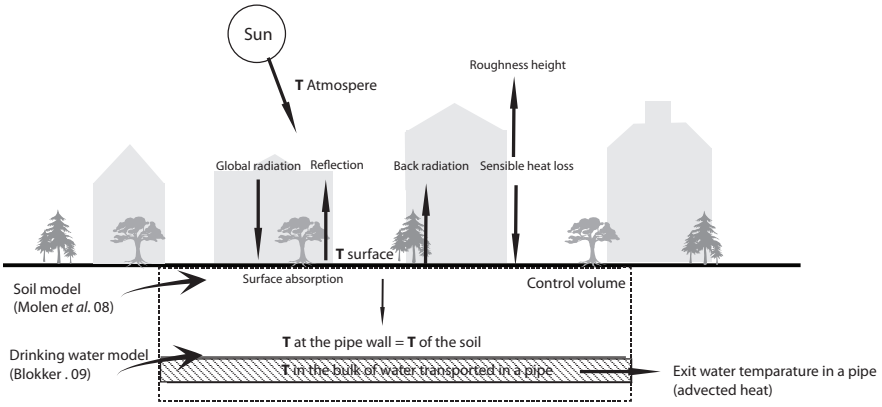

Figure 2.12: Schematic representation the soil temperature model developed by Blokker and Pieterse-Quirijns (2009). - The conceptual representation of the main modelling principles.

Blokker and Pieterse-Quirijns (2009), assume that so obtained soil temperature at burial depth is equal to pipe wall temperature. Thereby, Blokker and Pieterse-Quirijns (2009) use the soil temperature calculated by Van Der Molen et al. (2008) model to obtain the log mean water temperature in a drinking water pipe (Section 2.6.4 Equation 2.56) .

[1]The formulae is based on work of Blokker and Pieterse-Quirijns, from KWR–Dutch Watercycle Research Institute. Blokker and Pieterse-Quirijns (2009) have found out that the time needed for the drinking water to reach the soil temperature is shorter than the travel time of the drinking water from the production station to the customers' taps. Authors have confirmed their hypotheses with results from the experiment conducted in Zandvoort during summer months in 2008.

According to Blokker and Pieterse-Quirijns (2009) methodology, the pipe wall temperature can be easily obtained directly from the soil model and indirectly from the weather data and extrapolated to several distinct points in a network. A combined impact from such input points constitute a vertical input to a drinking water network (see scheme of this relation in Figure 2.12).

Theoretical Rationale for Coupling

The dynamic equilibrium is a condition in which the piped drinking water receives or releases heat or cold in such way that is follows with a time lag the atmospheric conditions (Medrano, 2008). This time lag in case of a pipe will be relative to the surface temperature and soil diffusivity.

As soon as heat is discharged or withdrawn in another way than vertical, such as by the forced convection in turbulent flow, when the mixing of phases is intensified, the water can be defined as out of its natural equilibrium (see Figure 2.13).

When the water temperature deviates from the equilibrium temperature changes in heat transfer with the soil is invoked. The heat fluxes can be calculated from the difference between the natural heat exchange during the dynamic equilibrium (stagnant water) and a real exchange altered by heat discharged to the pipe by the incoming bulk of water.

Data Based Coupling

The main output of the soil modelling is a temperature scalar which can be assumed constant for a given time interval. This constant temperature is an upper boundary of the temperature of the water flowing in a pipe. The gradient between the temperature of the pipe wall and water is defined by the rate at which the heat is transferred to the drinking water this in turn depends on the thermal diffusivity of water in a network and on a system hydraulics. By coupling hydraulic, soil and piped water temperature models our knowledge on vertical temperature distribution in soil can be extrapolated into a horizontal temperature distribution in a drinking water supply network.

Clearly, in order to realize the task of defining the temperature distribution in a drinking water network, large-scale variability of the the network should be accounted for. To this end, local or point measurements should be contrasted with groundwater models and GIS analysis. However, the soil temperature can be still translated as an uniform (scalar) input in a network. In this thesis we will estimate error of such simplification. Several platforms can be used to calculate the combined water temperature and hydraulics. In this thesis we use Epanet 2 platform (Rossman, 2000).

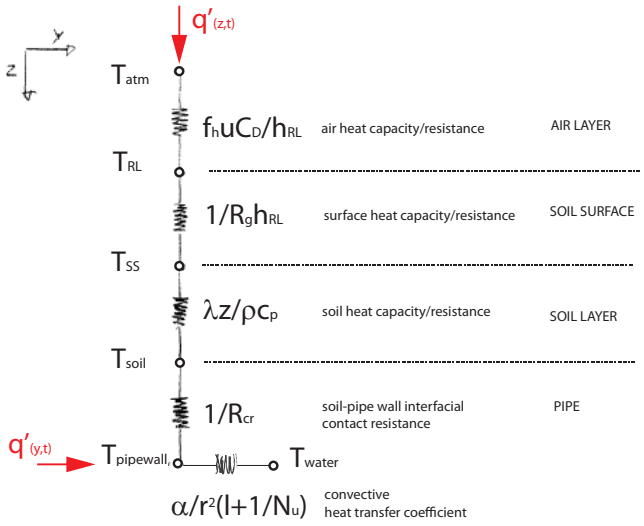

Figure 2.13: A scheme of a thermal resistance network of a coupled models. - The calculated vertical and horizontal heat-flux and resulting temperatures against the models' resistance parameters.

Section	Denomination	Input sources	Input parameters	Output	Literature source
Section 2.5.3	Soil temperature model	Breda experiment	(i) meteorological data (ii) soil temperature	soil temperature	Molen *et al*,2008
Section 2.6.4	Drinking water temperature model	soil temperature model	(i) soil temperature = pipe wall temp.	exit water temperature in a pipe	Blokker and Pieterse-Quirijns, 2010
Chapter 3	Drinking water in a network	Epanet, MSX Network model Measurements	(iii) heat transfer rates (iv) hydraulics and geometry (demands, pipes, etc) (v) incoming water temperature (vi) initial temperatures (vii) temperature patterns	transport of the temperature in a network	This thesis

Figure 2.14: Data flow based coupling of the soil and drinking water temperature models. - Data flow between the models that have been found in the literature and their input and output relations.

Blokker and Pieterse-Quirijns (2009)) predict temperature changes in the horizontal direction, in a pipe, by means of Epanet MSX and basic ODE formulations for the heat exchange between the constant temperature of a pipe wall and the variable drinking water temperature. The approach will be extended in this thesis. The exemplary data flow between the models is given in Diagram 2.14.

3

Materials and Methods

3.1 Introduction

The primary goal of this research is to explore how network hydraulic influences the temperature of the drinking water. The secondary aim is to establish linkages between climate conditions, network characteristics and the drinking water temperature. To achieve these goals, we have used a model instrument consisting of two heat transfer models representing weather and soil conditions, and two network models calculating hydraulics and water quality. In order to validate the models' an experiment was organised.

In the next parts of this thesis, we will explain how the models of Van Der Molen et al. (2008) and Blokker and Pieterse-Quirijns (2009), described in chapter 2, will be applied to Waternet conditions and what was the validation procedure.

Figure 3.1 shows a possible compilation path and sequential coupling of the inputs and outputs originating from the models of Van Der Molen et al. (2008) and Blokker and Pieterse-Quirijns (2009). In each phase the modelling simulations are validated with observed temperatures, or calibrated if necessary (as explained in section 2.6.6 in chapter 2). The figure shows also that in order to use the model of Van Der Molen et al. (2008) or Blokker and Pieterse-Quirijns (2009), boundary conditions and initial temperatures are needed. Thus, for the purpose of validation/calibration it was decided to provide a novel experimental data set.

The architecture of an experimental set–up was based on the research of Van Der Molen et al. (2008) and Blokker and Pieterse-Quirijns (2009). The novelty of the experiment was to provide simultaneous measurements of the drinking water and the soil temperature at several points at West part of Diemen Noord, the Netherlands and in one vertical, at the three different depths below the surface. A secondary

aim of the experiment, apart from testing the models at the representative smaller subdivision of the Waternet supply network, was to revise what realistic temperature gradients can we expect to find in a network at given climatic conditions.

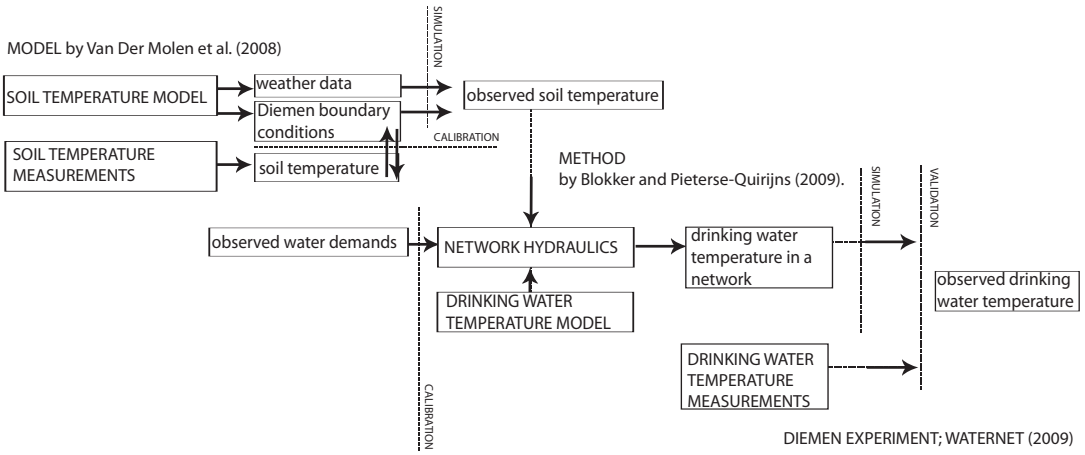

Figure 3.1: A parse tree applied in this thesis to estimate and experimentally validate models relevant to drinking water temperature in a network. - Methodology was partially adopted from the (Van Der Molen et al., 2008) and (Blokker and Pieterse-Quirijns, 2009).

In order to estimate an influence of the hydraulics on the heat and mass transfer in a pipe, the Waternet hydraulic model was calibrated. To this end, water meters were deployed at eight different points in a thoughtfully selected houses in west section of the Diemen Noord supply network. The demand data have been used for the water quality (temperature) calculations.

This chapter main focus is to present experimental and modelling methodology but also to describe particularities, a rationale of the choice of site and instrumentation; sampling rates and set-up of the experiment.

3.2 Monitoring Site Selection Criteria

Waternet drinking water supply network comprises of mains of a different fabric: 30% of the network pipes are cast iron, 20% ductile iron, 25% PVC and 25% other[1], many of which the pipes are overdimensioned for customers' demands[2]. The location qualified to the experiment was selected according to how this variety of pipe sizes and fabrics was manifested at a site (see Table 3.1) and how well is the

[1] polyethylene (8%), copper (8%), steel (4%), concrete (4%), glass fiber reinforced plastic (1%)
[2] The network is designed according to fire hydrants demands.

site islolated from the rest of the network; so that the total incoming and outgoing volume of water to and from the section could be estimated.

3.2.1 Diemen as a Part of Waternet Supply Network

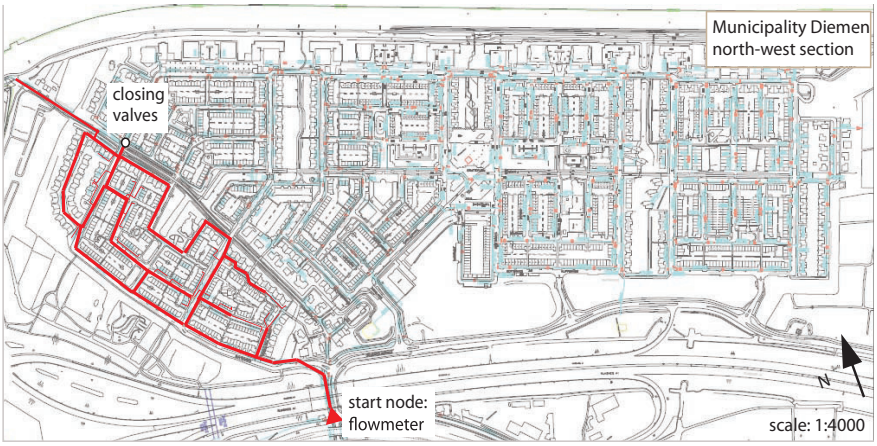

Figure 3.2: The selected distribution network of West part of Diemen Noord. - A selected section of the distribution grid at West part of Diemen Noord indicated by red lines.

Such sought section was the North-West part of the Diemen network. As indicated in Table 3.1 the West part of Diemen Noord is a representative subdivision of the Waternet distribution network. It is equipped with two flow meters installed at the two incoming, main pipelines at the entrance to the network section. Furthermore, it was workable to close one of the outgoing valve at the north end during the course of the experiment, which allowed a better isolation of this section from the remaining supply network (see Figure 3.2).

3.2.2 Pipe Fabric and Pipe Characteristics

Table 3.1: Characteristics of the Waternet Distribution Network vs. characteristics of the West part of Diemen Noord supply section.

Pipe diameter classes (mm) Waternet			Diemen	Pipe length classes (m) Waternet			Diemen
<100		25%	33%	<5		6%	7%
100	-200	53%	36%	5	-10	12%	14%
200	-300	12%	30%	10	-50	47%	40%
300	-500	7%	-	50	-100	22%	30%
500	-800	3%	-	100	-500	13%	8%
800	-1000	0%	1%	500	-1000	0.2%	-
1000	-1200	0.6%	-	<1000		0.04%	-

Similarly, to the pipe types and characteristic present at the total Waternet distribution grid; the 62% of distribution pipes in the West part of Diemen Noord supply network are made from PVC, 35% from cast iron or copper and 3% other.

3.3 General Information on Diemen

Topographical Influences on Heat Exchange

The municipality of Diemen is situated at the east of Amsterdam. West part of Diemen Noord is a polder system, surrounded by a canal, where ground level is maintained at the NAP -1.95 m, the groundwater is around 1 m below the surface level and the pipes are buried at approximately 80 cm below the surface level. Other Diemen's urban topology and the annual-mean meteorological variables are the same as the ones found in Amsterdam. Those parameters are summarized in table 3.2.

(a) Detached houses (section A).

(b) Semi-detached old houses (section B).

(c) Terraced houses (section C).

Figure 3.3: A side-view photo of a three typical dwellings in west part of Diemen Noord. Source: Google maps. Retrieved on 21.04.2010, from http://maps.google.nl/maps.

Table 3.2: General topologies of Diemen.

location:	West part of Diemen Noord	Units
Mean air temperature:	9	$^{\circ}\mathrm{C}$
Mean pressure:	101.13	kPa
Mean incoming long wave radiation:	358.57	$\mathrm{W/m^2}$
Regional albedo:	0.16	
Latitude:	52.21N	
Azimuth(north based):	270	

Source: Wikipedia, the free encyclopaedia. Retrieved on 01.10.2009, from http://en.wikipedia.org/wiki/Amsterdam.

West part of Diemen Noord consist of detached, semi-detached and congested terraced housing made mostly from concrete and occasionally from bricks (see Figure 3.3). The build-up area is uniform in height (1-2 storeys). Most roofs are gamble covered with bituminous tiles. Seventy percent of the selected area is paved with occasional patches of green (see Figure 3.4).

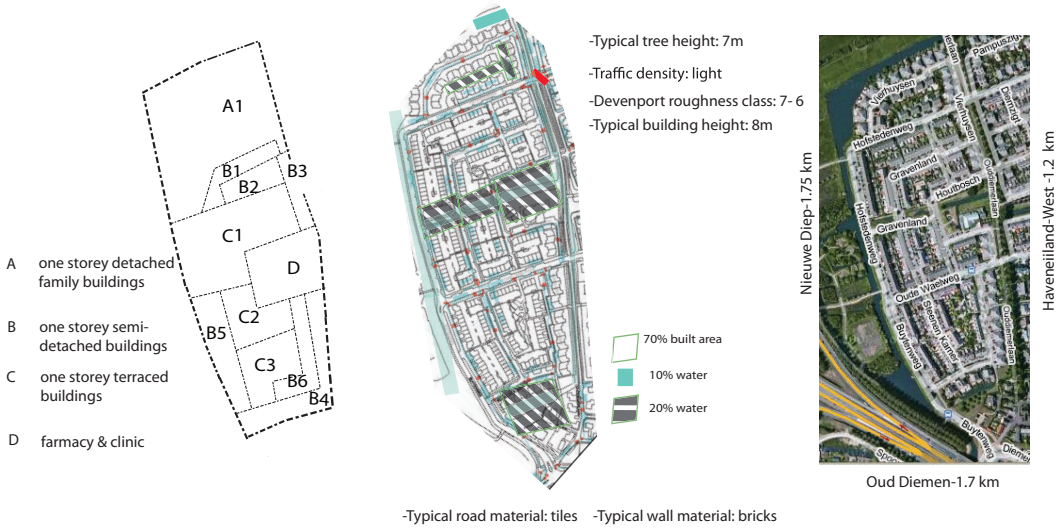

Figure 3.4: The type of housing, local settings and a nearest distance to the topographic change; west part of Diemen Noord. - The first map shows a schematic division of the site according to the prevailing type of buildings. The second map shows the most relevant features of Diemen urban topology. The shaded areas represent water bodies and vegetation, such as grass land, shrubs, single trees and parks. The unshaded part of the map represent built up area. The third picture is an aerial photograph of west part of Diemen Noord, with indication of the distance to the nearest topographic change. Source: Waternet and Google maps. Retrieved on 21.04.2010, from http://maps.google.nl/maps.

The building spacing to height ratio is 0.5-1.5, thus the impact of the urban climate on the heat partitioning can be significant (see Figure 3.3 and compare with the Devenport classes in Appendix A.5). Additionally, most of the surface is impermeable, which affects the moisture of the ground and hence its humidification and evaporative cooling potential. According to (WMO, 2008), at the site with the narrow building spacing and impervious coverings, the flow regime types and thermal controls (solar shading and longwave screening) can be significantly changed.

Sources of Water Supply

The water that reaches west part of Diemen Noord originates in more than 90 % from the Bethunepolder; from the Weesperkarspel treatment plant, in specific (see Figure 3.5). The mixing zone of the two source waters is shown in Figure 3.5.

Travel Time from the Source

Apart from having different quality characteristics (see Appendix A.4 for details on quality aspects), the water from the Bethunepolder resides longer in the network (Diemen Noord is marked with black squares in Figure 3.5) which influences the temperature of the distributed water in a way that it has more time to adjust to the temperature of the bounding soil.

As it can be seen from hydraulic calculations presented in Figure 3.5, it takes roughly 15-20 hours for the water from Weesperkarspel to reach parts of west part of Diemen Noord.

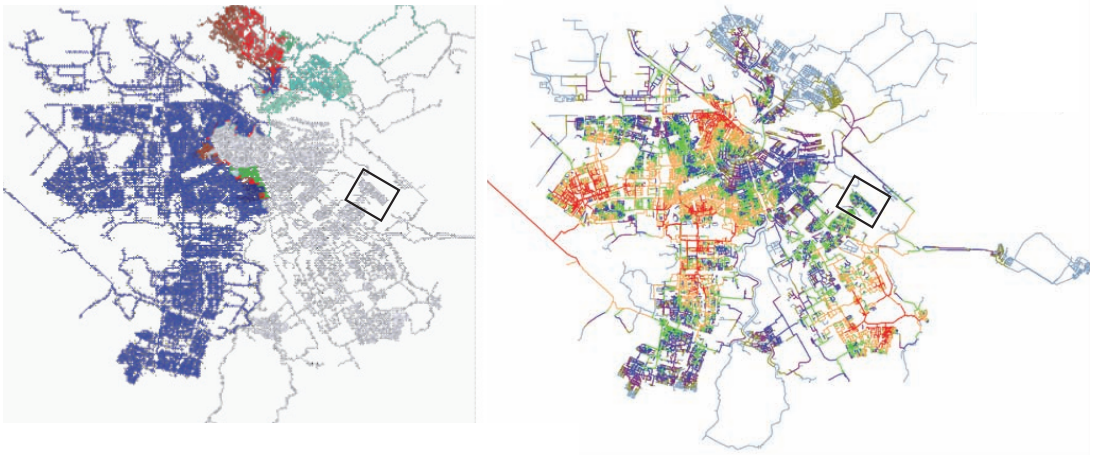

Figure 3.5: Mixing zones and average age of the water from Leiduin and Weesperkarspel. - The left picture shows the water origins. The probability that the water comes from Weesperkarspel: blue (less than 1%), green/red (40-50%), white (more than 90%). The right picture shows estimated average hydraulic residence time in Waternet network. The colours in the legend represent hours during which water remains in the pipes: mininum residence time, red (<5 hours), mininum residence time, grey (>30 hours and more). Source: Waternet.

3.4 Soil Temperature Measurements

The interest of the experiment was to capture variations of the temperature of the drinking water due to atmospheric heat fluxes and various demands in the supply network. To this end, four distinct locations in the west part of Diemen Noord area have been selected. Intention behind choosing multiple monitoring sites was to: (i) estimate the influence of urban topology on an energy conservation and changes in drinking water temperatures, (ii) determine vulnerability of the distribution network to climatic changes, (iii) capture how the changes in the temperatures progress in a network.

In order to ensure sound results, we have followed (WMO, 2008) guidelines and put efforts to (i) situate the sampling points outside of micro climatic influences of: individual buildings, trees, roads,

streets, and to (ii) obtain measurements that integrate the mix of local climatic effects, characteristic for a certain surface cover, size and spacing of buildings and streets and load due to traffic and heating.

The aim was to obtain the temperature from different mediae: soil, water and different pipe wall types. A system of coupled thermistors, were chosen for this purpose as a relatively accurate and inexpensive measuring equipment that work equally well at different materials. In addition, vented transducers were deployed to measure ground water temperature and levels at several distinct points. Temperature of soil and drinking water were measured with the NTC 100k Ohm sensors[1]. Technical details can be found in Appendix A.7. To measure the temperature and the level of groundwater nearby the soil and drinking water monitoring locations (see Figure 3.16) vented transducers, commonly known as groundwater divers, were installed at a number of piezemeters[2]. In specific, Mini Diver electrical pressure vented transducers were used. Technical details can be found in Appendix A.7.

3.4.1 Sampling Points' Characteristics

At each sampling point, five temperature sensors were installed. The sensors measured the temperature of the drinking water, pipe wall and the soil above the pipe, simultaneously. Locations represent a single class of the urban climate zone (see Table 3.3 and Appendix A.5), feature a different cover type, combination of pipe diameter and pipe type. Locations 1-3 are paved with concrete tiles whereas location 4 is partially underneath a concrete slab and partially covered by grass. Location 3 is situated between two drainage canals in the vicinity of the grass patches. There is a pharmacy nearby this location, which will result in distinct demand patterns.

Table 3.3 lists urban properties of the west section of the west part of Diemen Noord. Specifically, (i) urban canyon orientation responsible for the sunshine intensity and duration, (ii) urban climate zone, indicating the intensity of mixing of moisture and heat fluxes at the surface (the higher the zone class the less the mixing) , and (iii) the percentage of the waterproofing coverings, indicating the prevalent heat fluxes (the more waterproofing the smaller the latent heat flux).

[1] NTC (Negative Temperature Coefficient) Thermistors are semiconductor resistors in which resistance decreases with increasing temperature. Commercial name: NTC Honeywell Sensor 192-104QET-A01

[2] Waternet supply pipes are submerged under the groundwater in 70%. The west section of west part of Diemen Noord is not an exception. There are many reasons to believe that groundwater temperature will have an important effect on the resulting drinking water temperature.

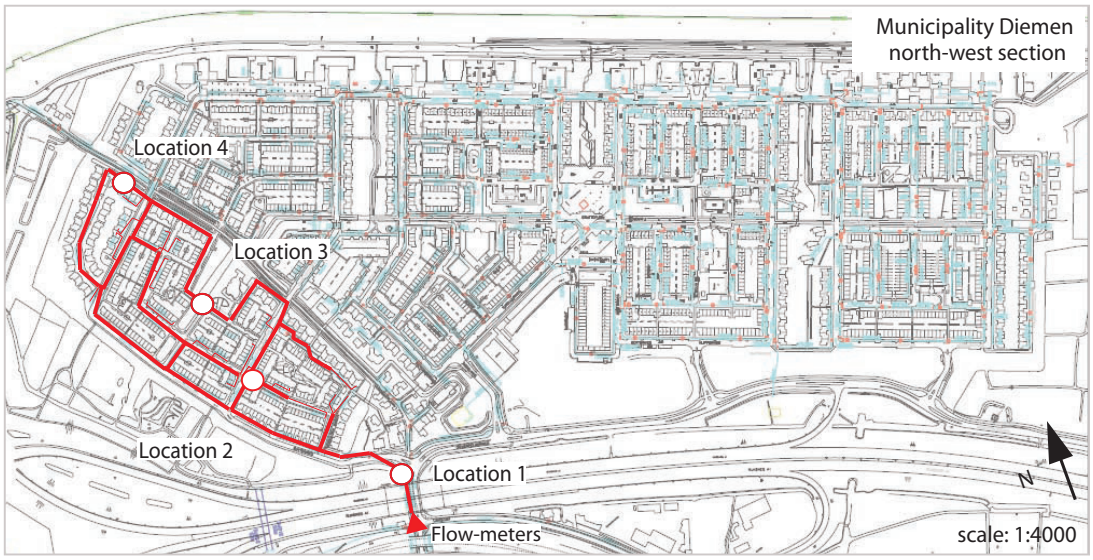

Figure 3.6: location of 4 sampling points in west part of Diemen Noord. - Each point is situated in a different micro-environment and at pipes of a different diameter and fabric.

Table 3.3: Information on urban and pipe characteristics at the monitoring points collected during the site survey. Please refer to chapter 2 and Appendix A.5 for explanation of the determinants.

location:	1	2	3	4
Street name:	Buitenweg 2	Oude Waelweg 6	Houtbosch 39	Vierhuizen 39
Canon orientation:	West: Azimuth(270)	East: A(90)	East: A(90)	South: A(180)
Davenport class:	6	6	6	5
Urban climate zone:	5	3	6	5
Roughness class:	6	7	5	6
Hight-Width aspect ratio:	0.2-0.6	0.5-1.5	0.1-0.5	0.2-0.6
Impermeable surface [%]:	35-65	70-85	<40	35-65
Pipe diameter:	250	250	125	125
Pipe material:	pvc	cast iron	pvc	cast iron

Please refer to chapter 2 and Appendix 3 for explanation of the determinants.

It was expected that during the short measuring campaign we anticipated, because of reduced global radiation in autumn/winter seasons and more precipitation, which may have a cooling effect, the influence of the urban topology, Urban Heat Island in specific, will be less significant. Thereby, an vulnerability of the distribution network to climatic changes would be difficult to verify. Thus, in order to

capture how the changes in the temperatures progress in a network, we narrowed our focus to how the temperature evolves in vertical at four distinctly different location.

Each location features a different type of cover whilst the same soil layers are assumed at all locations (see Table 3.4)[1]. The shallow layers are assumed to consists of dry sand and deeper layers are assumed to be saturated sandy soils.

Because of the bigger thermal inertia of CI pipes, locations 2 and 4 should exhibit significant changes during the day (look at Equation 2.19 in chapter 2 for explanation).

Table 3.4: Thermal characteristics of the surface at the monitoring points.

location:	1	2	3	4
Receiving layer:	concrete tiles	concrete tiles	concrete tiles	grass
Pavement thickness, cm:	10	5	5	-
Heat capacity, $\mathrm{J/m\ K}$:	2.11	2.11	2.11	1.4-3
Thermal conductivity, $\mathrm{MJ/m^3\ K}$:	1.51	0.67	0.67	0.25-1.6
Albedo, -:	0.35	0.10	0.10	0.26
Emissivity, -:	0.91	0.71	0.71	0.95
Soil shallow layer:	dry sand	dry sand	dry sand	dry sand/humus
Heat capacity, $\mathrm{J/m\ K}$:	1.3	1.3	1.3	1.3
Thermal conductivity, $\mathrm{MJ/m^3\ K}$:	1.5	1.5	1.5	1.5
Soil below deep layer:	wet sand	wet sand	wet sand	wet sand
Heat capacity, $\mathrm{J/m\ K}$:	2.5	2.5	2.5	2.5
Thermal conductivity, $\mathrm{MJ/m^3\ K}$:	2.5	2.5	2.5	2.5

Please refer to chapter 2 and Appendix A.5 for explanation of the determinants.

[1]The values of the albedo, emissivity, pavement heat capacity and thermal head conductivity were taken from (Oke, 1982). The values of the soil heat capacity and thermal conductivity were taken from (Van Der Molen et al., 2008). The soil properties are estimated homogeneous at all locations.

3.4.2 Arrangement of the NTC Sensors

The core of the experimental set-up consists of five NTC sensors that are organized at the three different depths below the surface (5cm (S5), 50cm (S4) and 100cm (S3)) and at the pipe wall (S2) (see Figure 3.7). The temperature of the drinking water is measured in the middle the pipe cross-section (S1) with the same type of sensor, NTC thermistor.

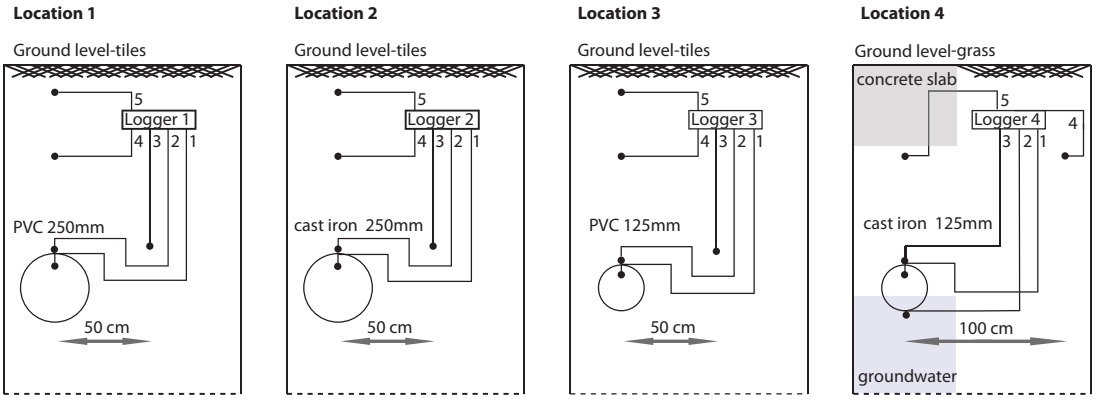

Figure 3.7: An experimental set-up of the NTC temperature sensors. - Every sensor node consists of five temperature sensors, measuring the temperature in the pipe, at the pipe wall, in the soil layer next to the pipe and in two intermediate soil layers. The sensor node has a built in GSM module so that data can be transferred via a GSM network to the central server.

(a) Excavation and drainage.

(b) Installing the pipe clamp with the opening for the sensor.

(c) Mounting sensors S2-S5 in the soil.

Figure 3.8: Photographs taken during the NTC thermistors' installation.

There are two sensors at the pipe depth S3 and S2. Sensor S2 measures soil temperature and is

located in soil at a distance of $50\mathrm{cm}$ from the S3, which measures pipe wall temperature. The aim of such set-up of S2 and S3 was to obtain the value of a thermal resistance at the soil and pipe wall interface. The five sensors per location are connected to one common data logger (type ElliTrack-T38), which has a built in GSM module via which the collected data can be transferred to the central server (see Figure 3.7). This setup is repeated at four monitoring points (see Figure 3.16).

The sensor S1 could not be directly inserted inside of a pipe. In order to protect the quality and conform with the drinking water guidelines, the sensor was tightly mounted in a sterilized metal tube. This metal tube, called insertion tube, was then mounted on a pipe clamp (see Figure 3.8b).

Sensors S3, S4 and S5 were inserted in the undisturbed soil (see Figure 3.8c). The excavation was filled gradually with soil and compacted for a duration of about 10 minutes by a special compacting equipment, to cause re-orientation of the soil particles into a denser configuration. Annex provides some photographs taken during the preparation of the experiment (see Appendix A.7). The installation of the NTC sensors at four locations took two days (16 hours) and a working team of three people (plus two supervisors).

3.5 Soil Model Implementation

The soil model of Van Der Molen et al. (2008), was implemented with settings and state parameters as listed in tables 3.3 and 3.4, and the observed temperatures registered during the experiment in Diemen at different depths in soil (see Figure 4.10 in chapter 4) as initial values. Model simulating the soil temperature at the pipe burial depth was verified with the real soil temperature measurements at the pipe burial depth[1].

Input data

What is characteristic of this soil model, is that the same values of weather inputs are submitted to the model at all individual points, while the soil thermal conditions (model states) and boundary values (measured temperatures) are diversified for every location (see Table 3.9). All variables are interpolated for each minute of the model time step and a spatial grid of $5\mathrm{cm}$. The boundary values are also recalculated at every model time step. Based on this input, model calculates the temperature of soil at each location (see Figure 3.9). Knowing the output of this modelling allow us to estimate (i) temperature differences between individual locations, (ii) error we introduce when we assume average soil temperature in the network calculations. Validation results are reported in chapter 5.

[1] A soil model was similar to MATLAB which is included in Appendix A.12. The proper code can be obtained by contacting M. Blokker from KWR.

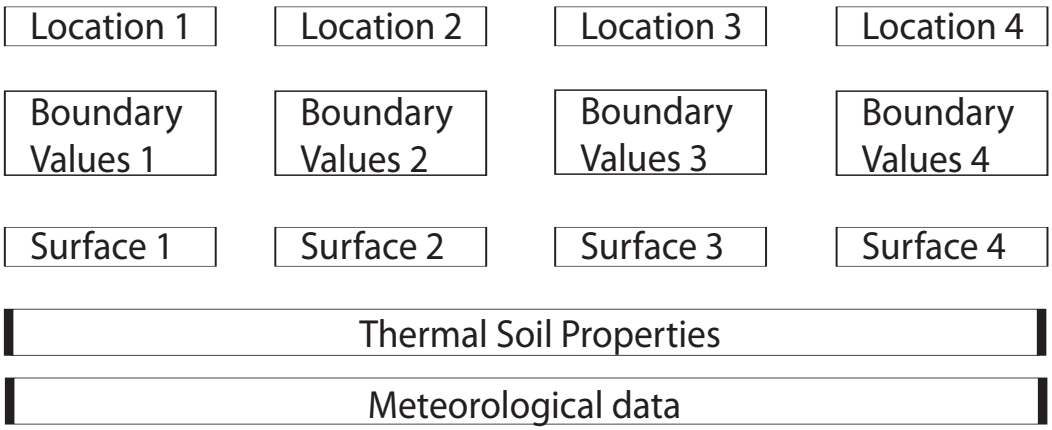

Figure 3.9: Principles of the data input in the soil model by Van Der Molen et al. (2008). - The input data consists of the homogeneous meteorological and soil data set and diverse boundary values and properties of the surface coverings.

3.6 Calibration of the Network Hydraulics

Simulation of temperature transport depends on reliability of a network hydraulic model. Errors in hydraulic model can greatly affect results of water quality simulations. Therefore, to limit prediction uncertainty, we have chosen to modify the Waternet default hydraulic model according to measured water flows.

Observed Water Demands

The area was divided into sections (see scheme of the division in Figure 3.10). Modifications related in great deal to changes in demands multiplier patterns and base demands (thereby flows). The demand patterns were altered at all group of model's nodes. The values of base demands and demand patterns corresponded with the values registered by water meters deployed at the selected housing connections. Those base demands were then extrapolated to the remaining houses at the section.

The water meters deployed at a number of representative households were continuously measuring the specific demands and weekly and daily patterns during the period from 15th of October 2009 till 6th of December 2009. To this end, Actaris Flodis residential single jet velocity, turbine type water meters were used. Technical details can be found in Appendix A.7. Table 3.5 and Figure 3.16 indicate location of the water meters installed and provide data on the number of inhabitants and prevailing type of housing at the measuring location.

Table 3.5: Deployment of Actaris Flodis water meters; respective information on water usage at a specific household type.

Denomination (section)	Number of inhabitants	Total number of tap points	Washing machine usage	Dish washer
B8 (C2)	1	9	night	Y
B1 (C1)	4	7	day	Y
B11 (C1)	2	7	day	Y
B3 (B6)	2	8	day	Y
B9 (A1)	3	9	evening	Y
B5 (B2)	2	8	day	N
B16 (B1)	4	8	day	Y
B12 (B3)	2	8	day	Y

The total incoming discharge was measured by the Waternet's flow meter located at the entrance of the section (see Figure 3.2). In next sections we will discuss how the observed flow measurements were implemented to Epanet 2; a demand-driven water distribution modelling software that uses temporal demand multipliers patterns to periodically vary demands. The Epanet 2 simulation results are reported in chapter 6.

3.6.1 Domestic Water Consumption According to Statictics

The division of west part of Diemen Noord site into sections was based on the site typology presented in Figure 3.4, the prevailing type of building and average number of house connections deducted from the occupancy rate.

Population Density

West part of Diemen Noord supply grid comprises a total of 324 household connections. There is one house per parcel and a pharmacy in the middle of the east part of the section. The number of inhabitants registered at Diemen municipality is 829 which accounts for 2.56 of the occupancy rate.

Population density can be estimated according to uniform occupancy rate and a maximum number of people living in each type of the house (see Figures 3.3 and 3.10). The thus estimated population density, number of house connections multiplied by the occupancy rate, in each network section is given in Table 3.6.

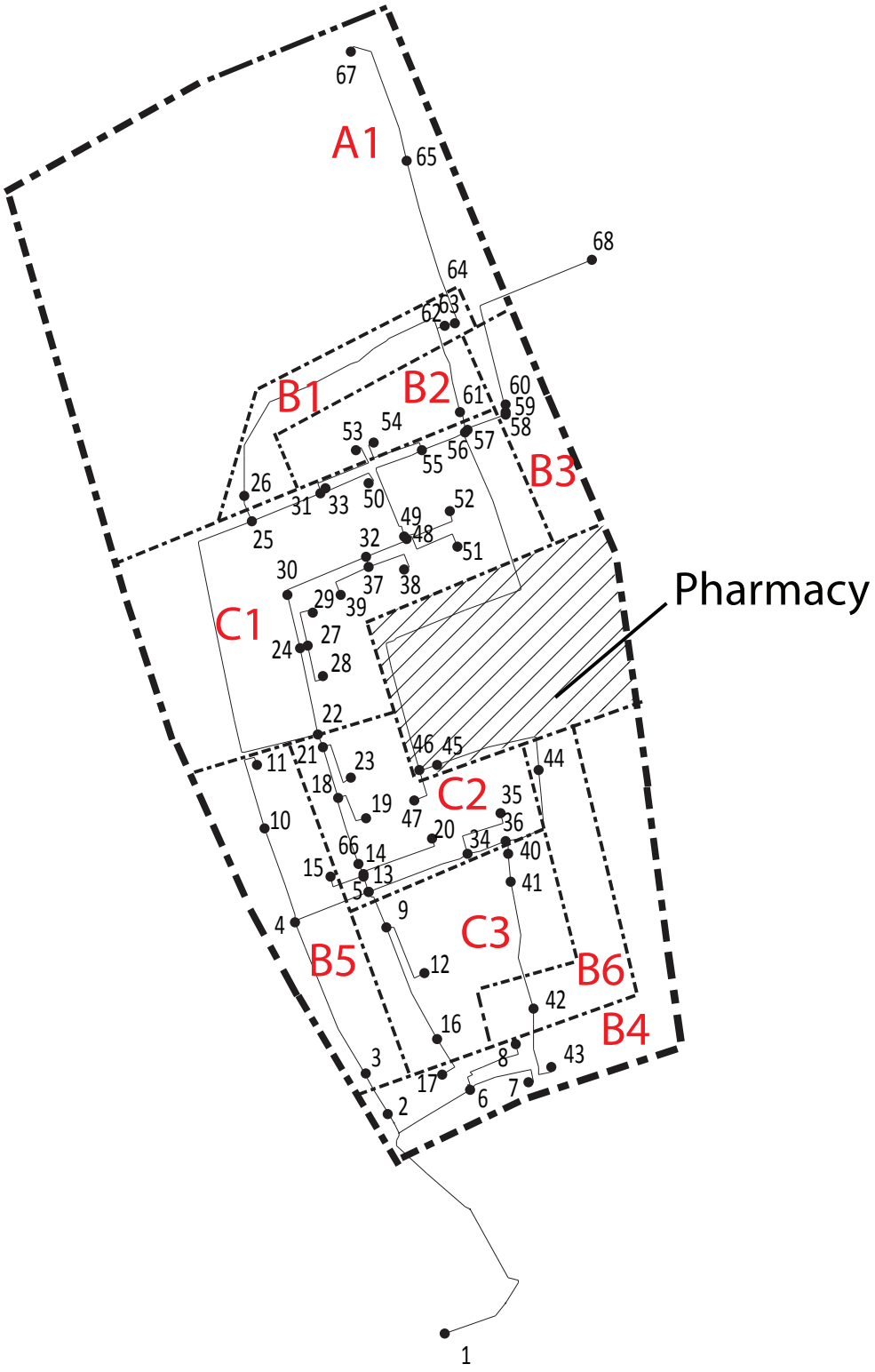

Figure 3.10: The sectional division of the west part of Diemen Noord supply grid. - Pipe routes and nodes are obtained from the Waternet SynerGee hydraulic model, which has been exported to Epanet 2.

Water Consumption

Uniform occupancy rate allowed projection of water demands at each section[1]. Table 3.6 presents demands allocation per section. The demands are assumed to be equally allocated over a section. Industrial water consumption at the pharmacy is unknown and is to be measured.

Table 3.6: Estimated population density and domestic water demand at west part of Diemen Noord according to the occupancy rate, the type of building and estimated number of people per section.

section	Number of connections	Number of nodes	Type of the housing	[cap]	Basic consumption per house [l/day]	Basic consumption per section [l/day]	Sectional average consumption [m3/d]
A1	5	3	detached	12.5	150	1875	1.9
B1	20	2	semi-detached	50	600	7500	7.5
B2	20	3	semi-detached	50	300	7500	7.5
B3	14	3	semi-detached	35	300	5250	5
B4	20	6	semi-detached	50	150	7500	7.5
B5	20	5	semi-detached	50	300	7500	7.5
B6	22	2	semi-detached	55	600	8250	8
C1	96	21	terraced	240	300	36000	36
C2	62	13	terraced	155	387	23250	23
C3	44	5	terraced	130	600	19500	20
D	1	2	industrial	2.5	0	375	
	Σ 324	Σ 65		Σ 829	$\bar{x} = 335$	Σ 124500	Σ 124

The total average consumption in west part of Diemen Noord is $124,34\mathrm{m}^3$/day which, according to statistics, yields a peak discharge [2] of $5,18\mathrm{m}^3/\mathrm{h}$. From the historical data on Amsterdam's drinking water demands, it can be found out that the average peak factor is on the average 2,18. According to this information, due to the domestic consumption of west part of Diemen Noord inhabitants the peak discharge of $11,3\mathrm{m}^3/\mathrm{h}^3$ can be expected.

3.6.2 Measured Domestic Water Consumption

The measured base demands are much higher as compared to what could be expected from the estimations based on a statistical analysis (see measured-estimated difference in Table 3.6). Table 3.7 presents demands allocation per section. In section D main demand pattern comes from the pharmacy.

The real sectional consumption was estimated from the base consumption registered at the typical housing in a section. The total sectional consumption was then proportionally allotted to the remaining

[1] The assumed domestic water consumption is 150 litre per capita.
[2] The peak discharge of 1. ($124\ 34\mathrm{m}^3$/day/24hr)
[3] When a peak factor of 2.18 is applied.

houses in a section according to the pipe length connected to a specific house divided by the total pipe length in a section.

Table 3.7: Measured domestic water demand at west part of Diemen Noord according to the readings from the domestic water meters deployed in each section.

section	Measured consumption per house [l/day]	Measured consumption per section [l/day]	Sectional average consumption [m3/day]	Measured-estimated difference (Table 4.5)
A1	233	1167	1.17	-0.71
B1	1035	20698	20.70	13.20
B2	336	6716	6.72	-0.78
B3	252	3528	3.53	-1.72
B4	295	5909	5.91	-1.59
B5	336	6716	6.72	-0.78
B6	336	7387	7.39	-0.86
C1	683	65572	65.57	29.57
C2	179	11089	11.09	-12.16
C3	192	9964	9.96	-9.54
D	490	490	0.49	
	$\bar{x} = 396$	Σ 139235	Σ 139.24	Σ 14.6

Demand Patterns

The demand patterns vary according to a housing type and maximum number of occupants in a house. Figure 3.11 gives a typical diurnal patterns at selected houses in sections B1, C1 and D (see Table 3.7).

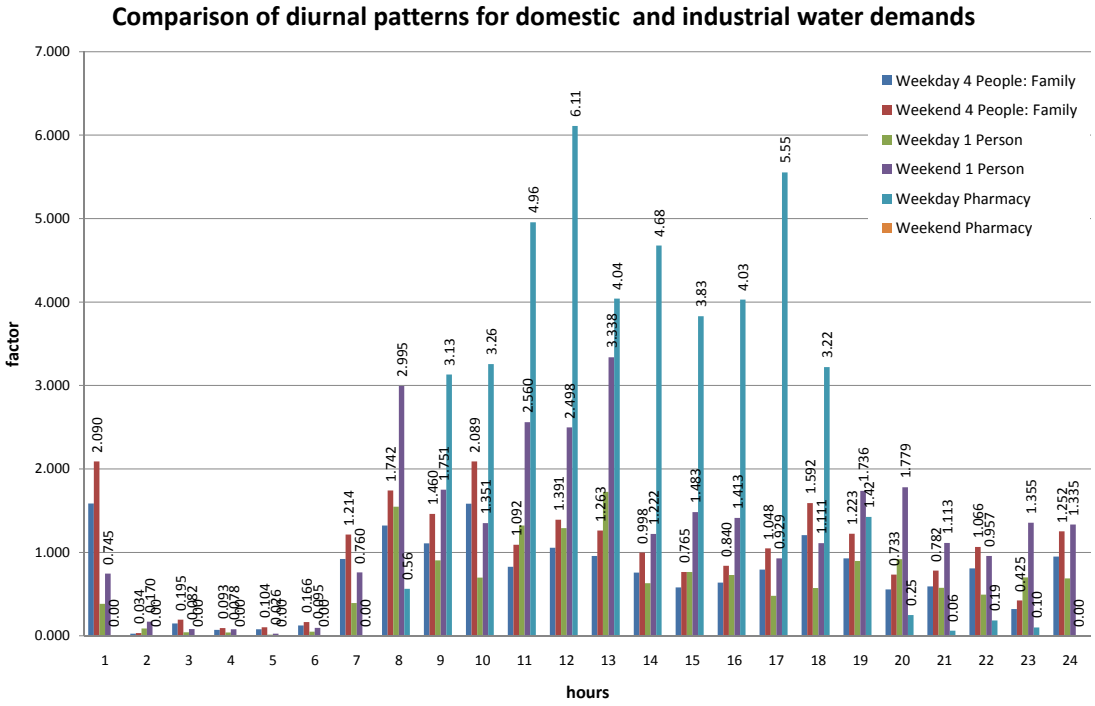

Figure 3.11: Diurnal pattern of domestic and industrial drinking water demand at characteristic housing in west part of Diemen Noord . - The peak factors are given for the 2 characteristic basic demand and for the industrial water consumption.

The week and daily demands have been calculated for each node according to variable pattern and the formulae for the required water supply to cover domestic (Equation 3.1) and industrial (Equation 3.2) demand (per hour) (Bollrich, 2000)

$$Q_{sup,dom(m)} = \frac{1}{1000} \cdot \frac{1}{24} \cdot q_{av,dom(m)} \cdot (1 - UFW) \cdot f_{d,dom(m)} \cdot f_{w,dom(m)} \tag{3.1}$$

$$Q_{sup,ind} = \frac{1}{1000} \cdot \frac{1}{24} q_{ind,av} \cdot (1 - UFW) \cdot f_{d,ind} \cdot f_{w,ind} \tag{3.2}$$

where Q_{sup} is required supply to cover domestic (dom) and industrial (ind) demands, m^3/h, m=1...n is a node number and n is a total number of nodes in a model, q_{av} is the average base domestic water

consumption (column one in Table 3.7), [l/day], UFW is unaccounted for water (leakage)[1], and f are the diurnal and weekly average peak factors for nodal domestic and industrial demands, respectively.

The total discharge per hour is then:

$$Q_{tot(n)} = \sum_{m=1}^{n} Q_{sup,dom(m)} + Q_{sup,ind} \tag{3.3}$$

Water Balance

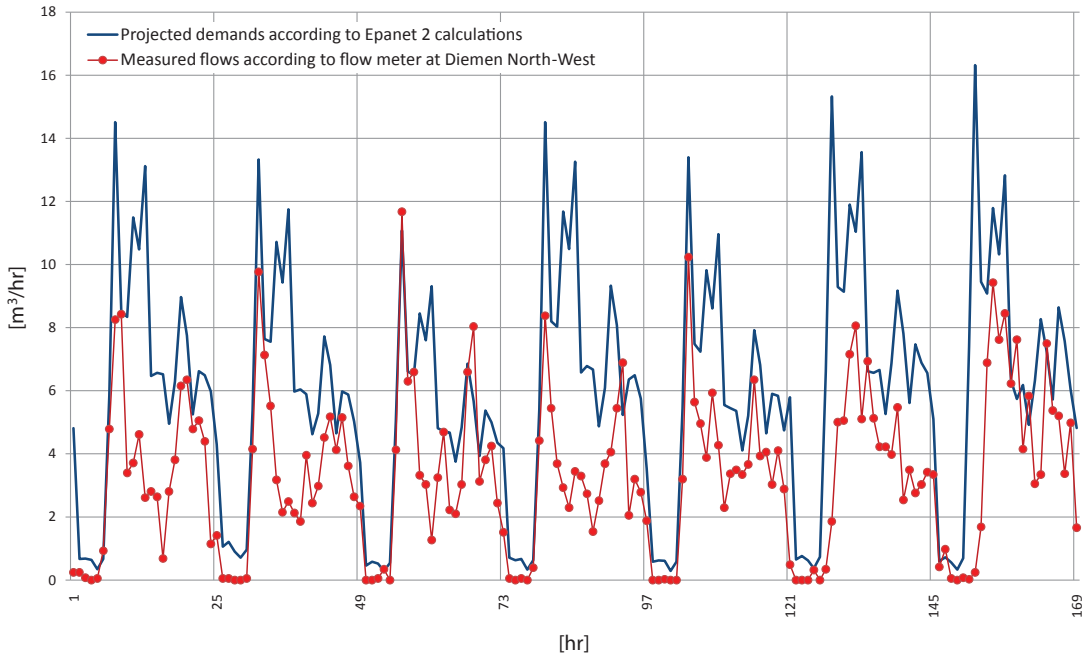

Figure 3.12: Measured water demand due to inhabitants of west part of Diemen Noord vs. calculated demand in Epanet. - The model overestimates the required demands by $2,26\mathrm{m}^3$/h. Based on Waternet hydraulic model.

The total model nodal consumption at one hour should not exceed the incoming discharge measured by the flow meter at the entrance of the area. Based on the average nodal consumption presented in Table 3.7 and realistic demands patterns, the new hydraulic model was applied in Epanet 2. The results were compared with the flow measured during the course of the measuring campaign. There was one week where the projected flows correlated well with the flow measurements registered by the flow meter (RMSE= $2,26\mathrm{m}^3$/h) (see Figure 3.12).

[1] Equals zero according to Figure 3.12, as the discharge is zero during night.

According to a preliminary test, the projected peaks differed decisively from measured peaks (and from $11,3\mathrm{m}^3/\mathrm{h}$ estimated by the statistics). The total incoming flow, measured at the start of the section, was less than anticipated by the model (see Figure 3.12). Only model demands between 48 and 72 hour (see Figure 3.13) were represented correctly. This pattern , from 48-72 hours, was taken as a base for further quality calculations and to this end was repeatedly applied to week 48 (15/11/09-22/11/09) where it fitted well with the flow meter values resulting in the total root mean square error of $1,3\mathrm{m}^3/\mathrm{h}$.

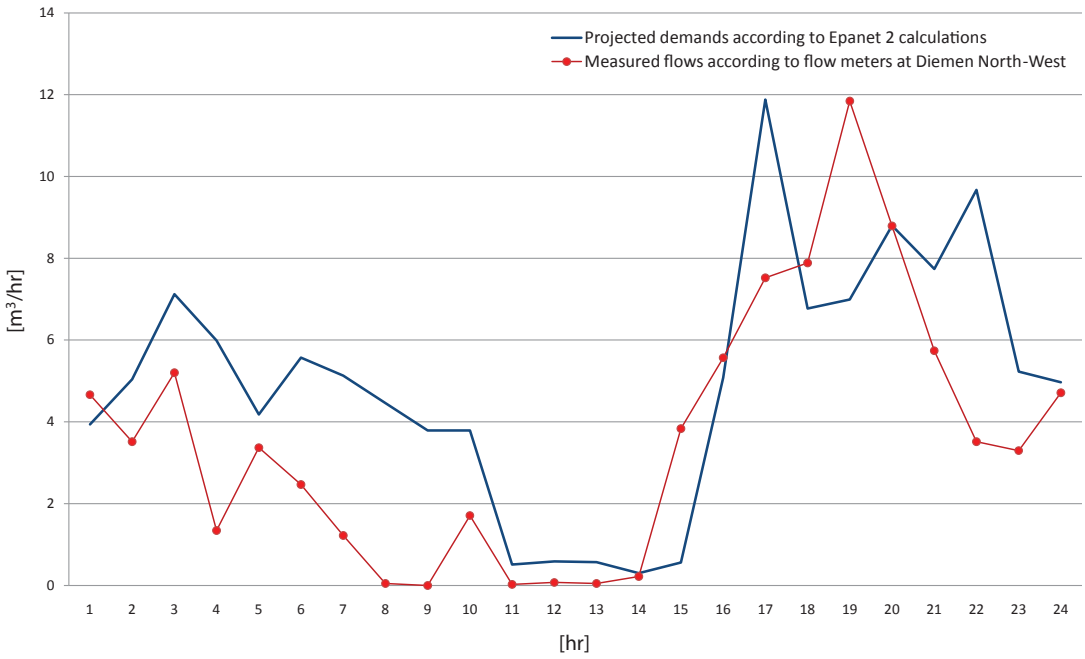

Figure 3.13: Selected water demand pattern vs. measurements. - The final root mean square error due to hydraulic model is $1,3\mathrm{m}^3/\mathrm{h}$. Based on Waternet hydraulic model.

3.7 Validation of Temperatures in a Network

Epanet MSX

To calculate the temperature in the west part of Diemen Noord distribution system, Equation 2.55 was extended with the Epanet 2 with an multi-species extension (MSX)[1]. The quality model in Epanet MSX track changes of discrete parcels of water as they travel through the network, according to Lagrangian transport algorithm. This algorithm ignores axial dispersion and tracks the movement and reaction of chemicals in discrete water volumes, or segments. The water 'volumes' travel by the bulk mean velocity and mix completely at junction nodes (see Figure A.27).

Epanet MSX extension allows to model a mobile bulk water phase and a fixed pipe surface phase. Bulk temperature species are dependent on the incoming (source) bulk water phase. Surface phase is a temperature that is incorporated into the pipe wall and are thus rendered immobile. Such a surface phase is a temperature absorbed at laminar layer of water, which is either equal the soil temperature (according to (Blokker and Pieterse-Quirijns, 2009)), outside pipe wall temperature (according to section 2.5.4 in chapter 2).

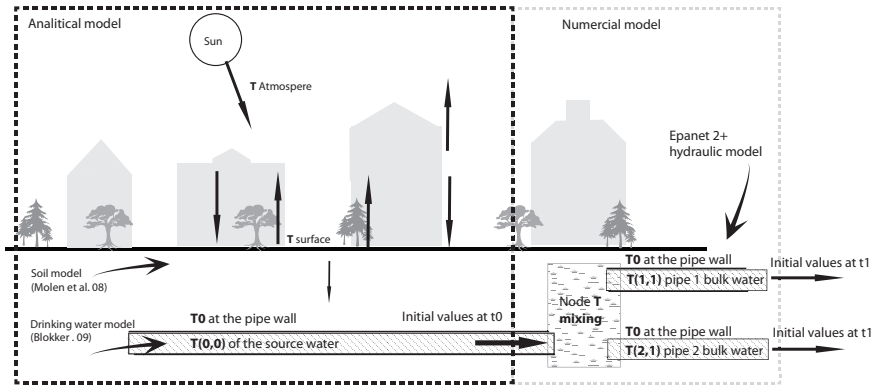

Figure 3.14: Schematic representation coupling of the hydraulic and heat transfer models. - The conceptual representation of a possible models' coupling. The abbreviation 'T' is a temperature. T0 means an initial temperature (at time an first time step t0), T1 the temperature after one time step (t1).

In Epanet MSX the heat transfer reactions can be modelled with an ordinary differential equations applied at specific pipes and nodes in a network. The heat transfer parameters, similar to the one presented in equation 2.56 for exit water in a pipe, can be applied to all pipes. The pipes will have different conduction coefficients which will allow required diversification. The heat and mass transfer coefficient will in general depend on the amount of flow turbulence, type and diameter of a pipe as well

[1]The code is given in Appendix A.12

as initial temperature values. A typical empirical relation might be the one developed by Blokker and Pieterse-Quirijns (2009), which is based on the mean bulk water temperature (see equation 2.56). The code used in Epanet simulations is given in Appendix A.12.

Validation

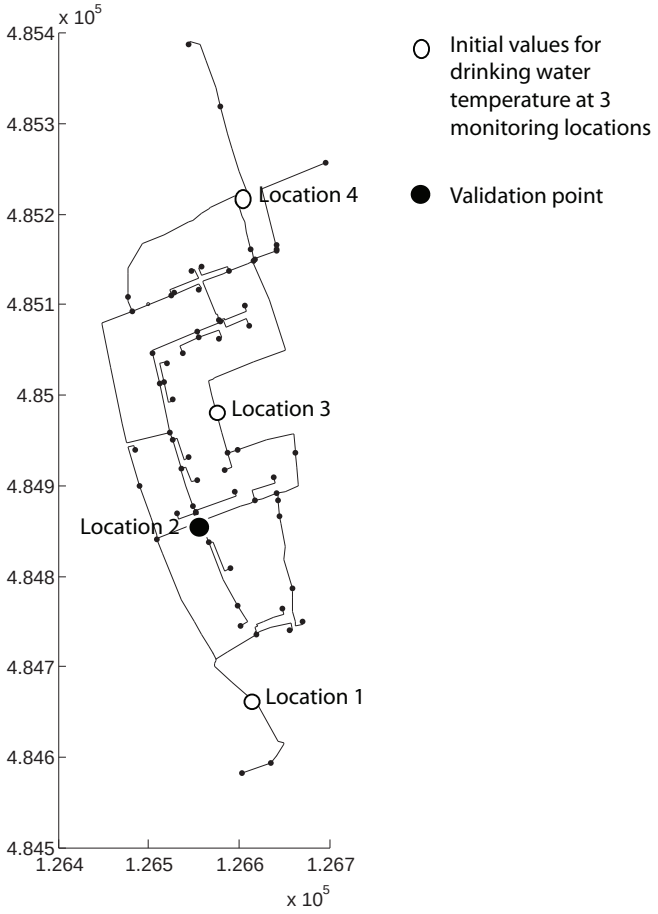

Figure 3.15: Network validation procedure at west part of Diemen Noord. - Location of the temperature inputs and a validation point that has been used to verify network simulations.

Sampling locations 1, 3 and 4 are used as sources of temperature in the network. Specifically, the initial temperatures are applied at nodes 1, 3 and 4 at time zero. At every subsequent time this initial value is multiplied by the specific temperature pattern created from the real drinking water temperature measure-

ments. At the remaining nodes temperatures at each unit of time are added to the total flow entering the specific node from all connecting pipes. More detailed description of Epanet MSX modelling principles can be found in (Rossman, 2000).

In addition, the pipe wall temperature equals the average of the measured pipe wall temperatures from the four sampling locations (see position of sensor 2 at four locations in Figure 3.7). This value is kept almost constant at the simulation interval(see MSX code in Appendix A.12 for details, the value is slightly regressing in time).

In order to compare results from the network modelling location 2 was chosen as a verification point, were the modelling results will be verified with measurements. Only pipe wall and bulk species were applied at location 2. No initial values neither temperature patterns are applied at this node.

3.8 Experimental Summary

The NTC sensors and loggers were installed on 15th of October 2009 and the measuring campaign for the purpose of this thesis ended on 6th of December 2009 but the NTC thermistors and Mini Divers are on site measuring till October 2010.

During the eight weeks the valve, indicated in Figure 3.2, were closed, so that the demands were solely due to inhabitants of the west section of west part of Diemen Noord and the incoming flow could be measured over a single in-fluent pipe.

By the 15th of October 2009, all the NTC soil and pipe temperature sensors were installed at the selected locations. Subsequently, one week later eight water meters were deployed at various houses in west part of Diemen Noord. In the beginning of November, the groundwater Mini-Divers were located in the piezometers adjacent to the measuring points. The individual sampling rates and manufacturing accuracies are given in the Table 3.8.

Table 3.8: Summary of the sampling rate and accuracies of the used instrumentation

	Accuracy	Sampling rate
NTC 100k Ohm	± 0 2°C	10 min
Mini-Diver		30 min
Actaris	$\pm 5\%$	1 min

Table 3.9 gives details on NTC thermistors and Mini Divers setting. Figure 3.16 provides a detailed map indicating the divers, NTC thermistors and water meters sampling locations deployed at west part of Diemen Noord. The groundwater temperature was measured with Mini-Divers placed in the existing piezometers, which are situated in the vicinity of the monitoring points.

Table 3.9: Period of measurements and arrangement of the NTC thermistors and Mini-Diver instrumentation

Address	Sensor	Instrument	Denom.	Position	Depth	Temperature /parameter measured
Buitenweg 2	location 1				[m]	
	1	NTC 100k Ohm	S11	inside the pipe	-1.13	water
	2	NTC 100k Ohm	S21	at the pipe wall	-1	PVC pipe wall
	3	NTC 100k Ohm	S31	in the soil	-1	resistance
	4	NTC 100k Ohm	S41	in the soil	-0.5	soil
	5	NTC 100k Ohm	S51	at the surface	-0.1	surface
Oude Waelweg 6	location 2					
	1	NTC 100k Ohm	S12	inside the pipe	-1.08	water
	2	NTC 100k Ohm	S22	at the pipe wall	-0.95	CI pipe wall
	3	NTC 100k Ohm	S32	in the soil	-0.95	resistance
	4	NTC 100k Ohm	S42	in the soil	-0.5	soil
	5	NTC 100k Ohm	S52	at the surface	-0.1	surface
Houtbosch 39	location 3					
	1	NTC 100k Ohm	S13	inside the pipe	-1.61	water
	2	NTC 100k Ohm	S23	at the pipe wall	-1.02	PVC pipe wall
	3	NTC 100k Ohm	S33	in the soil	-1.1	resistance
	4	NTC 100k Ohm	S43	in the soil	-0.5	soil
	5	NTC 100k Ohm	S53	at the surface	-0.1	surface
Vierhuizen 39	location 4					
	1	NTC 100k Ohm	S14	inside the pipe	-1	water
	2	NTC 100k Ohm	S24	under the pipe	-0.9	CI pipe wall
	3	NTC 100k Ohm	S34	at the pipe wall	-0.7	groundwater
	4	NTC 100k Ohm	S44	in the soil	-0.3	soil
	5	NTC 100k Ohm	S54	at the surface	-0.32	concrete
Steenen Kamer 2	1	Mini-Diver	G1	piezometer	-1.15	groundwater
Oude Waelweg 19	2	Mini-Diver	G2	piezometer	-1.18	groundwater
Houtbosch 55	3	Mini-Diver	G3	piezometer	-1.25	groundwater
Vierhuizen 39	4	Mini-Diver	G4	piezometer	-0.96	groundwater
Hofstedenweg 74	5	Mini-Diver	G5	piezometer	-1.9	groundwater
Gravelaan 49	6	Mini-Diver	G6	toilet basin	-	tap water
Gravelaan 51	7	Mini-Diver	G7	piezometer	-1.65	groundwater
Oudiedimerlaan 108	8	Mini-Diver	G8	piezometer	-1.85	groundwater

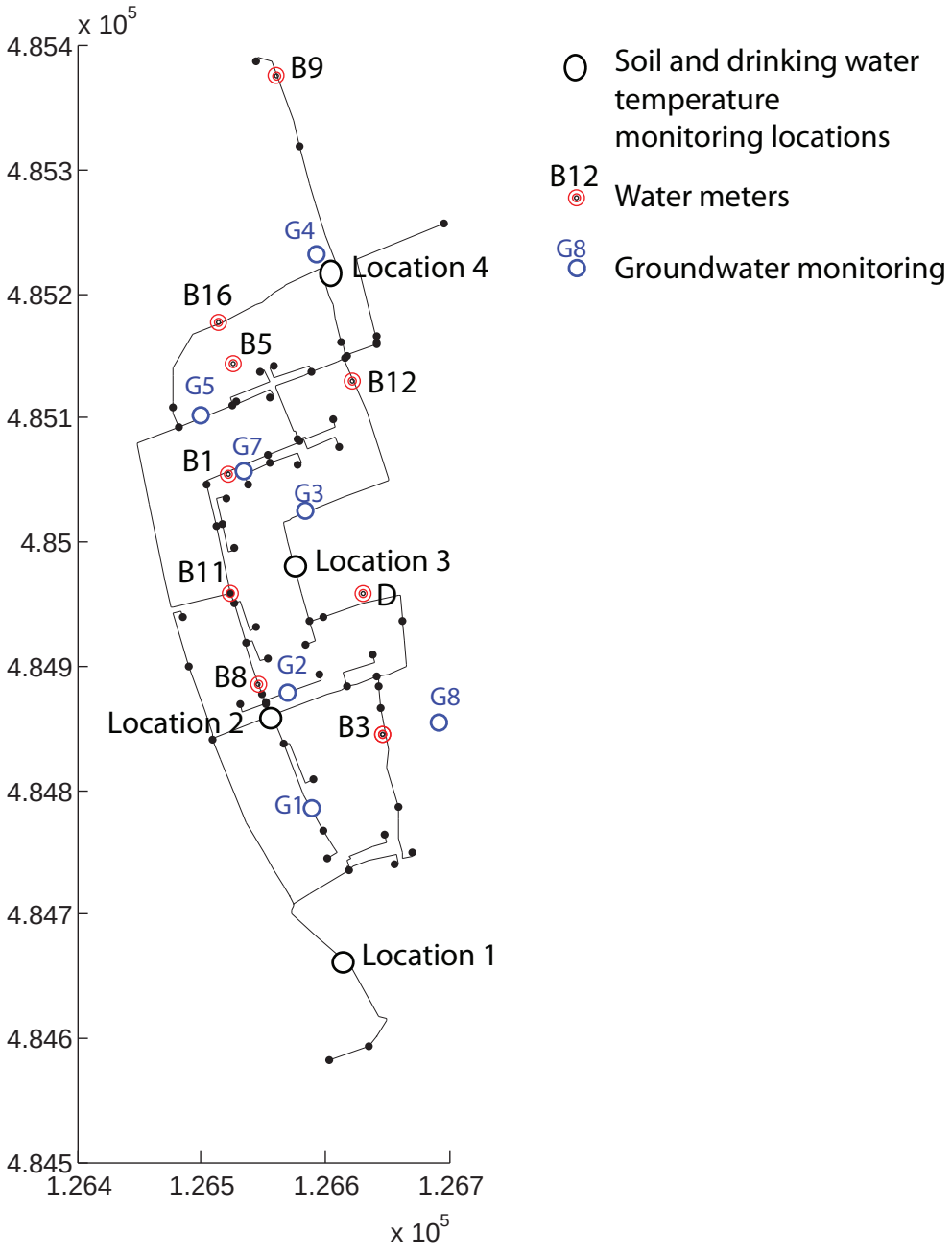

Figure 3.16: Deployment of the various instrumentation at west part of Diemen Noord. - Position of the NTC, divers and water meters in a RD coordinate system[1].

4

Measurements Analysis

4.1 Introduction

In the introductory chapter we have presented a selection of statements derived from previous findings, namely: (i) drinking water relates to the outside temperature, (ii) drinking water heating time depends on the pipe fabric, (iii) soil temperature at the pipe depth differs significantly at different coverings, (iv) soil determines drinking water temperature, (v) soil layer constitutes the largest thermal resistance to the heat transfer from the air. We have based our analysis of experimental observations on comparing and contrasting measured results with what could have been inferred from heat transfer models (sensitivity analysis) in order to support or refute those five claims. In general, this analysis is closely entwined with the model validation in the next chapter; it analyses how realistic model projections are.

The chapter begins with an analysis of heating time entailing to a drinking water distribution network. A comparison of temperatures registered at the extraction point in Weesperkarspel and at four monitoring points of west part of Diemen Noord, to verify differences between the observed heating time and the heating time predicted by the drinking water model, is given in a subsequent paragraphs. In section 4.3, relations between the atmospheric conditions and drinking water temperature are discussed. In section 4.4 we review temperatures of air, soil, pipe wall and drinking water and again compare them with the sensitivity analysis of the soil temperature models. The temporal variability of the soil's temperature is verified by a frequency spectrum analysis. The results are reported in section 4.5.

It should be noted that the NTC time series obtained from the short measuring period of 15th of October 2009 - 6th of December 2009 were inconclusive. Since this thesis has been extended for a longer period, an extended time series are thus used as they reflect better seasonal changes. Especially,

the drinking water time series are discussed for the period of 9th of November 2009 - 23rd of April 2010 (Period A). The focus is however narrowed down to the measuring period of 9th of November 2009 - 6th of December 2009 for which groundwater temperature series and the flow measurements are available (Period B).

4.2 Drinking Water Heating Time

It is possible to estimate density of the heat flux and its influence on the open water (extraction point) and a soil column (distribution) based on the wavelengths and spectral emissive power of the net radiation (see Appendix A.2). The short wave radiation is between two boundary values of 160-220W/m^2; long wave 200-400W/m^2 and back radiation between 400-460W/m^2. It can take more than one day [1] (1.8 days) to heat up by $1°\mathrm{C}$ a water column (for example at an extraction point[2]), whereas it takes a bit more than a half of a day (0.8 days) for the soil column of $2\mathrm{m}^3$ to be heated up by $1°\mathrm{C}$. Therefore, by the time the temperature at the extraction point will be influenced by the heat wave, the soil temperature,and perhaps distribution pipes, will be already affected by the atmospheric conditions.

Heating Time According to Drinking Water Model

According to sensitivity analysis of the model developed by Blokker and Pieterse-Quirijns (2009) long and small diameter cast iron pipes have a short characteristic heating time which is usually much shorter than the average network hydraulic residence time.

In PVC pipes heat conduction from ambient soil is limited due to big thermal resistance of the PVC material. It takes a day or more for the exit water in a PVC pipe of $400\ \mathrm{mm}$ to heat up from $10\ °\mathrm{C}$ to the soil temperature of $25\ °\mathrm{C}$, assuming constant velocity of $0.1\ \mathrm{m/s}$. The cast iron pipe would need an hour to heat up in the same situation (see Figure 4.1). This is clearly explained by materials different thermal inertia; a typical cast iron will have a thermal inertia of $20.2\ \mathrm{J/m^2\ K\ s^{0.5}}$ while PVC $0.47\ \mathrm{J/m^2\ K\ s^{0.5}}$ (see Equation 2.19, chapter 2).

Transport pipes are usually long, cast iron pipes with big diameters (more than $300\ \mathrm{mm}$), which means the water transported from the source to the treatment plant will be already heated up to the ambient soil temperature. Distribution pipes made from cast iron and with diameters between 100-$250\mathrm{mm}$ will encounter a similar effect. The PVC distribution pipes will be cooled down by the bulk of

[1] A time required to heat 6 meter column of water of 1000kg/m^3 density and 4195J/kg/K with radiation of 160W/m^2.

[2] At Waternet extraction point at the lake Loenderveen is at the level of *metalimnion*, which is at $6\mathrm{m}$ depth, where anaerobic conditions, high algae content and increased concentration of the dissolved iron and manganese are negligible (see Appendix A.3).

[3] A time required to heat a column of 2 meter sand of 1900kg/m^3 density and 2650J/kg/K by $1°\mathrm{C}$ with radiation of 160W/m^2.

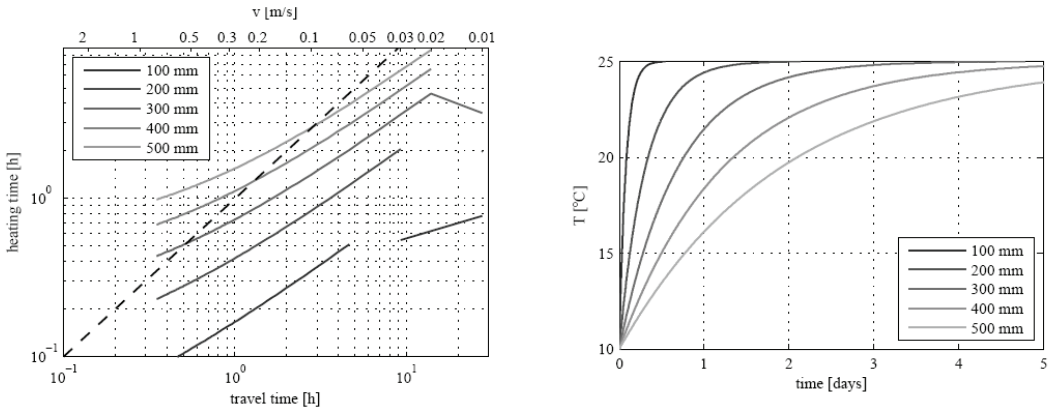

Figure 4.1: Sensitivity of the drinking water model to a changes in a pipe fabric and diameter. The entering water temperature is 10°C. The ambient soil temperature is 25°C. A sensitivity analysis for the cast iron pipes, on the right(the dotted line is travel time) and PVC on the left. The velocity is held constant $0.1\ \mathrm{m/s}$. Source: (Blokker and Pieterse-Quirijns, 2009).

water provided the temperature of the incoming water is lower than the ambient soil and the residence time does not exceed the required heating time, see figure 4.1. It takes 12 hours for 100 mm PVC pipes to heat up to the soil temperature, in theory.

Blokker and Pieterse-Quirijns (2009) assume a situation where the ambient soil is 15°C warmer than the water in pipes. Based on this assumption, Blokker and Pieterse-Quirijns (2009) go on with quantifying relation between the travel time, pipe type and time required to heat the piped water to the ambient soil temperature (see Figure 4.1). From the measurements we can see however that the temperature gradient between the temperatures of the ambient soil and the drinking water applied in the (Blokker and Pieterse-Quirijns, 2009) renders unrealistic at the conditions we have found at Diemen Noord.

Heating Time According to Measurements

Measurements collected during the Period B indicate that temperatures of the water registered at the extraction point in Loenderveen are around $1°\mathrm{C}$ lower than the temperatures registered at Weesperkarspel production site and 2-3°C lower than the temperatures at at sampling locations at west part of Diemen Noord. This discrepancy gets $2°\mathrm{C}$ or $1°\mathrm{C}$ bigger with time (see Figure 4.2). Furthermore, a daily fluctuation can be seen in the temperature patterns of the distribution pipes, an effect which can be attributed to heat fluxes from the ground water.

Residence Time at Production Site

The water travels around $10\mathrm{km}$ as it recedes from the extraction point to the production. The distance between the extraction point and west part of Diemen Noord is around $20\mathrm{km}$. The average water velocity is 0.1-0.2 $\mathrm{m/s}$[1]. Given such long distance, the drinking water should have three or four days to slowly adopt to the soil temperature. Figure 4.2 shows in fact that it takes around one week before the temperature in the distribution reaches the same temperature as at extraction point, which is probably an influence of the water residence time.

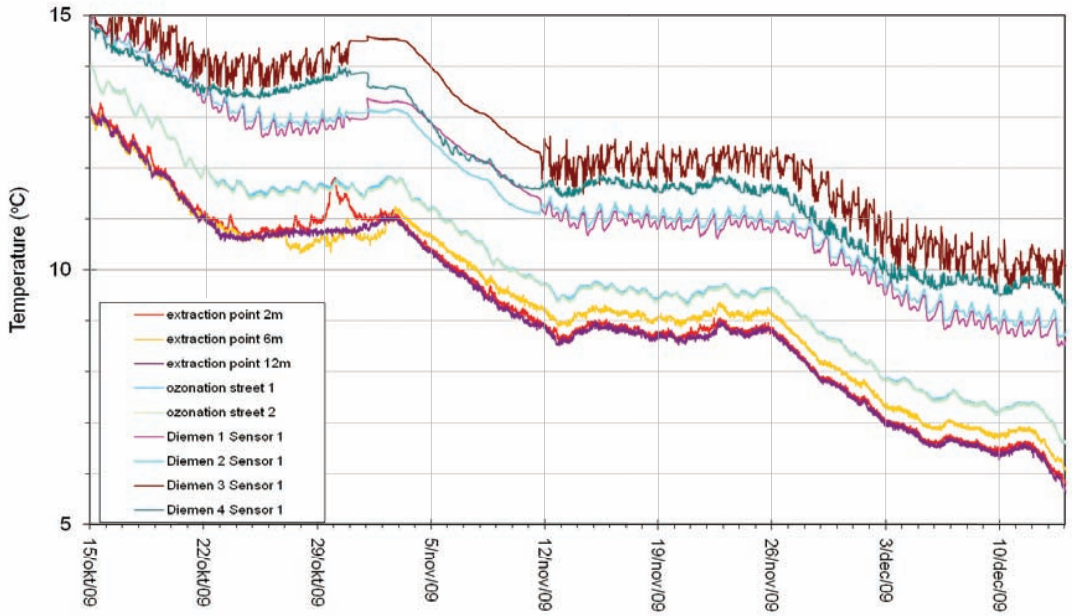

Figure 4.2: Drinking water temperature time series obtained from the extraction point, Loenderveen production site Wesperkarlsper and monitoring points at west part of Diemen Noord. - Temperature differences between the extraction point and drinking water measured inside the pipes at the 4 locations in Dimen North-West.

4.3 Influence of the Atmosphere

Soil Model Sensitivity to Atmospheric Parameters

according to the sensitivity analysis of the model developed by Van Der Molen et al. (2008) air temperature and global solar radiation play a crucial role in predicting the soil temperature (see Appendix A.9 and Table A.6). Values of net global radiation and air temperature registered at two distant synop-

[1] Information provided by Waternet.

tic stations (Bilt and Schiphol) showed a very good correlation (see Figure 6.3). Thus data from the closest synoptic station (Schiphol , KNMI 240), were used in this thesis (see section 7.2, chapter 7 for discussion).

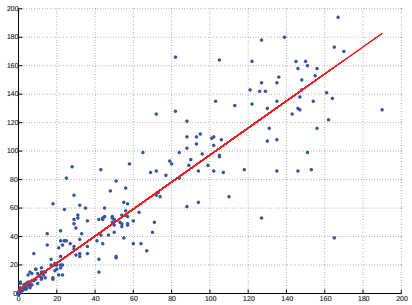

(a) Global radiation at Schiphol; KNMI 240 against Bilt; KNMI 260

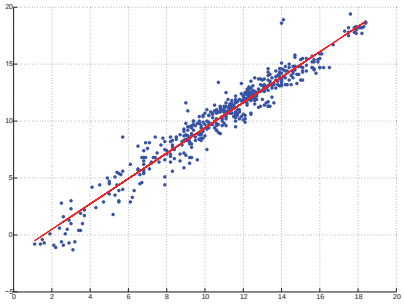

(b) Temperature at Schiphol; KNMI 240 against Bilt; KNMI 260

Figure 4.3: In the first graph: correlation of the measured global radiation, [$\mathrm{J/cm^2}$]; R^2=0.94, and the second: correlation of the temperatures, [$^\circ$C]; R^2=0.97. Both show a very good correlation ($R^2 = 0.95$)at the two distant synoptic stations.

Measured Soil Temperature and Atmospheric Parameters: Period A

Figure 4.4 presents meteorological data obtained from KNMI database[1] in the period A. As can be seen from Figure 4.4 and 4.6, the weather patterns are well reflected in the measurements of the soil temperature in west part of Diemen Noord, especially at the surface. When exploring the two figures, it can be seen how the increase in global solar radiation (from 01/03/10 onwards) results in the increase of temperatures at the surface (S5 at $10\mathrm{cm}$ depth).

Measured Soil Temperature and Atmospheric Parameters: Period B

Soil temperatures measured in the Period B are depicted in Figure 4.6. It can be seen clearly, that the soil temperature at at the $1\mathrm{m}$ depth follows weather changes. In the first week when the air temperatures were low, soil temperature plummeted. In the second week, the air temperatures soared, while the deep soil temperatures exhibited consistently lower through for almost two weeks. In the last measuring week the air temperatures fell again and so did the soil temperatures. The sharp rises and falls in the air temperatures are followed with a lag and attenuation by the deep soil temperatures.

[1] Source: KNMI, Royal Netherlands Meteorological Institute. Retrieved on 06.10.2009, from http://www.knmi.nl/kd/frequentietabellen/uur.cgi.

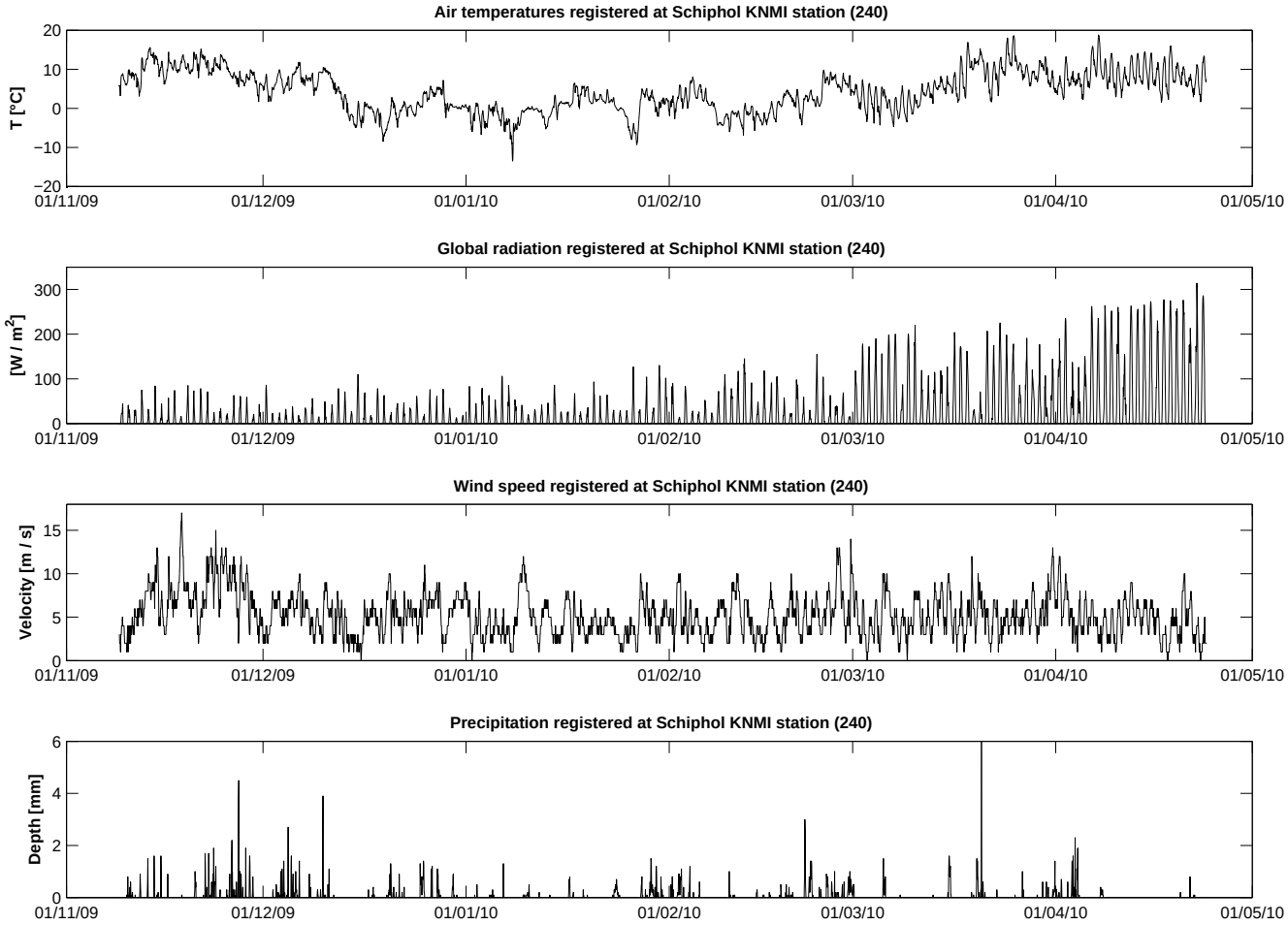

Figure 4.4: Overview of a meteorological data measured in the period of 9/11/2009-23/04/2010. 240 KNMI, Schiphol synoptic station.

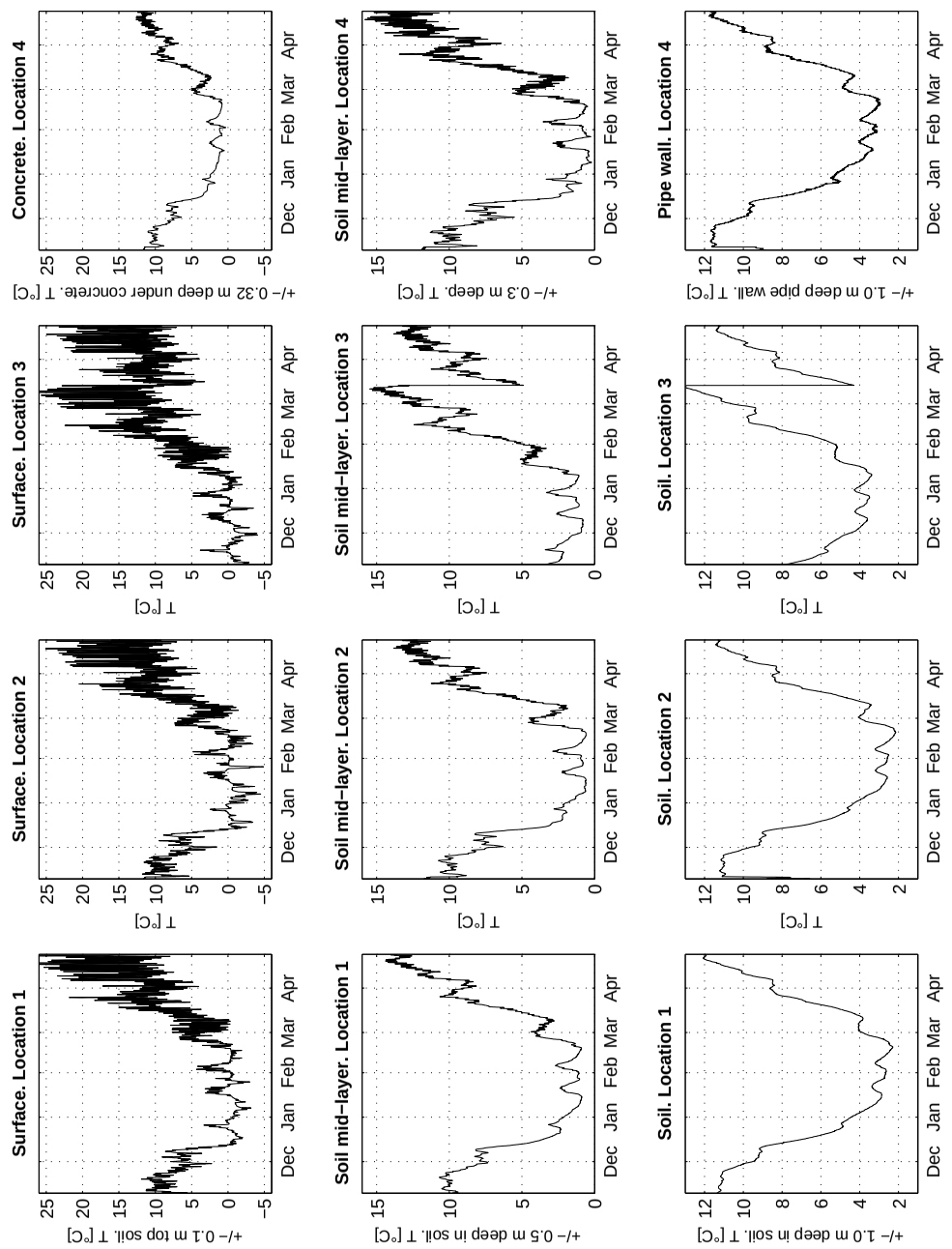

Figure 4.5: Comparison of the soil temperature measurements at different locations and different depths, in west part of Diemen Noord (Period A).

Figure 4.6 illustrates also differences in temperatures at different soil depths and at four different sampling locations. Discrepancies can be attributed to soil's changing thermal inertia according to the water content. Dry sand has thermal inertia $0.6\ \mathrm{J/m^2\ K\ s^{0.5}}$ while wet sand $2.78\ \mathrm{J/m^2\ K\ s^{0.5}}$.

At every depth big seasonal temperature changes and small diurnal temperature fluctuations, are clearly visible. The biggest amplitude of temperature oscillations are in time series of the surface temperature. Oscillations, which result probably from diurnal atmospheric changes, become smaller further in the soil depth. At the pipe burial depth (+/- $1\mathrm{m}$) only the strongest decreasing seasonal trend is visible.

4.4 Differences at Sampling Locations

Soil Model Sensitivity to Different Surface Coverings

Each sampling location features different albedo and covering (listed in Table 3.4[1]. According to soil model sensitivity analysis (see Appendix A.9; Table A.7 and first column second row in Figure 4.7), there should be at least $1^{\circ}\mathrm{C}$ difference between the soil temperatures at all individual locations. Location 4 should be the coldest spot[2]. This is not apparent in the results, therefore, model outcomes, cannot be confirmed with observations from west part of Diemen Noord.

Results depicted in Figure 4.9, show that at location 3 temperatures and amplitudes are higher from the remaining locations. Soil temperature differences cannot be explained purely by dissimilarities in the thermal properties of the coverings at individual locations (see Figure 4.7 and Table A.8; in Appendix A.9). The possible explanation for those discrepancies are micro-climatic influences at location 3.

Soil Model Sensitivity to Different Water Content

Typically soils enclosing the pipes consists of sand which can be occasionally filled with pockets of clay. Locations 1-3 are assumed to be filled with dry sand, while location 4 is moist sand. As have been explained in (Abu-Hamdeh, 2003) and chapter 2, soils' diffusivity depends on a water content. Soils have different properties when they are moist, saturated or dry. Therefore temperatures at locations 1-3 should be $1^{\circ}\mathrm{C}$ different at depths from temperature at location 4 (see moist sand in Figure 4.7 and Table A.8 in Appendix A.9). This is not visible in the measurements.

[1](location 1 thick concrete, 0.35; location 2 and 3 concrete, 0.11; location 4 both concrete, 0.11 and bare soil, 0.4)

[2]This location is not covered with impervious material and a latent heat flux can be there appreciated. So there will be cooling from the soil (due to lower temperatures) and cooling from the outgoing evaporation.

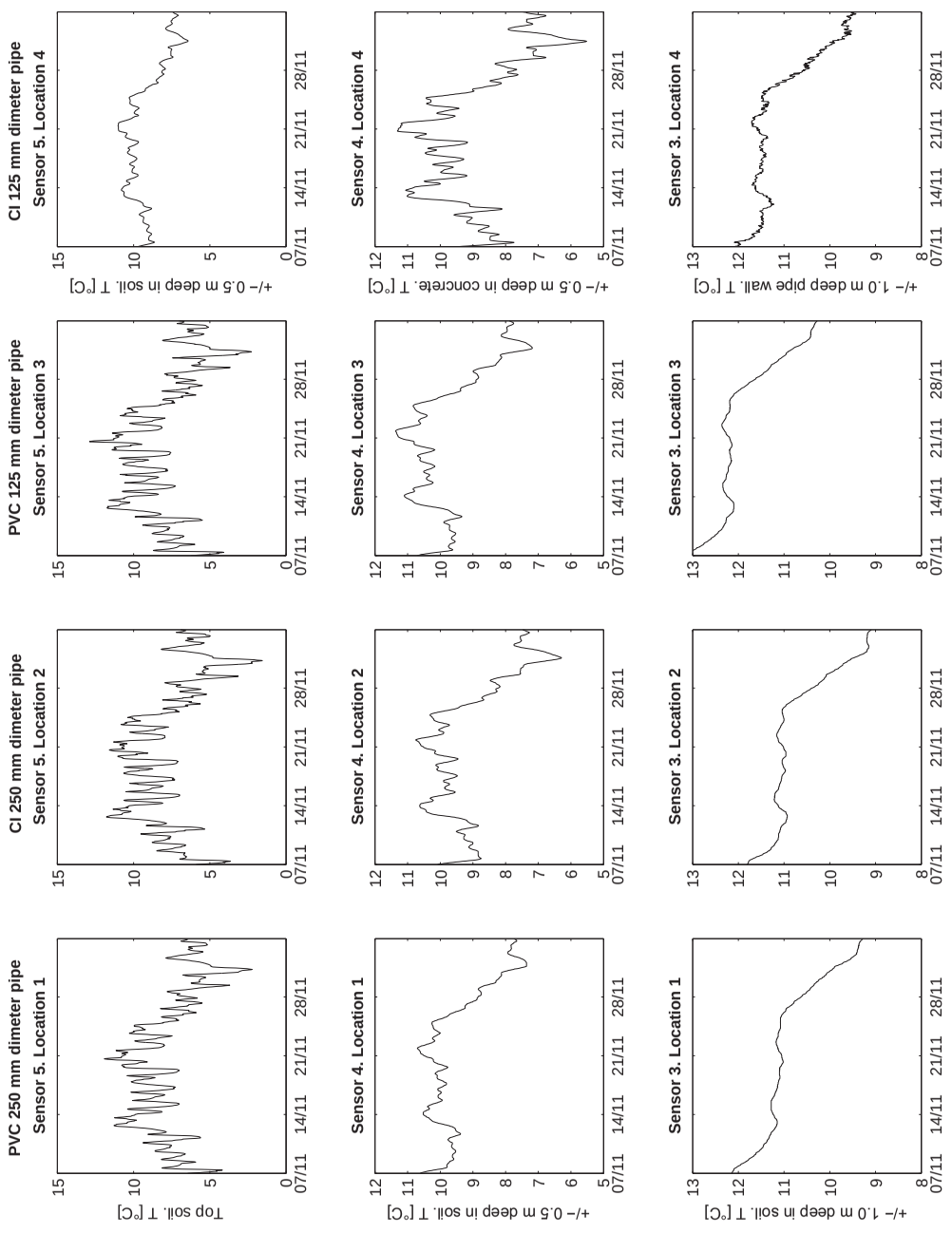

Figure 4.6: Comparison of the soil temperature measured at different locations and at different depths, in experimental set up at west part of Diemen Noord, in the Period B. Temperatures at all locations decrease linearly with time. Only the surface temperatures at S5 are not. Location 3 has the highest temperatures registered. Temperature time series at location 4 show a significant difference between the temperature under the concrete (S54) and under the bare soil (S44). Surprisingly, the temperature under concrete fluctuates more than the one under the bare soil.

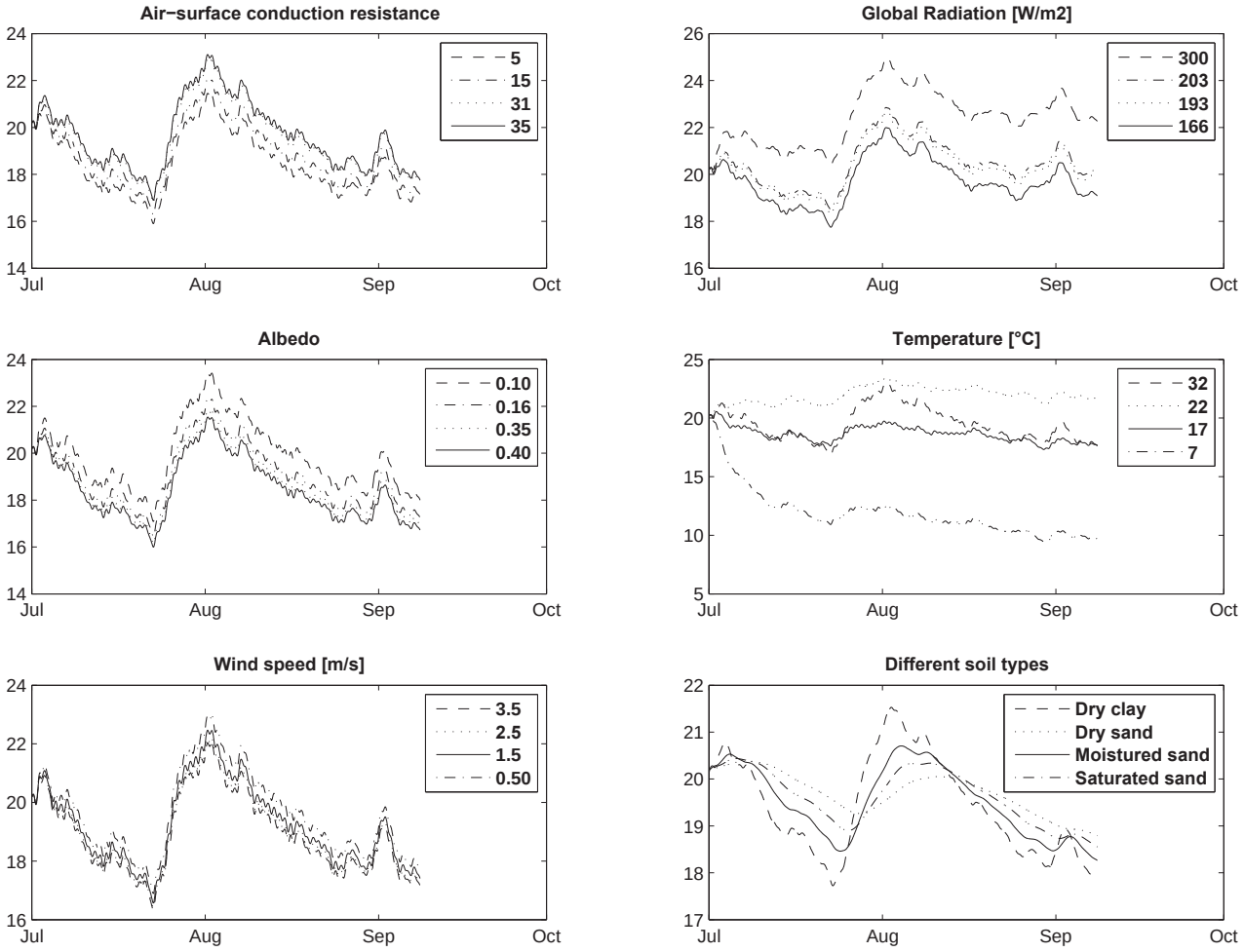

Figure 4.7: The anticipation of environmental influences on the soil model; results of the sensitivity analysis. RMSE is a root mean square error indicating the magnitude of the error as compared with the reference situation. N&S is a goodness of fit parameter indicating how well the curve obtained from the sensitivity run fit the reference situation.

Drinking Water Temperature at Different Locations

General patterns of drinking water temperature series are similar to the patterns visible in the soil temperatures (see Figure 4.8). They both reflect a seasonal trend. Pipe wall temperature at location 3, exhibit strange outliers[1]. Temperature and amplitude at this location are again the biggest. Whether those observations can be trusted is questionable. Pipe wall temperature at locations 1 and 2 are positively correlated.

Influence of Pipe Fabric on Drinking Water Temperature

According to assumptions described in section 2.6.1 of chapter 2 (see Figure 2.10 for temperature boundary conditions), it is expected that soil temperature is an upper boundary towards which the drinking water temperature eventually proceeds (see for verification Figure 4.9). But at all four locations, drinking water is fluctuating around the pipe wall temperature, at times it even exceeds pipe wall and soil temperature(see drinking water and pipe wall temperature patterns at location 3 Figure 4.9). It means that during the observations the heat flux was in the soil direction. Even if there were any heat fluxes from the drinking water, the volume of a pipe is much smaller than the volume of the soil enclosure, so any heat flux from the pipe would be quickly dampened by soil.

In general measured temperatures of the drinking water support results of the sensitivity analysis of the drinking water model. The pipe fabric influence water temperatures which at location 1 and 3, where PVC pipes are installed, are clearly less correlated with the pipe wall temperatures. The opposite applies at locations 2 and 4, with CI pipes. Temperature of the cast iron pipe at location 4 is constantly lower than the drinking water temperature. The reason for the lower temperature might be ground water influence but this can be also attributed to different thermal inertia of CI.

Influence of Groundwater on Drinking Water Temperature

According to Figure 4.10, the ground water at location 4 registered by NTC is $2^{\circ}\mathrm{C}$ lower than the drinking water which could explain the difference visible in Figure 4.9. However, the groundwater temperature registered by diver 4, which lays in a vicinity of location 4, is actually warmer than the drinking water. There is a $1^{\circ}\mathrm{C}$ difference between the temperatures registered by NTC (S24) and the Mini-Diver (G4) although both sensors are located in a proximity of one another. Perhaps, the gradient

[1] This data set has not been cleaned. This was intentionally to show that location 3 registered temperature values that may not be trusted. Data set for Period B was cleaned from outliers as this data set has been used for modelling.

Figure 4.8: Comparison of the soil, pipe and drinking water temperature measurements at each location at pipe depth (the period from 09/11/2009 to 09/05/2010). Temperatures at all locations follow a likewise pattern. Drinking water temperatures exhibit short wave oscillations which are partially reflected in the pipe wall temperatures, especially at CI pipe walls. At location 3 distinct equipment problems occurred which results in outliers starting visible from date 09/01/2010. Data obtained after that period should not be trusted.

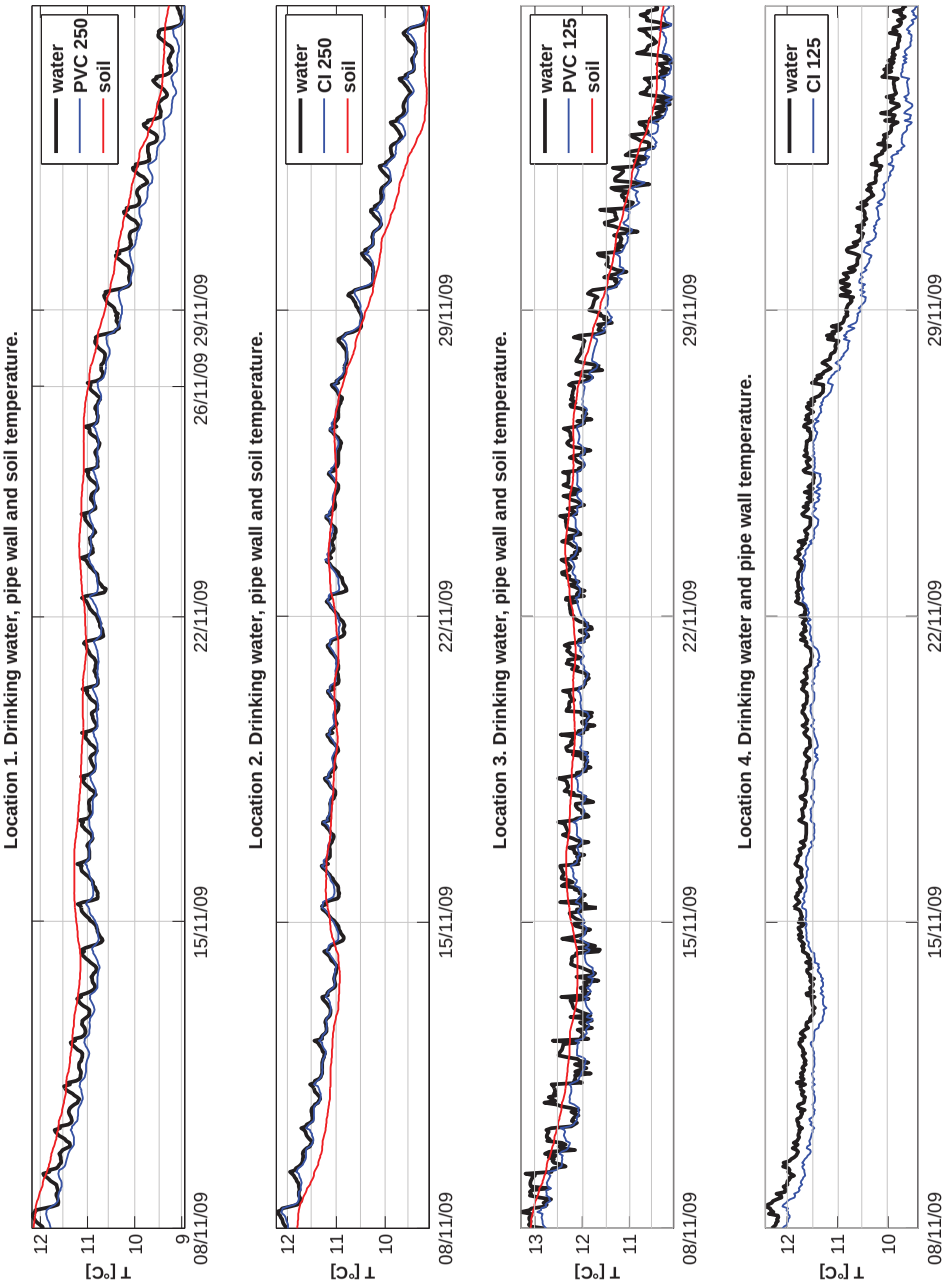

Figure 4.9: Drinking water and pipe wall temperatures registered by NTC thermistors during 8/11/2009-6/12/2009. Temperature time series of the soil, pipe wall and drinking water registered at all four monitoring locations at the same pipe depth.

results from differences in instruments' accuracies. Interestingly, the groundwater temperature near location 3–registered by Diver 3 (G3)–is approximately the same value as the drinking water temperature. At each measuring point (G1-G8) the groundwater temperatures are relatively constant.

Correlation Between Temperature at Pipe Walls

There is a high correlation between the temperatures registered at the interfaces of the pipe-soil-groundwater-drinking water. Table 4.1 list coefficients of determination. Values of all coefficients oscillate around $R^2 = 0.95$.

Table 4.1: Selected correlations at the interfaces and different mediae. Locations 1-4.

Independent v.↓	Soil (-1 m)	Pipe wall	Concrete	Groundwater	Drinking water
Soil (-1 m)	-	0.99	0.98	0.98	
Pipe wall		-			
Groundwater	0.98		-		0.94
Concrete (Location 4)				-	
Drinking water				0.94	-

In general, the most data points in correlation scatter plots (Appnedix A.11) are accumulated around 11-12°C but at some there is a displacement in the middle of scatter plots (see Figure 4.11). The reason for displacement can be a non–linear relation between correlated time series or a time difference between the temperature registered. Namely, the sampling frequencies of the two measurements were slightly different (10 and 30 minutes for NTC and Mini-Diver, respectively). However, for the purpose of a correlation check, the data has been interpolated to one hour values. One way to verify the source of the displacement would be a time-lag analysis.

Essentially, a correlation as good as in Table 4.1 may be misleading due to the fact that all the temperature time series contain the same long term seasonal trend. The presence of the trend gives impression that both the groundwater and soil temperature are good predictors of the drinking water temperature, when in fact one could explain more of the drinking water temperature variability than other.

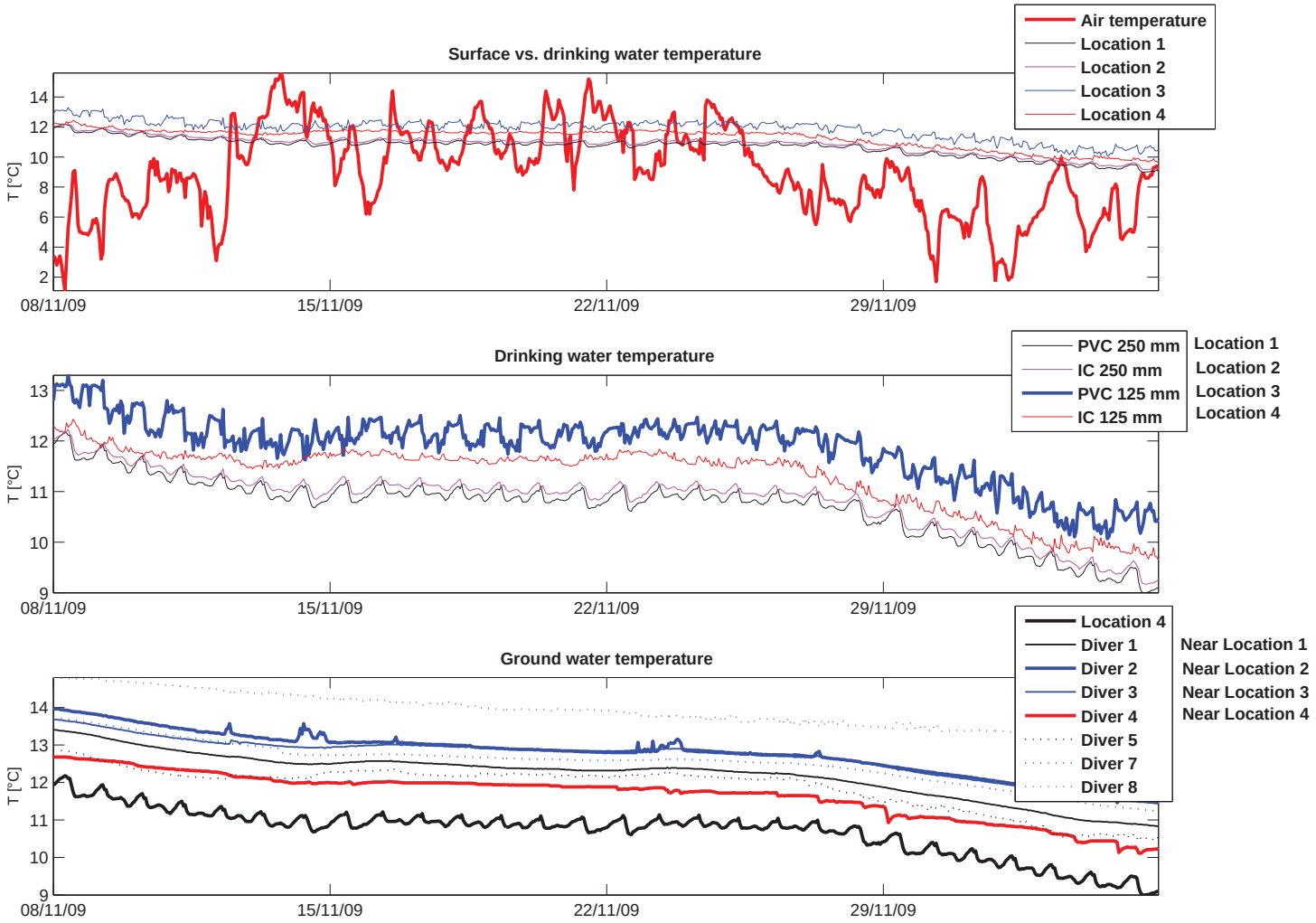

Figure 4.10: Comparison of the measurements in the period from 01/11/2009 to 06/12/2009. Drinking water temperatures at Locations 1 and 2, S11 and S12, are almost the same. There is no significant correlation between the air and the drinking water temperatures. At each measuring point (G1-G8) the groundwater temperatures have stable values.

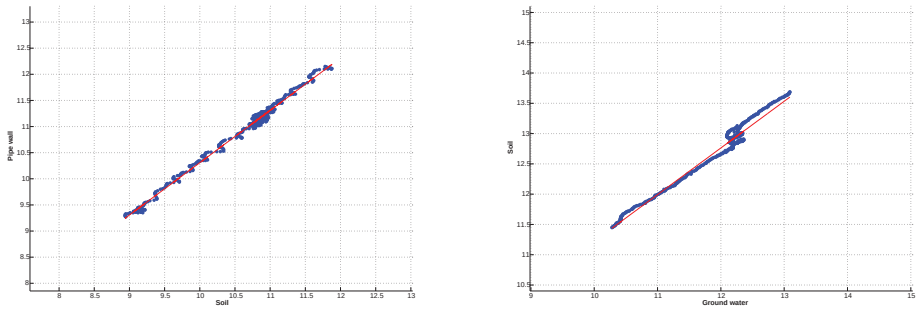

(a) Example of a scatter plot without displacement.

(b) Example of a scatter plot with a displacement.

Figure 4.11: Comparison of the scatter plots correlations of the temperature time series obtained at the interfaces of different mediae. Both scatter plots graphs represent a high coefficient of determination. First graph illustrates correlation of the temperatures $^{\circ}$C at the pipe wall and the soil at Point 1. R^2=0.98; second, correlation of the temperatures $^{\circ}$C of the soil and groundwater at Point 3. R^2=0.99. The second graph exhibit data points displacement in the middle of the graph.

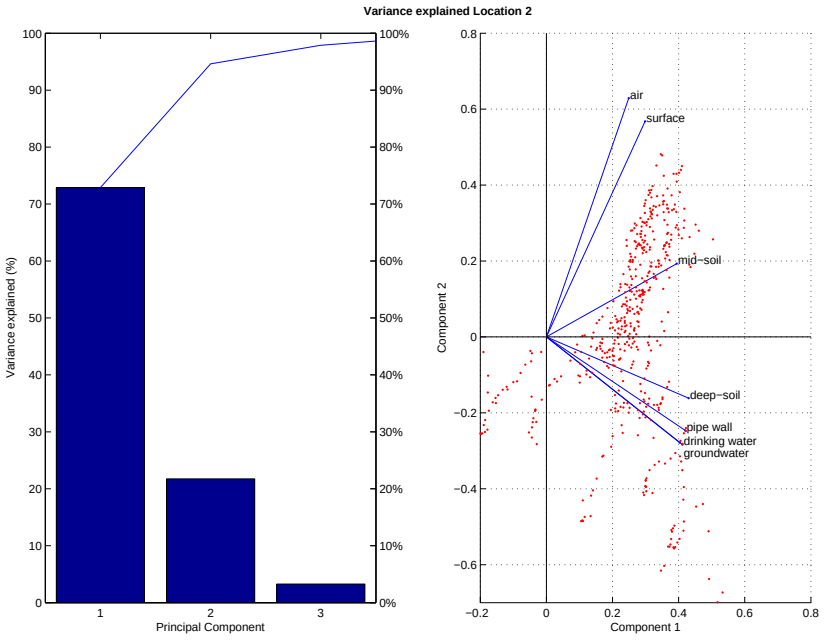

Figure 4.12: The Principle Component Analysis preformed on the data obtained from the measurements at the Location 2. - The principle component analysis distinguishes elements which accounts for the major system variability (see left figure). The different temperatures obtained from the sensors and groundwater divers are plotted in the right figure against two principal components.

From the principal component analysis, it can be seen that the groundwater temperature is more important predictor of the drinking water temperature. According to the principal component analysis, both temperatures of ground and drinking water, are located at the same polar of a component 2, while the surface temperature lays in opposite[1] side of the component 2 (see Figure 4.12). Theory of heat transfer confirms the importance of groundwater outperforming influence; although both media are closely interrelated, the heat capacity of water is much bigger than the soil.

Thermal Contact Resistance

Blokker and Pieterse-Quirijns (2009) stipulate that pipe wall temperature is the same as soil temperature at the pipe depth. We will validate this assumption. Figure 4.9 shows that temperature gradient at the soil, pipe wall and drinking water interface differ at each location. From time series presented in Figure 4.9, it can be seen that location 2 has the biggest gradient between the drinking water and the pipe wall temperatures, whereas water temperatures at locations 1 and 3 (PVC pipes) are well phased with pipe walls and soil.

Table 4.2: Thermal Resistance values have been obtained from the averages of a difference between temperatures at the pipe wall and in the soil.

Location 1 (250 PVC)			Location 3 (125 PVC)		
$\overline{T_s}$ [°C]	$\overline{T_{pipewall}}$ [°C]	$R_{t,c}/q_x$ [°C]	$\overline{T_s}$ [°C]	$\overline{T_{pipewall}}$ [°C]	$R_{t,c}/q_x$ [°C]
10.90	10.59	-0.31	11.92	11.72	-0.20
Location 2 (250 CI)			**Location 4 (125 CI)**		
$\overline{T_s}$ [°C]	$\overline{T_{pipewall}}$ [°C]	$R_{t,c}/q_x$ [°C]	$\overline{T_s}$ [°C]	$\overline{T_{pipewall}}$ [°C]	$R_{t,c}/q_x$ [°C]
10.71	10.83	0.12	8.98	11.09	2.10

The same conclusion can be derived from the calculations of the thermal contact resistance factors (for thermal resistance values see Table 4.2). Calculations of a thermal contact resistance allow to discern the direction of the heat transfer flux and to give indication of how the vertical heat flux changes at interfaces of soil and pipe mediums. At temperature gradient is found between soil (S3) and pipe wall (S2) at every time interval (As it was explained in section 2.5.4 and equation 2.31 in chapter 2). Table 4.2 gives more details on the thermal heat flux resistance between the two mediums featured at each location.

[1]The direction and the length of the vector assigned to the different temperatures indicates how the variable contribute to the main components in the plot. The vertical axis represents a positive component for the temperatures influenced by the air temperature and a negative value for the temperatures in the substrate (i.e., soil temperature, pipe wall temperature, drinking water temperature). For the first principle component, all the seven variables are positive. Check Appendix for details.

Although locations 1 and 2 at the first sight look very similar, the heat fluxes there are opposite. Location 1 (PVC) yields the biggest thermal resistance while location 2 the smallest (CI). Interestingly, on average, the heat fluxes at locations 1 and 3 (PVC pipes) are towards the drinking water, whereas at locations 2 and 4 they are towards the soil. This may have something to do with thermal inertia of cast iron pipes which overtake temperature of drinking water faster than PVC pipes. Location 4 yields inaccurate values due to too big distance between the two sensors.

4.5 Soil Frequency and Depth of Heating

In chapter 1, one of the statements claims that the drinking water temperature is determined by the soil temperature. However, the soil and drinking water temperatures registered at Diemen Nort-West, differ in its variability. At the pipe depth, the drinking water temperature oscillates, which is manifested also at the pipe wall, especially at the cast iron pipes, whereas, soil temperature at this depth is stable and exhibit only seasonal changes. Figure 4.9 exemplifies; drinking water and pipe wall temperatures have short frequency oscillations not present in the air or soil temperatures series. The short oscillations are temperature exchanges between warmer drinking water with the colder pipe wall (see section 2.5–2.7 of chapter 2 for explanation).

Absence of the short wave oscillations in soil indicate two things: the soil layer in fact constitutes the largest thermal resistor and regulates the temperature changes in the drinking water conveyed in the pipes.

Daily Variations of Temperatures

Almost at all location, temperature of a pipe wall and drinking water temperature are slightly higher than the soil temperature which results in the heat flux direction from the pipes towards the bounding soil (see Figure 4.13 and 4.14). The gradient between the pipe wall and drinking water is however negligible. The heat flux, due to such negligible temperature gradient is small and therefore cannot be noticeable in the soil temperature.

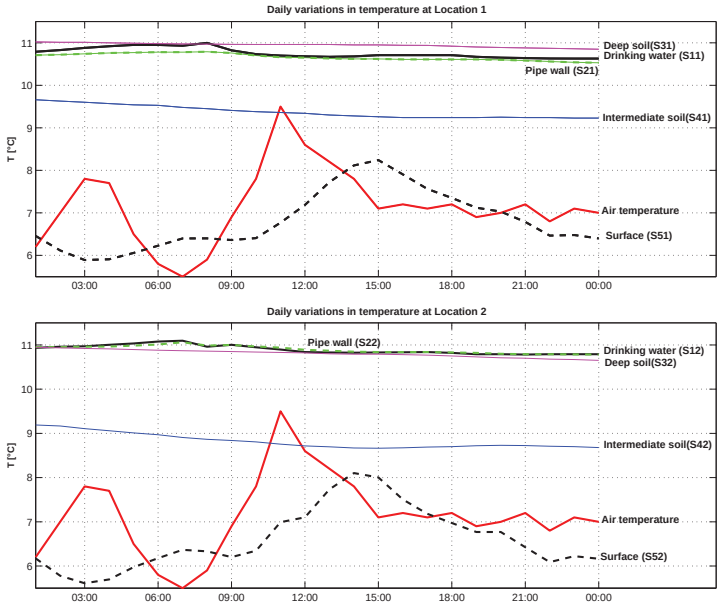

Figure 4.13: Daily temperature variations registered at Locations 1 and 2. - Undistinguished daily variation in the drinking water temperature vs. air temperature variations at Locations 1 and 2.

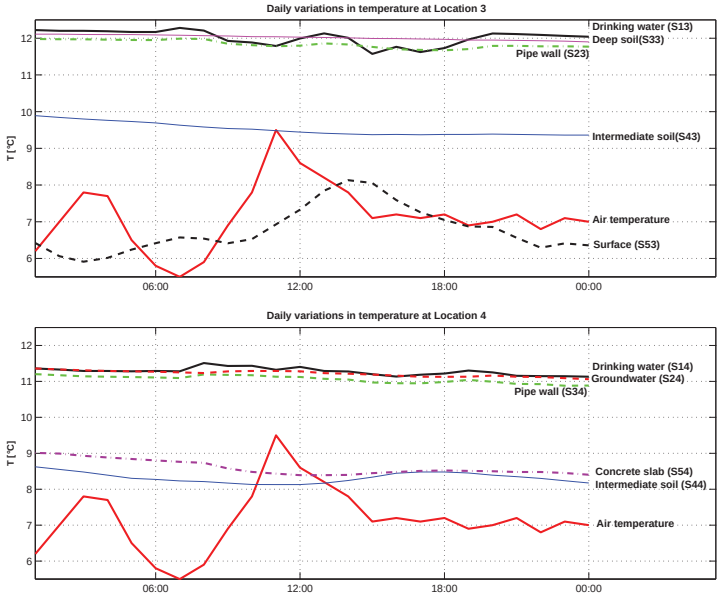

Figure 4.14: Daily temperature variations registered at Locations 3 and 4. - An arbitrary day was chosen on the basis of a big air temperature variations (end of November 2009). The drinking water temperature varies during that day at Location 3. The variations are however tenuous; smaller than 1°C.

Soil Temperature Spectrum Analysis

Lack of smaller diurnal temperature changes is expected when looking at the analytical solution of the soil diffusion equation (section 2.5.3 chapter 2). Diurnal surface temperatures oscillate less during colder seasons. There is less influence of the net radiation therefore heating and cooling processes shown in Figure 2.2 in chapter 2 are less distinct. The amplitude of fluctuations within the soil decays exponentially with distance from the surface thus it is expected that at depths soil will have stable temperature.

In order to verify till which depth the diurnal changes may occur at the four observed locations, Fast Fourier has been used (see Appendix A.8). The analysis was performed on the de-trended data set (see Appendix A.6). A data set consisting of 7112 cleaned data points has been used for the analysis. The bigger trends have been removed with the robust linear regression. For calculations an estimated value of diffusivity obtained by optimization were taken (as listed in Table 5.2). As can be seen from Figure 4.15 temperature variation frequency is similar for each location and each sensor. The strongest signals from the sensor installed near the surface and resulting damping depths for every location are listed in Table 4.3.

Table 4.3: The damping depths calculated according to the Fourier analysis performed on sensor 5 and 3.

	Frequency	Power	ω	Damping depth
SURFACE	1/day	-	rad/day	m/day
Location 1	6.8E-03	1.0E+06	4.3E-02	8.4E-03
Location 2	7.2E-03	8.0E+06	4.5E-02	8.2E-03
Location 3	6.9E-03	1.0E+05	4.4E-02	8.3E-03
SOIL				
Location 1	6.9E-07	5.0E+06	4.4E-06	8.3E-01
Location 2	2.1E-06	3.0E+06	1.3E-05	4.8E-01
Location 3	2.1E-06	3.0E+06	1.3E-05	4.8E-01

Results confirm that the pipe burial depth is below the damping depth (see Equation 2.29 in chapter 2). The strong diurnal waves that are present near the surface have a frequency of about one day and reach very shallow depths. The other weaker waves showed in the table, occur more than once per day. Those frequencies are only getting weaker with depth. Sensors situated deeper in soil register only small temperature oscillations. The thermal damping depth is reciprocal to the frequency, and as it is getting stronger the damping is getting weaker. However, it should be reminded that the strongest seasonal signals are filtered out. The assumption taken in the model developed by Blokker and Pieterse-Quirijns (2009), that the temperatures variations are negligible at the burial depth are valid for the

diurnal calculations. As Figure 4.5 demonstrates, soil temperature diurnal fluctuations increase their frequency and amplitudes in warmer seasons. Therefore, seasonal soil temperatures indeed determine pipe wall, thus indirectly drinking water temperature. But diurnal soil heat fluxes have only impact during summer when their amplitudes are strong enough to reach the pipe depth. During colder periods it is the incoming water that drives temperature oscillations at the pipe wall.

Soil as a Thermal Storage

Especially during the moderate seasons, like autumn, at $1\mathrm{m}$ depth the heat exchange with the atmosphere stops and the heat storage starts. The heat storage in the soil is noticeable in Figure 4.6. The temperature at the surface starts at $15°\mathrm{C}$ decreases at $0,5\mathrm{m}$ depth to $10°\mathrm{C}$ to rise again to $12°\mathrm{C}$ at $1\mathrm{m}$ depth.

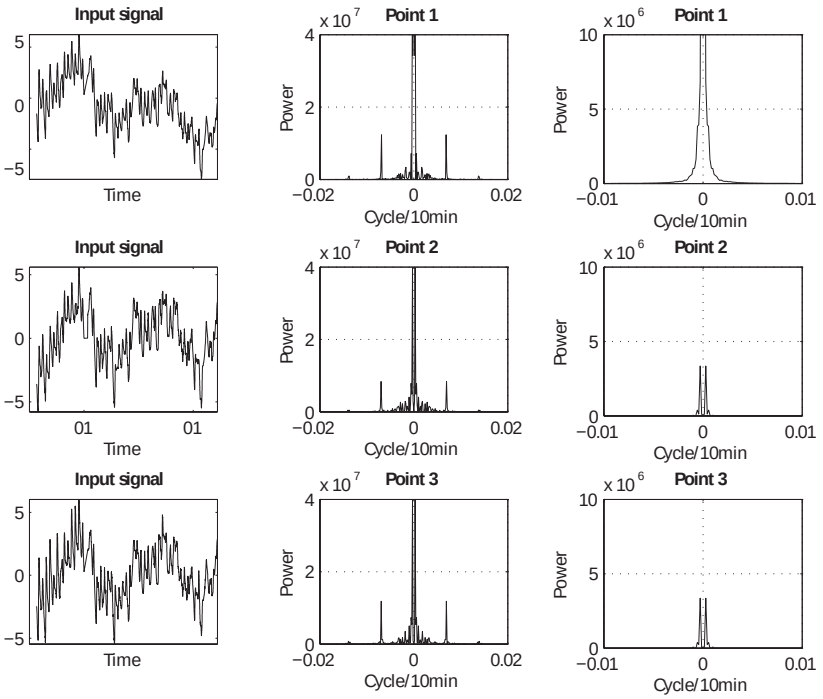

Figure 4.15: Comparison of the FFT at different depths and different Locations 1-3 in west part of Diemen Noord. - From left to right: The input signal is the de-trended temperature from the surface (sensor 5). Second column shows the FFT of that signal. Third column shows the FFT of the signal from -1m depth in soil (sensor 3). The signals units are in K. The power indicates an absolute power of the signal in the frequency spectrum calculated as fraction of squared temperature amplitude to the sampling frequency. Source: FFT. Mathworks.com

5

Model Validation

5.1 Introduction

This chapter is dedicated to analysing a sensitivity of drinking water temperature to hydraulics, and testing drinking water temperature distribution in a network during the heat wave conditions.

During the heat wave conditions, the drinking water temperature depends indirectly on the air temperature and directly on the soil temperature. Our claim is that in order to obtain the temperature of the soil at burial depth, it is necessary to use a heat transfer model like the soil model developed by Van Der Molen et al. (2008), that resolves temperature input in vertical. We were able to validate the soil model developed by Van Der Molen et al. (2008) with soil temperature measurements, which are hardly ever available at drinking water companies.

Nevertheless, this chapter does not intend to calibrate the soil parameters in order to improve performance of the soil models; rather it focuses on the analysis of the errors introduced by such model. The aim of the analysis is to define if the soil temperature can be applied as a scalar to the entire network[1] and if not what improvements can be introduced.

The algorithm developed by Blokker and Pieterse-Quirijns (2009), that calculates the exit drinking water temperature, was implemented in the Epanet 2 MSX platform. Next, we simulated drinking water temperature transport, in the calibrated North-West supply network of Diemen, and then tested heat wave scenarios. We reported on results that are general thus applicable to other parts of Waternet network.

[1] Since in Epanet 2 MSX platform, the spatial variability if not accounted for, it is difficult to estimate if calibration of the soil model would improve results of our analysis; it may only improve temperature input at one point in a network which could result in a bigger error at a different point in a network.

5.2 Soil Model Validation

Model Initialisation

The imposed boundary values are often source of a big error in numerical models (Blokker and Pieterse-Quirijns (2009) termed it 'initialisation'). Therefore, our model has been trained for a longer time interval. The initialization was removed by extending the calculation period from 7th November 2009 till 5th December 2009 to 1st January 2009 till 5th December 2009. In fact the validation period is between 7th November 2009 5th December 2009–a period in which soil and drinking water temperatures are available.

Preliminary Results

The preliminary tests with the standard settings of the soil model of Van Der Molen et al. (2008) indicated that its application to predict the soil temperature led to inaccurate results. The simulated temperatures at location 1 (concrete surface) and 4 (bare soil surface) are identical even though there are crucial differences in the surface characteristics and boundary temperatures observed at those locations (differences can be seen in Figure 4.12, chapter 4). At both locations simulated temperatures start at around 11 9°C and drop till 10°C. The same similarity can be found in temperatures at locations 2 and 3, but both those spots share similar coverings. As can be seen from the results juxtaposed in Figures 5.1 and 5.2 there is a systematic error and trend in data.

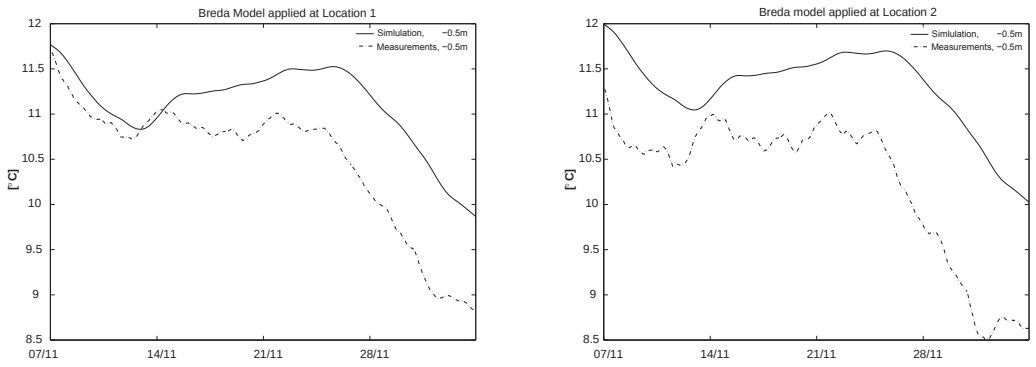

Figure 5.1: The soil model validation applied at Locations 1 and 2. Model has been validated for the period of 7th November - 5th December 2009. Dotted line represents simulation of the model and solid line represents measurements. Both temperature are from the depth of 50cm.

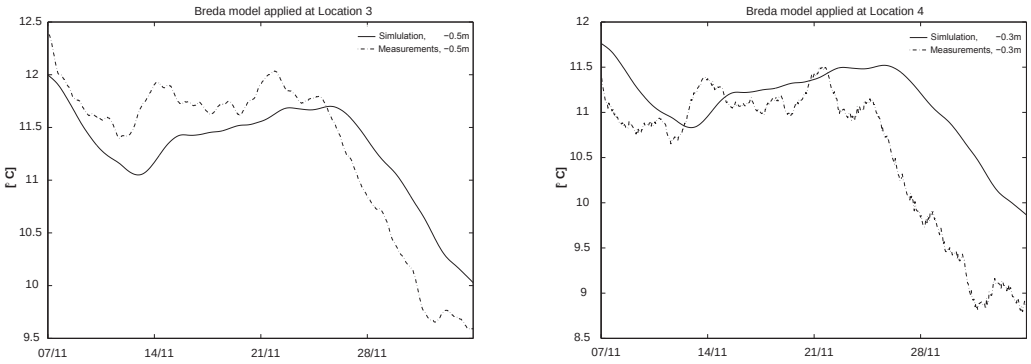

Figure 5.2: The soil model validation applied at Locations 3 and 4. Model has been validated for the period of 7th November - 5th December 2009. Dotted line represents simulation of the model and solid line represents measurements. Both temperature are from the depth of 50cm.

As can be seen from Figures 5.1 and 5.2, preliminary tests of the soil model of Van Der Molen et al. (2008) yielded a maximum error of 1°C at locations 1 and 4, 1.5°C at location 2 whereas at location 3 the maximum error reaches merely value of 0.4°C. Magnitude of those errors renders insignificant but it requires more investigation for two reasons. Firstly, a closer look at the propagation of the residuals reveals downward trend in series. Good correlation between observed and simulated temperatures might have been thus partially caused by a shared decreasing trend. Secondly, simulated temperature is less variable than observed temperature. The model should reflect realistic temperature oscillations in order to be able to correctly represent dynamic and diurnal temperature changes. In fact, during warm seasons the amplitude and frequency of diurnal oscillations increases.

The trend visible in validation results, should be removed in order to obtain more trustworthy fit between observed and modelled temperatures. Trend removal can be done by applying robust linear regression to the residuals. Relevant methodology is described in Appendix A.6. The cleaned temperature time series vary around zero, giving a clear picture of residuals. Statistics describing changed and original temperature time series is given in Appendix A.10.

Minimizing the Error

According to the plots of residuals (Figure 5.3) the soil model performs well at location 3. Root mean square error, which is the standard deviation of the unexplained variance from the mean value and measures models precision, is the lowest at location 3. However, according to Nash-Sutcliffe coefficient (better fit if the value if closer to 1), locations 2 and 4 are fitted better to the observed temperatures.

Table 5.1: Summary of the soil model validation errors.

Error	Location 1	Location 2	Location 3	Location 4
min	-1.81	-3.06	-2.13	-3.81
max	0.14	0.12	0.48	0.98
RMSE	0.95	1.48	0.93	1.68
NS	0.59	0.73	0.50	0.76

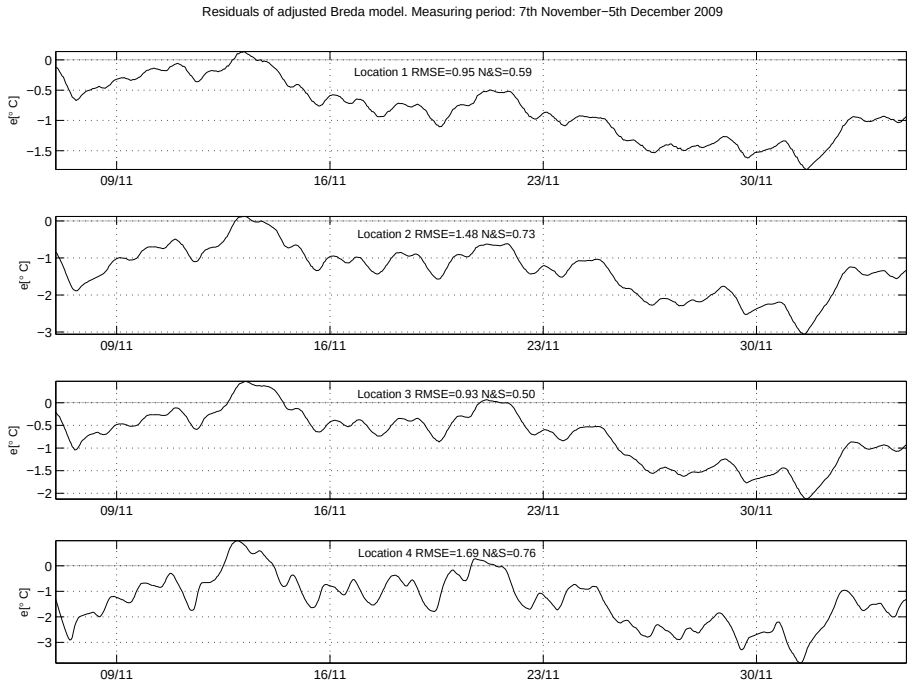

Figure 5.3: Residuals of error between observed and predicted the soil temperature after removing seasonal trend. Locations 1-4. - The residuals of the model developed by Van Der Molen et al. (2008) have been plotted as times series for all four locations. The thermal properties of the receiving layers have been chosen according to the default settings.

After the trend removal, the error sequence, presented in Figure 5.3, diverges in time which points out that the values of the soil temperature can not be predicted within a clearly defined confidence levels.

The origin of the error can be manifold. In general, any failure of the model to accurately reflect the measured temperature at the pipe wall can be due to: (i) inaccuracy of the input data due to faults in a measuring equipment (wrong configuration, transmission problem or misread), (ii) numerical error embedded in the modelling process, (iii) model failure to reflect the system's processes or variability

(temperature oscillates less).

Typical sources of errors in a temperature measurement taken with electrical resistance thermometers can be: (i) self-heating of the thermometer element, (ii) inadequate compensation for non-linearities in the sensor or processing instrument, (iii) resistance bridge circuit (WMO, 2008). Those error cannot be quantified but are reflected in the quality of input data. The data has been cleaned and homogenized for the purpose of this modelling.

Modelled temperatures overstate the observed soil temperature values. This points towards possibility that value of a thermal diffusivity parameter is bigger. Therefore, calibration of the thermal diffusivity coefficient was performed on the cleaned data.

Calibration of Soil Thermal Properties

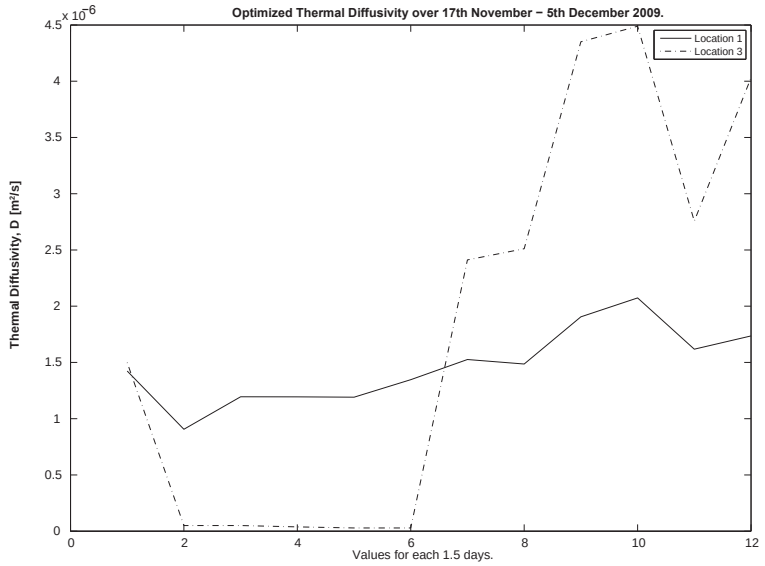

Figure 5.4: Example of optimized values of diffusion coefficients at Locations 1-3 derived from the multi-objective function. - Arbitrarily time interval of 1.5 days length.

Based on the estimated soil thermal properties at Diemen Noord (table 3.4) applied to the model, the diffusivity should be around 1-1 $5\mathrm{m}^2/\mathrm{s}$. To verify that we have used the calibration based on multi-objective function [1], which estimates a value of a diffusivity coefficient directly from temperature measurements obtained at different depths in the soil. The optimisation engine calculates soil's diffusivity for a moving window of 1 day per every 3hrs. The optimal value of the thermal diffusivity is obtained

[1] The calculation algorithm was written in MATLAB by and supplied to the author by courtesy of Susan Steele-Dunne.

by finding minima in objective function. The objective function represents a root-mean-square error from a difference between the measured and the projected temperatures. The minimisation algorithm uses the Nelder-Mead direct search method (Steele-Dunne et al., 2010).

Optimization Method Evaluation

Diffusion values obtained by the calibration change drastically (see Figure 5.4 and Table 5.2). Furthermore, there are distinct differences between the diffusivity at locations 1 and 3. Given similar soil thermal properties at all locations, an explanation of the diffusivity differences should be sought in a difference in the soil water content.

At location 3 the optimization algorithm indicated zero diffusivity, which may indicate that the temperature gradient between two sensors was close to zero rendering instabilities in the optimisation algorithm. The found diffusivity values are beyond reasonable values expected from the literature (Korevaar et al., 1983).

Radical changes in the diffusivity value at location 3 may be cased by the fact that the soil was re-organized during the experiment preparation[1] and probably there are still some gasps in the soil which resulted in changes to soil properties. However, average parameters resulted from the calibration correspond well with the values applied in the model developed by Van Der Molen et al. (2008).

Table 5.2: Results of the diffusivity search via multi-objective optimization algorithm. Location 4 due to specific experimental set-up was excluded from the analysis.(Algorithm source: Susan Steele-Dunne.)

	Units	Max	Av	Min
Location 1	$10^6 \mathrm{m}^2/\mathrm{s}$	2	1.455	0.91
Location 2	$10^6 \mathrm{m}^2/\mathrm{s}$	3.74	2.65	0.22
Location 3	$10^6 \mathrm{m}^2/\mathrm{s}$	4.99	1.18	0.31

As Steele-Dunne et al. (2010) stipulates, the diffusion values obtained directly form the measurements have several shortcomings. In the method a homogeneous diffusion over the depth is assumed. In addition, the diffusivity obtained this way is an 'apparent' diffusivity which uses primarily conduction as the only heat transfer mode. The 'apparent' diffusivity is influenced by other latent and sensible heat fluxes not represented in the model but most probably present in reality (at least at location 4).

[1] The algorithm fails to cover an optimum value, when the net radiation is low and the temperature gradients are small(Steele-Dunne et al., 2010). The inaccuracy may have something to do with precipitation. The conduction of heat takes please through all kinds of sequences of the conducting materials organised in series and in parallel. The value of conduction coefficient depends on the way in which the best conducting mineral particles are interconnected by less conducting water phase and are separated by the poorly conducting gas phase, (Korevaar et al., 1983). Any changes in a balance of the water and air phases can cause a thermal bridge where the heat is conducted faster or slower.

Optimized Model Results

We have used an alternative soil model[1]. The improvements to the model of Van Der Molen et al. (2008) were pursued by inclusion of soil moisture and stratification in the vertical layers (according to layers listed in Table 3.4). The new alternative soil model was an extension of the model of Van Der Molen et al. (2008). As state variables we have used thermal properties based found by optimization. In the model, we included the soil moisture content[2], divided the soil layers into a number of sub-layers with variable thermal properties. There are no weather data are included in the improved model.

The temperatures obtained from the two subtended NTC sensors located in one vertical ((S5) and (S3); see Table 3.9 chapter 4 for reference) were used to calculate a temperature gradient for a time step of a minute and a grid space of five centimetres in the soil vertical (based on equation 2.25). Simulated temperature values were contrasted with the temperatures registered at the third sensor (S4) which was located in the middle of the S5 and S3 (see Figure 3.7 to check the sensors arrangement).

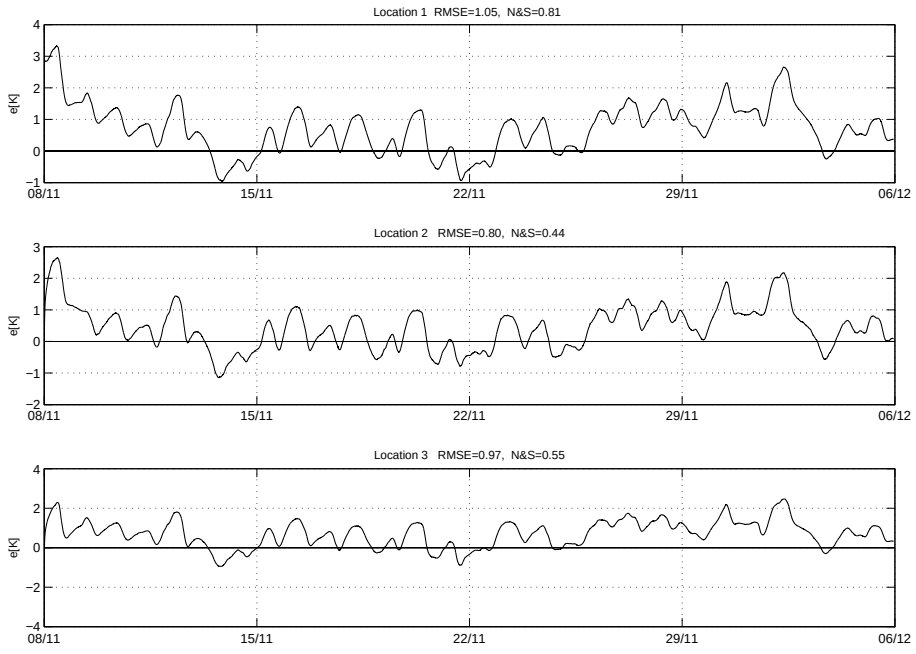

Figure 5.5: Residuals of optimized model prediction vs. observation. - At the top of the figure root mean square and variance of the error are given.

[1]The codes used in the optimized model are given in Appendix A.12.

[2]The soil moisture content under the concrete tiles, is assumed to be 20 percent of the porosity and have an exponential decay.

Figure **??** examines results of the model prediction. The measured temperatures are less variable. The model overestimates the amount of cold that intrudes into the soil.

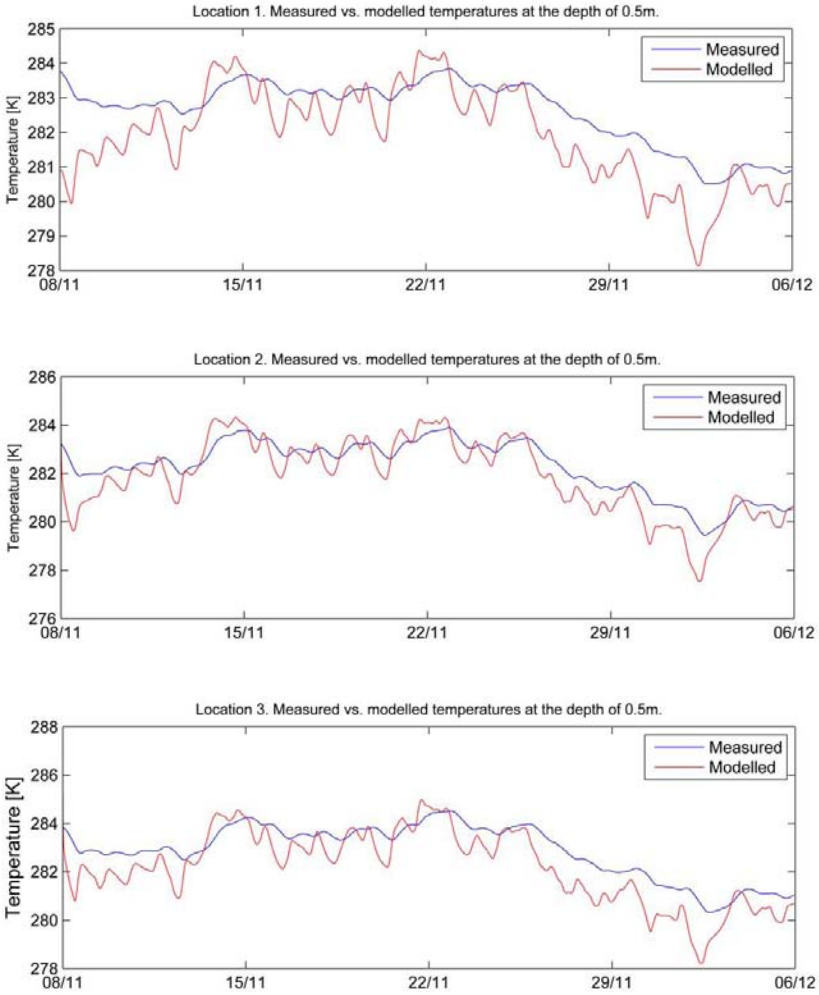

Figure 5.6: Validation of the two dimensional soil diffusivity model vs. observed temperatures. - Validation of the optimized error at locations 1, 2 and 3.

Figure 5.5 presents the modelling errors. It can be seen from the time series of the residuals that observed temperatures are on average $1\mathrm{K}$ (or $1^{\circ}\mathrm{C}$) higher than the modelled. The biggest error occurs around 29/11/09 at all locations. According to Figure 4.8 from chapter 4, this was a period of intense rainfall events (rainfall depth was up to $5\mathrm{mm}$). During that time soil moisture increased and elevated values of diffusivity were modelled. Similar effect was described in (Steele-Dunne et al., 2010).

Inventory of Imposed Modelling Uncertainties

In case no measurements are available, predicting the vertical propagation of temperature from the surface to the pipe wall to estimate the temperature of drinking water in a network requires usage of at least two models: surface heat balance and a soil diffusion model (see . Value of the temperature of drinking water in a network is highly influenced by the predictions of the pipe wall temperature. In previous chapter (Section 4.6, Table 4.5) it has been confirmed that the difference between the temperatures of the pipe wall and the soil at the same depth, are negligible. Thereby, the vertical heat transfer model such as one developed by Van Der Molen et al. (2008) or Steele-Dunne et al. (2010) can give a meaningful information. Outcome of the modelling was not always accurate. But as Savenije (2007) equated the model accuracy to the bias of the simulation, whereas model precision to the prediction uncertainty. If we follow this line of reasoning, then our aim is to have a model that would give a estimation of the average values of temperatures at the depth we require.

The models are highly sensitive to the air temperature and global radiation values. Table 5.3 identifies possible errors inferred from the sensitivity analysis. The purpose of the soil model validation analysis was to depict and estimate a possible errors and sensitivity to the soils thermal properties and water content. Table 5.4 identifies possible errors inferred from the validation. The largest errors result from faulty estimation of soil thermal properties (diffusivity).

Table 5.3: Summary of the uncertainties.

Model	Data	Sensitivity
soil model	wind speed	low
	albedo	medium
	global radiation	high
	air temperature	high
	precipitation	high
	accuracy of the weather data	high
	soil thermal properties	high
	thermal resistance	low
	soil temperature	high

Table 5.4: Summary of the largest errors.

Model	max. RMSE
default soil model by Van Der Molen et al. (2008) (after data cleaning)	$1,6°C$ $(1,68°C)$
optimized diffusion model (based on pure diffusion model by (Steele-Dunne et al., 2010))	$3,5°C$

5.3 Analysis of Drinking Water Temperature in a Network

Test Period

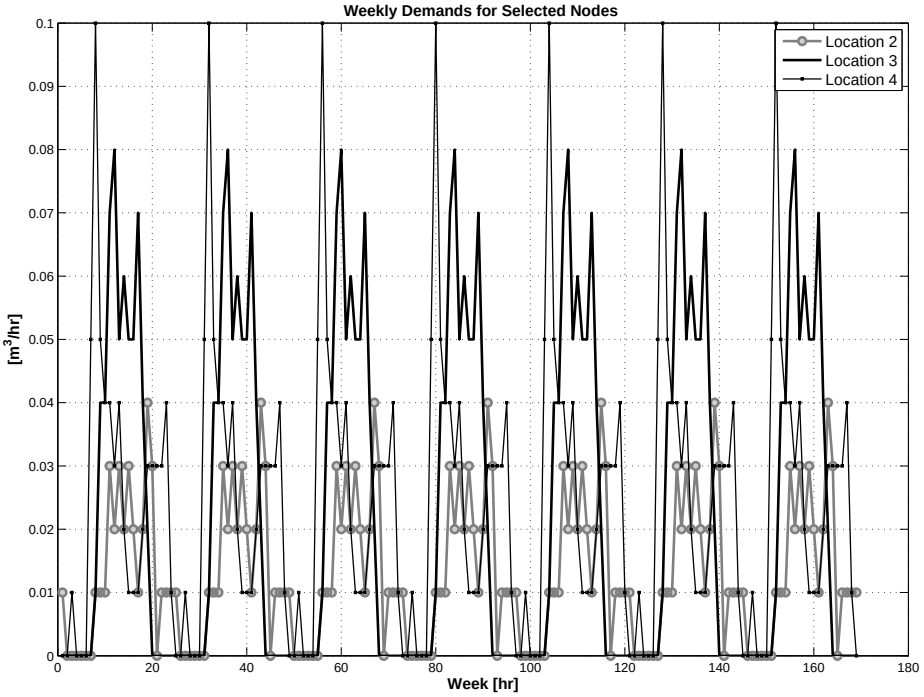

Figure 5.7: Plot of demands calculated by the models at monitoring locations 1 - 4. - Location 1 has the same demand as flow meter at the start of the network.

Calculations of the exit water temperature in a network was done in Epanet 2 extended with Epanet MSX. Blokker and Pieterse-Quirijns (2009) stipulates that heating time in a PVC pipes can take days. Thereby, it was clear that a period of one week would be the required simulation interval. From Figure 4.8 (Chapter 4) it can be seen, that three time phases can be depicted in the time series obtained during the measuring period B: a period where the soil temperature remains relatively stable, a week from 8th of November 2009 - 15th of November 2009 and week in a period from 29th of November 2009 - 6th of December 2009, a period where the soil temperature is linearly decreasing in time, a period from 15th of November 2009 - 29th of November 2009 . In this analysis,we have used a stable soil temperature period (15th of November 2009 till 22nd of November 2009).

Real Discharges Calculation

Hydraulic model based on the nodal consumption projected in section 4.4.2 in chapter 4, have been fed to the Epanet 2 software. A compound average residence time has been derived from the resulting demands (see Figure 5.8). The residence time has been calculated according to domestic and industrial measured demands. The residence time pattern at location 4 stabilizes after one week.

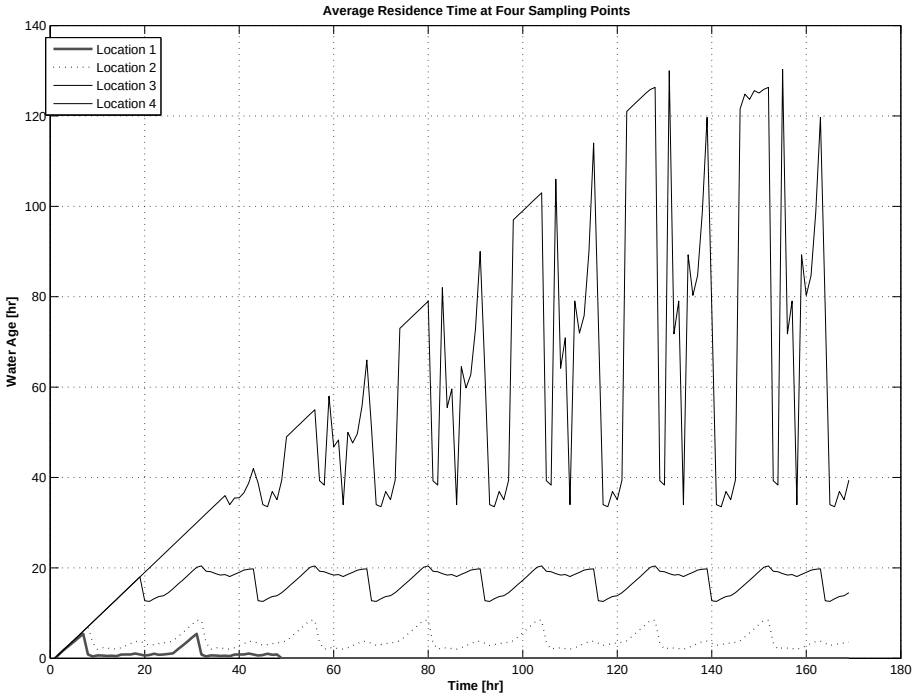

Figure 5.8: Average hydraulic residence times calculated by the models at monitoring locations 1 - 4. - Average hydraulic residence times are based on demands calculated by the Epanet 2 model at monitoring locations 2 - 4. Location 1 has the same demand as flow meter at the start of the network.

Temperature Distribution in a Network

The preliminary network runs were conceived to check credibility of the Epanet MSX predictions. Appendix A.12 contains the MSX input file with a water temperature settings applied to the Diemen network model. The settings assumed nearly constant pipe wall temperature and a constant temperature of an incoming water maintained at the entrance. The verification results are given in Figure 5.9.

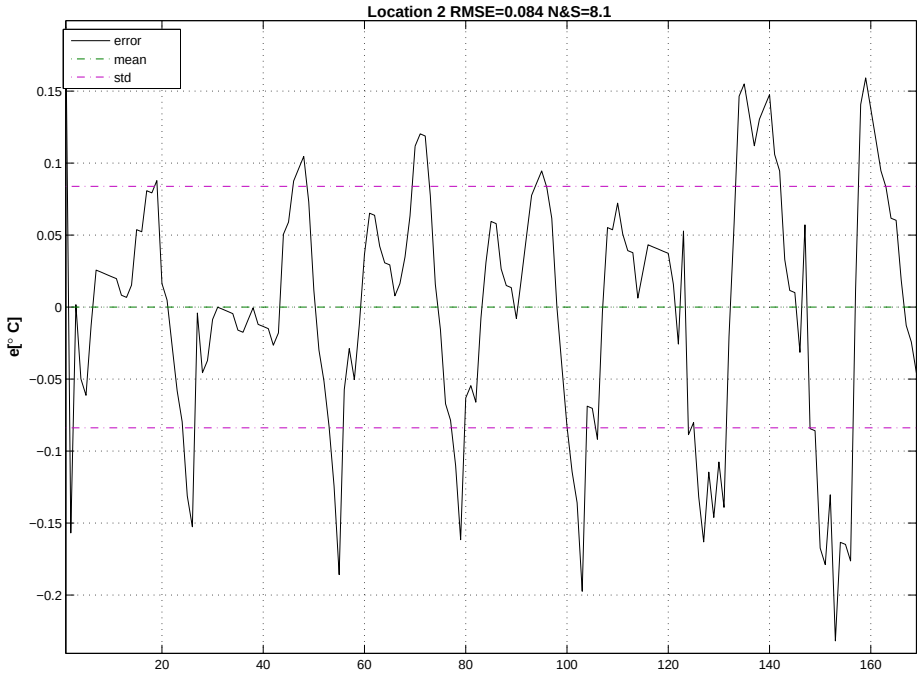

Figure 5.9: Residuals of error between observed and modelled drinking water temperature at locations 2. - The resulting standard devaition and error mean are given in the picture. (see chapter 3, section 3.7 for details on validation.

Inventory of Imposed Modelling Uncertainties

Exit drinking water in a network estimated by the soil model by (Van Der Molen et al., 2008) and Epanet 2 include intrinsic errors. In general errors can propagate from the model or data. Since predicting the exit drinking water in a network require usage of at least four models: surface heat balance, soil model, a pipe model and hydraulic model, there will be at least four errors that will lower the confidence of the temperature prediction. Table 5.5 identifies maximum errors inferred from the sensitivity analysis (qualitatively) or approximated from the validation analysis. Those errors could result in an over- or understatement of the sought exit water temperature.

5.4 Scenarios testing

The two questions that we aim to answer by scenario testing are: (i) if the soil warms up during summer days, how long will it take until it affects drinking water?, (ii) if we cool down the incoming drinking

Table 5.5: Summary of the uncertainties.

Model	Data	Sensitivity	max. RMSE
surface heat balance model	wind speed	low	
	albedo	medium	
	global radiation	high	
	air temperature	high	
	precipitation	high	
soil model	soil thermal properties	high	
	thermal resistance	low	
	soil temperature	high	$3,5°C$
drinking water in a network	discharge	medium	$1,3m^3$/hr
	pipe geometry	medium	
	pipe corrosion	medium	
	incoming water temperature	high	
	demands allocation	high	

water, how long will it take until the remaining parts of the network are affected?

In order to answer this question three scenarios have been prepared. First scenario, assumes a situation of a heat wave, when the soil temperature is $25°C$, the incoming water temperatures and the network water are moderate, summery temperatures of around $20°C$. The initial temperatures are the same as displayed in Figure 5.3 but increased by $10°C$.

Second scenario, assumes an imaginary situation, when the soil temperature is high, $26°C$, while the water temperature in a network and the incoming water are kept as in original series (see Figure 5.3 in chapter 5). Third scenario, assumes the after- heat-wave situation where the soil and the water temperature in a network remain moderate, around $20°C$ but the heat is extracted the the start of the network. The temperature at the first node is thus much lower, $0,9°C$ (heat extraction).

Results are given in form of isotherms and temperature values at every node of a network at a given time interval. The results can be compared with the average hydraulic residence time as calculated by the Epanet 2 given in Appendix A.13. We present the initial values before the tests for the temperature distribution, the results after 30 hours (next day at 6 o'clock in the morning when the demands starts to elevate) and after one week. The remaining results can be obtained at request from the author.

Scenario one

Initial Temperatures

The temperatures in the network are the initial values from the original temperature time series at t_0 applied at nodes 1, 46 and 62 which represent locations 1, 3 and 4 (see Figure 5.10), respectively (see Table 5.6).

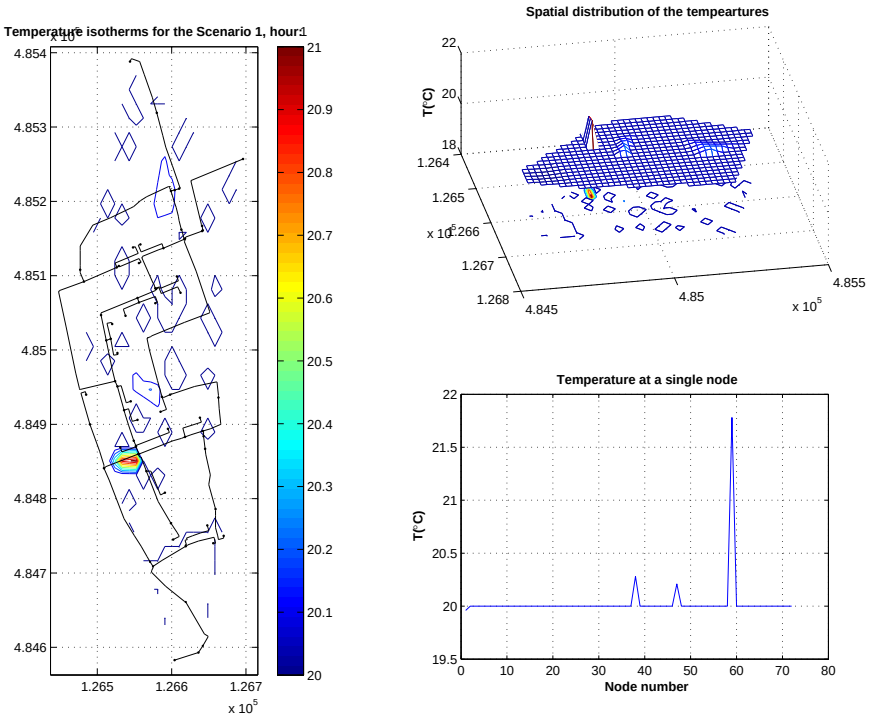

Figure 5.10: Temperature distribution in a network at a first hour for a realistic demand patterns. Scenario 1. - The right side of a graph shows the temperature cloud travelling in a network (top) and the temperatures at individual nodes (bottom). The nodes temperatures are interpolated into isotherms and plotted on the network pipes. The water in fact is in the pipes. Isotherms intend to give a glimpse on the spatial distribution.

One Day Temperatures

After one day (30 hours), the temperatures are already pretty well mixed and we can clearly see how the temperature in a network plummets due to that mixing. The only pipe that are still around soil temperature are pipes at nodes: 50, near location 4 (see Figure 5.11). Initially, the gradient in a network was $1,5°\mathrm{C}$. After 30 hours it is $2,5°\mathrm{C}$ while the gradient between the soil and water remains on average $5°\mathrm{C}$.

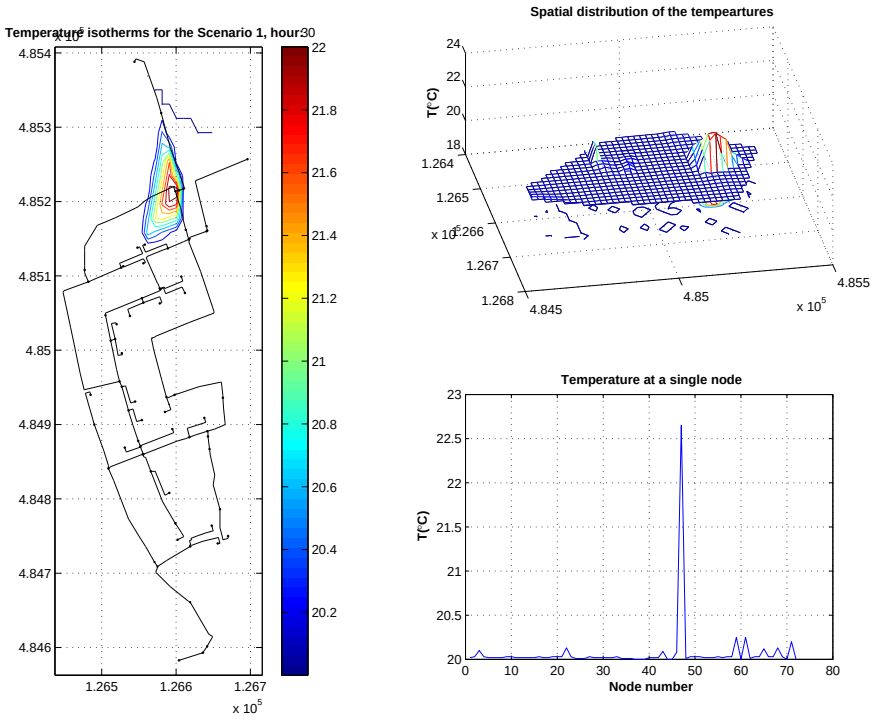

Figure 5.11: Temperature distribution in a network at 6 o'clock on a second day of Scenario 1. - The right side of a graph shows the temperature cloud travelling in a network (top) and the temperatures at individual nodes (bottom). The nodes temperatures are interpolated into isotherms and plotted on the network pipes. The water in fact is in the pipes. Isotherms intend to give a glimpse on the spatial distribution.

One Week Temperatures

After one week (168 hours), the temperatures should reflect a mixture of soil and temperature of the water that resides in the network. The soil decreasing trend is visible in the final temperature plot at the nodes. Boundary values at location 4 increase the average temperatures (see Figure 5.12) in the network. On average temperatures have increased as compared to the temperatures after one day but the peaks are $2,1°\mathrm{C}$ lower.

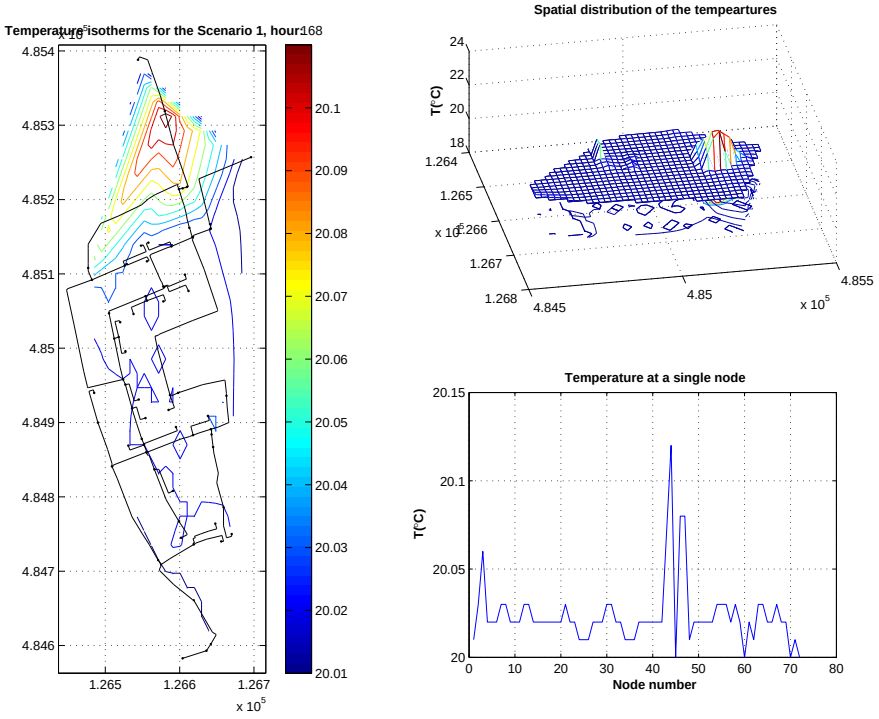

Figure 5.12: Temperature distribution in a network at 12 o'clock on a 7th day of Scenario 1. - The right side of a graph shows the temperature cloud travelling in a network (top) and the temperatures at individual nodes (bottom). The nodes temperatures are interpolated into isotherms and plotted on the network pipes. The water in fact is in the pipes. Isotherms intend to give a glimpse on the spatial distribution.

Table 5.6: Scenario one temperature settings.

Temperature	Soil	Incoming water	Network global water	Sampling locations
Set-point values	25°C	20°C	20°C	+ 10°C

Scenario Two

Initial Temperatures

The temperatures reflect the initial values applied at points 1,3 and 4 with peak values at nodes 62 (maximum) and 46 (minimum). Nodes 46 and 62 are the nodes of locations 3 and 4 (see Figure 5.13). At this scenario initial values are cooler than in scenario 1 (see Table 5.7).

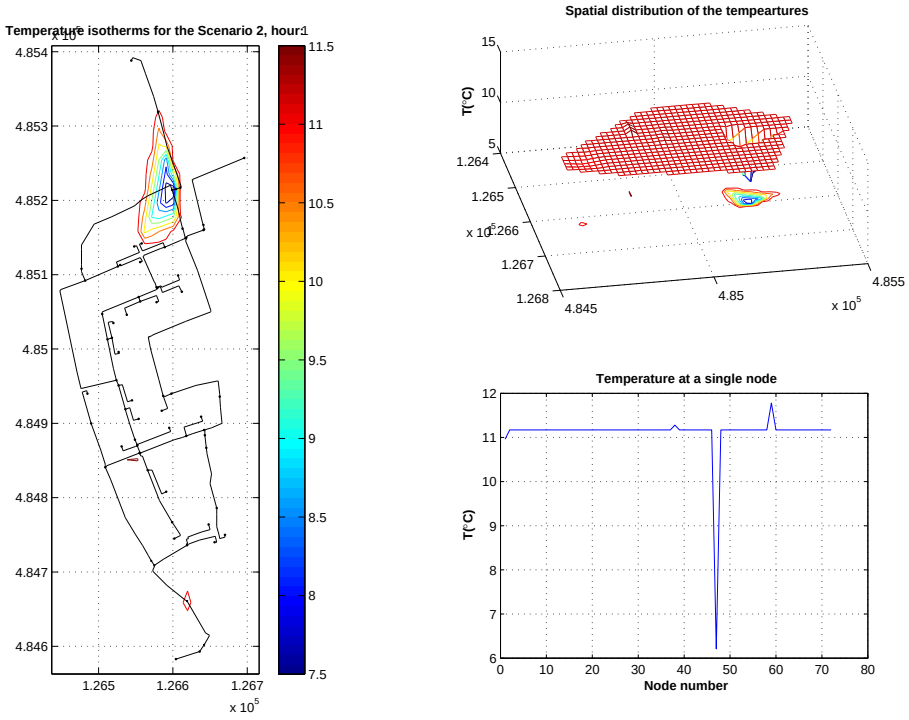

Figure 5.13: Temperature distribution in a network at a first hour for a realistic demand patterns. Scenario 2. - The right side of a graph shows the temperature cloud travelling in a network (top) and the temperatures at individual nodes (bottom). The nodes temperatures are interpolated into isotherms and plotted on the network pipes. The water in fact is in the pipes. Isotherms intend to give a glimpse on the spatial distribution.

One Day Temperatures

After one day (30 hours), the temperatures are already pretty well mixed and we can clearly see how the temperature in a network plummets due to that mixing. The only pipe that are still around soil temperature are pipes at nodes: 50 so location 4 (see Figure 5.14). The gradient in a network after 30 hours is 7°C while the initial gradient between the soil and water was 16°C.

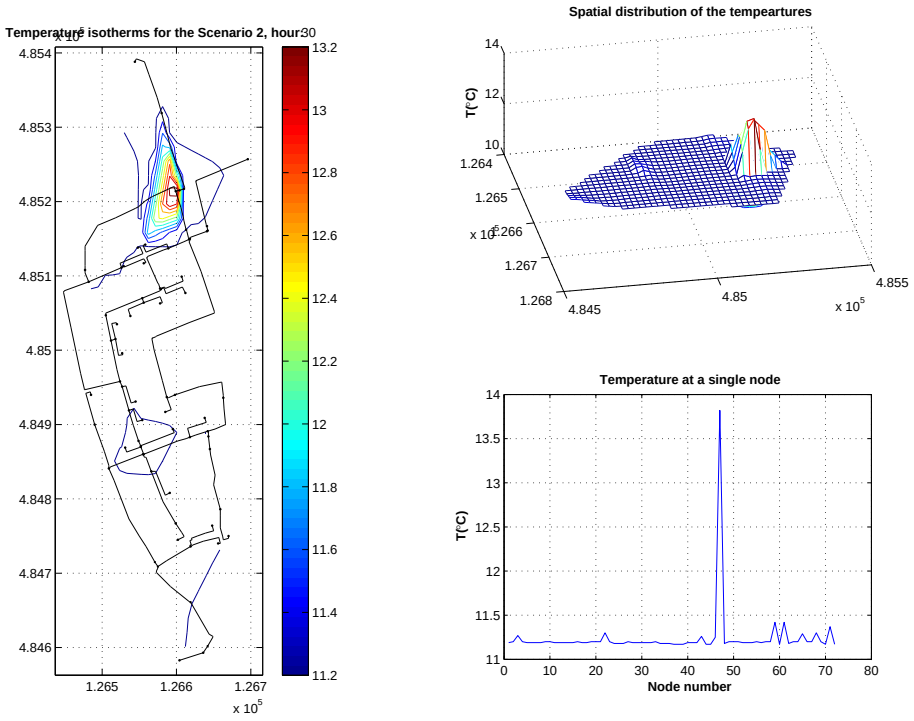

Figure 5.14: Temperature distribution in a network at 6 o'clock on a second day of Scenario 2. - The right side of a graph shows the temperature cloud travelling in a network (top) and the temperatures at individual nodes (bottom). The nodes temperatures are interpolated into isotherms and plotted on the network pipes. The water in fact is in the pipes. Isotherms intend to give a glimpse on the spatial distribution.

One Week Temperatures

After one week (168 hours), the temperatures are already pretty well mixed and we can clearly see how the temperature in a network elevates due to that mixing. The only pipes that are still lower temperatures are peripheral pipes at nodes: 40-42, 44-45 and 60 (see Figure 5.15).

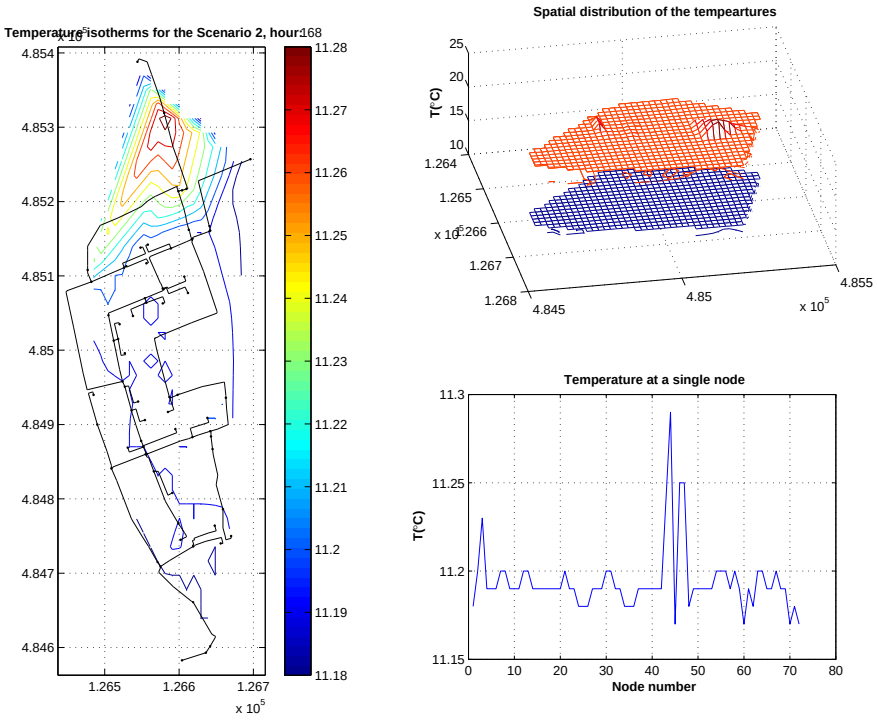

Figure 5.15: Temperature distribution in a network at 12 o'clock on a 7th day of Scenario 2. - The right side of a graph shows the temperature cloud travelling in a network (top) and the temperatures at individual nodes (bottom). The nodes temperatures are interpolated into isotherms and plotted on the network pipes. The water in fact is in the pipes. Isotherms intend to give a glimpse on the spatial distribution.

Table 5.7: Scenario two temperature settings.

Temperature	Soil	Incoming water	Network global water	Sampling locations
Set-point values	26°C	11°C	11°C	original

Scenario Three

Initial Temperatures

The temperatures reflect the initial values applied at points 1,3 and 4. At node 1 the cold water is applied. At the remaining nodes; 46 and 62 the temperature time series from measurements at locations 3 and 4 are applied, around 21°C (see Figure 5.16). Global water temperature is 23°C, soil temperature 20°C (see Table 5.8).

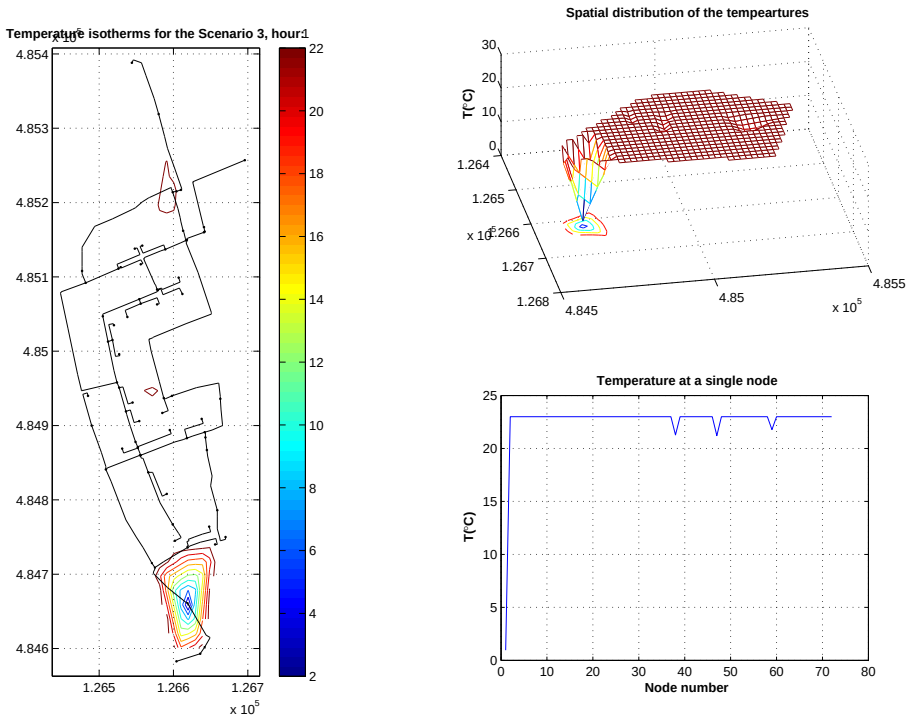

Figure 5.16: Temperature distribution in a network at a first hour for a realistic demand patterns. Scenario 3. - The right side of a graph shows the temperature cloud travelling in a network (top) and the temperatures at individual nodes (bottom). The nodes temperatures are interpolated into isotherms and plotted on the network pipes. The water in fact is in the pipes. Isotherms intend to give a glimpse on the spatial distribution.

One Day Temperatures

After one day (30 hours), we see how the temperature can be elevated in a network. From the global temperature of 23°C the water have risen to $25,5$°C due to mixing and long residence time near location 4 (node 48). The peripheral pipes at nodes: 40-42, 44-45 and 60 are insignificantly highier (see Figure 5.17).

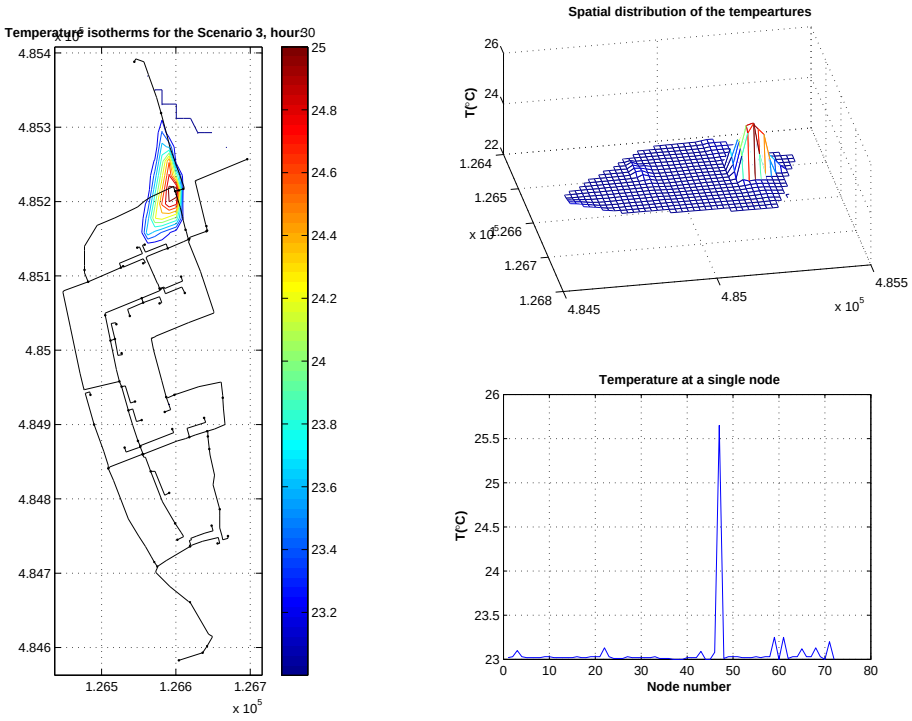

Figure 5.17: Temperature distribution in a network at 6 o'clock on a second day. Scenario 3. - The right side of a graph shows the temperature cloud travelling in a network (top) and the temperatures at individual nodes (bottom). The nodes temperatures are interpolated into isotherms and plotted on the network pipes. The water in fact is in the pipes. Isotherms intend to give a glimpse on the spatial distribution.

One Week Temperatures

After one week (168 hours), the temperatures drops again and adjust to the soil temperature (see Figure 5.18). The prevailing influence is due to global water temperature and initial water temperatures at individual nodes. The influence of the soil temperature is insignificant.

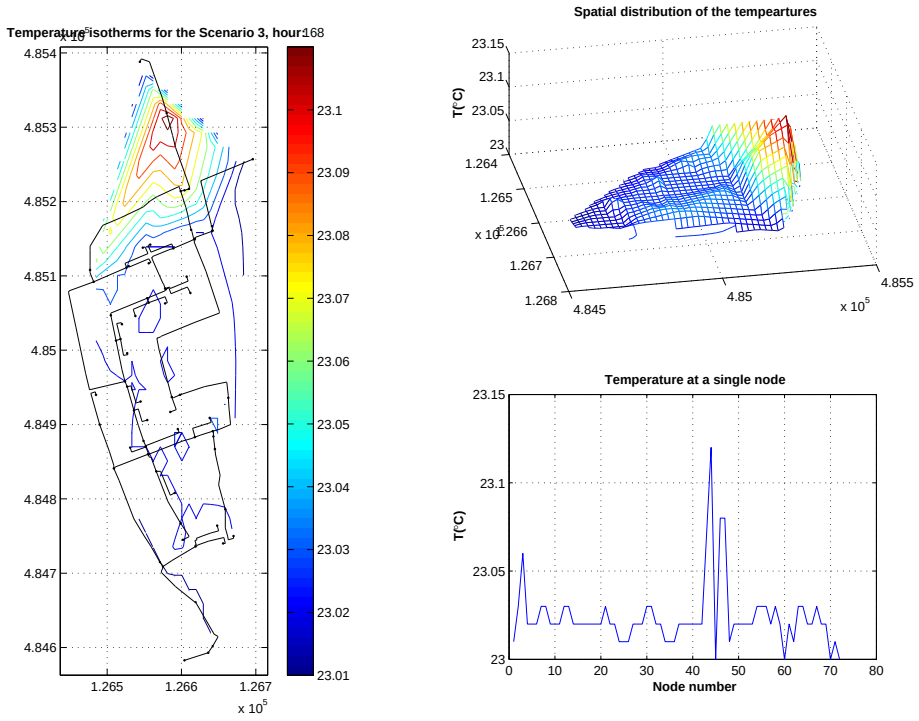

Figure 5.18: Temperature distribution in a network at 12 o'clock on a 7th day. Scenario 3. - The right side of a graph shows the temperature cloud travelling in a network (top) and the temperatures at individual nodes (bottom). The nodes temperatures are interpolated into isotherms and plotted on the network pipes. The water in fact is in the pipes. Isotherms intend to give a glimpse on the spatial distribution.

Table 5.8: Scenario three temperature settings.

Temperature	Soil	Incoming water	Network global water	Sampling locations
Set-point values	25°C	0, 9°C	20°C	+ 10°C

6

Discussion

There are few points that should be discussed before the final conclusions will be draw. In section 2 of chapter 3, we point out that the water incoming to the west part of Diemen Noord is already influenced by the soil temperature. Therefore, it can be questionable if the choice of sampling locations was correct. In section 7.1, we bring up results of the previous experiments to confirm that temperature in the network can still be altered although on the top of the soil influence. In section 7.2 we discuss why we have used the data from the synoptic meteorological station not the local one.

Finally, it can be pointed out that the heat extraction is not the sole solution to the drinking water temperature overheating. Some additional methods of overheating mitigation were naturally considered. A synthesis is given in section 7.3 and 7.4.

6.1 Observed Temperatures

In essence, measurements of temperature of the piped drinking water is complicated however necessary. The on-line temperature sensors indicate a mixture of a temperatures from the water incoming from a different sources thus may render irrelevant to networks studies as the temperature realisations inside pipes are governed by specific hydraulic conditions[1]. Therefore, contrasting measurements obtained at west part of Dimen Noord with previous studies can bring conflicting results.

[1] Additionally, those on-line temperature sensors are deployed at pumping stations or at the starting parts of the network while the problems occur at the periphery of a network.

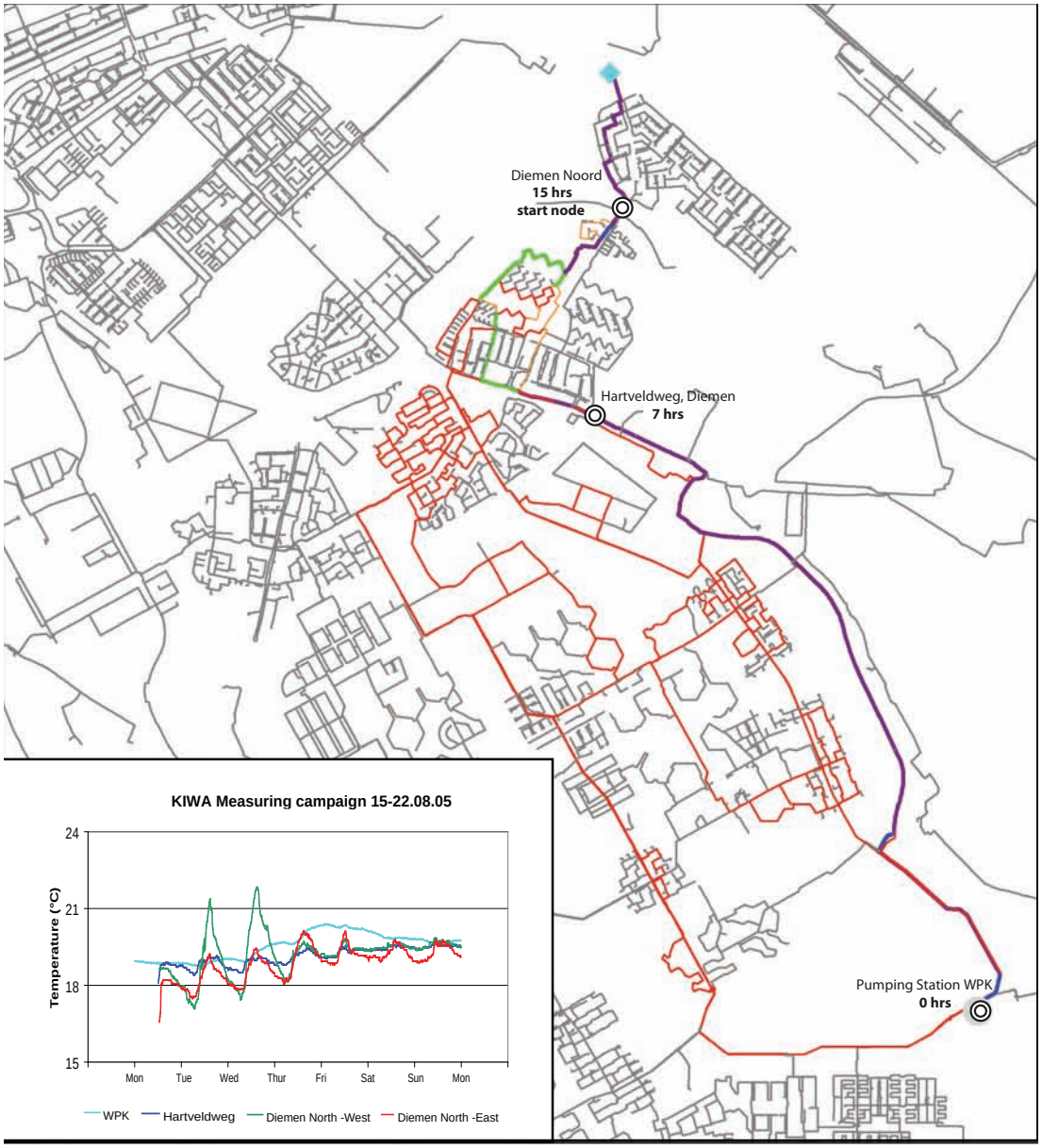

Figure 6.1: Temperatures registered at Waternet during the KWR research. - The research took place in summer 2005. The figure indicates the temperature difference registered at 4 sampling points and the estimated residence time of the water. From the figure it can be seen that the piped water measured in the pipe located at the North-West part of the Diemen (green line) has distinct peaks in the temperature time series. Those peaks are not visible in the temperature times series of the source water (light-blue line). According to hydraulic calculations, specifically backward tracing, which determines the routes of the water from the source to a tap-point, 15% of the total volume of water that leaves WPK treatment gets to west part of Diemen Noord.

In 2005, KWR has included west part of Diemen Noord in their quality-check research conducted at

the entire Waternet Network. Two important aspects have emerged from the KWR research: (i) 15 hours of time of travel from Weesperkarspel to west part of Diemen Noord, and (ii) the increasing temperature levels with a distance in the distribution (see also Figure A.7 in Appendix A.4). The research was done during summer. On average the water coming from Weesperkarspel was by 2°C higher at west part of Diemen Noord as can be seen in Figure 6.1. It is reasonable to believe that the differences in water temperatures registered at Diemen and at the treatment plant may be due to the atmospheric forcing; influence of the air temperature, wind convection and city heat storage. During experiment in west part of Diemen Noord we encountered opposite results. Its does not mean the measurements are conflicting what it means is that the atmospheric forcing plays an important role even in winter when colder atmospheric conditions (low net radiation and increased precipitation depth) prevail.

6.2 Source of the Atmospheric Input Data

The meteorological data, radiation, precipitation and the air temperatures for the purpose of this thesis, were taken from the nearest 240 KNMI synoptic station at Schiphol (see Figure 6.2).

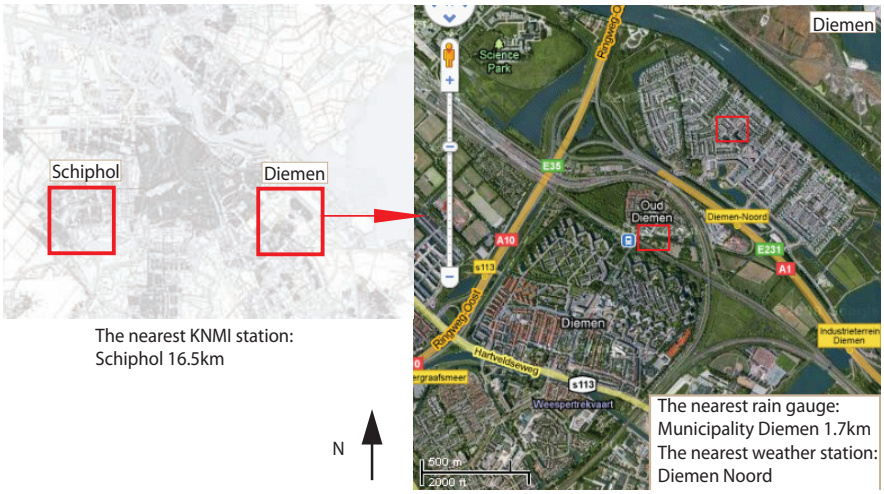

Figure 6.2: Weather stations nearby west part of Diemen Noord. - Schiphol is a synoptic station located the closest to west part of Diemen Noord. The local meteorological station is located at the North part of Diemen.

From the sensitivity analysis it is clear that the soil temperature depends strongly on the global radiation and air temperature. Those parameters may be altered urban heat island effect (Medrano, 2008). It seems preferable to have a local meteorological station to measure radiation and the temperature. However, during the course of this thesis, we have found out that the synoptic stations are more relevant

source of the meteorological data than a local meteorological station. The strong correlation between the global radiation observed at two adjacent synoptic stations of Bilt and Schiphol, ($R^2 = 0.94$) is lost if the same data are compared with global radiation obtained at the local meteorological station at west part of Diemen Noord, ($R^2 = 0.42$) (see Figure 6.3). This is probably due to the more stringent standards that the meteorological institutes impose on their measuring equipments and more precise guidelines on measuring set-up.

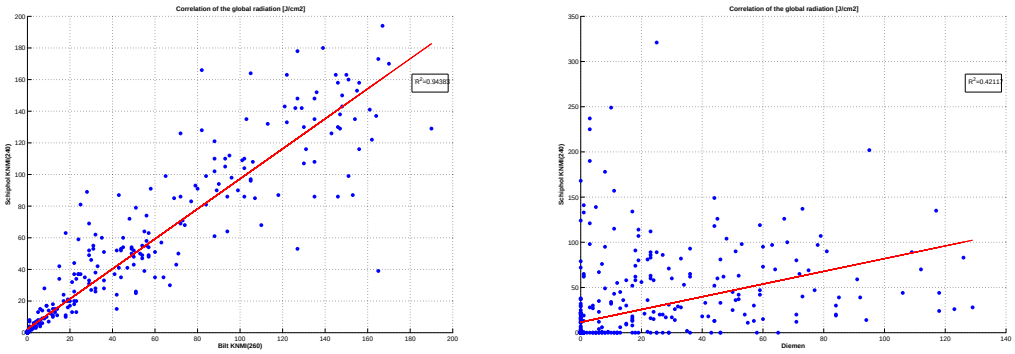

Figure 6.3: The measured global radiation at Dimen North-West has little correlation ($R^2 = 0.42$) with the values obtained from the synoptic stations.

6.3 Dealing with the Temperature Elevations

There is a number of different concepts of handling the drinking water temperature elevations. Three of them will be briefly discussed here: adjusting the treatment process, shielding the pipes directly exposed to solar radiation, and extracting excessive heat from the drinking water in the form of thermal energy.

6.3.1 Adjusting the Treatment Process

It should be pointed out that the overheating problem does not start neither ends in the distribution network level. First, as Waternet measurements show, the temperatures registered at the surface water extraction point: Loenderveen[1] at the level of *metalimnion* fluctuates around 2-25°C. Roughly, the optimal bacterial growth of *mesophiles* (e.g., *Legionella spp., Naegleria, Campylobacter.jejuni*) occurs in the temperature range of 20-30°C (Geldreich, 1996). A rise in the water temperature to 25°C may result in the drinking water susceptible to new opportunistic pathogens towards which the conventional

[1] See Appendix A.4.

treatment is not targeted (Van De Vossenberg et al., 2009). Second, according to quality controls at the randomly selected locations in Waternet network, the tap water temperatures are reportedly exceeding the $25^{\circ}\mathrm{C}$ threshold. It is difficult to asses, however, what is the origin of those temperature changes; the changes could be due to a faulty designed plumbing system.

The necessary adjustments to the water treatment process depend on the existing set-up at the treatment plant as well as on the space and funds available. Bouaziz (2009) investigated two possible scenarios: (i) upgrading the conventional treatment process with reverse osmosis and marble filtration and (ii) upgrading conventional treatment with UV combined with hydrogen peroxide dosage (UV/H2O2), activated carbon filtration and slow sand filtration.

The reverse osmosis method is expensive, requires a lot of water and energy and the waste produced during this treatment is difficult to dispose of. Nevertheless, this method creates a reliable barrier allowing removal of virtually all known microorganisms but the regrowth in the further parts of a network is still possible.

The UV / peroxide treatment does not remove microorganisms, but inactivates most of them. The slow sand filtration and activated carbon filtration are additionally necessary to remove the inactivated microorganisms and toxins.

Overall, the investment of the two scenarios amounts to approximately 1.5 billion euro for expanding a medium-sized treatment plant. Regardless the costs involved the chances are that the water in the further parts of the distribution will still deteriorate and the customers will be delivered water which is of inferior quality and hotter or colder as compared to the production site. This is not what the drinking water companies aim for.

6.3.2 Reducing the Direct Solar Radiation

The excessive heat in the soil ambient to the drinking water mains can be minimized by depleting the direct solar radiation by planting the shadow-creating shrubs, bushes and trees nearby the mains (Akbari et al., 2001). The vegetation, besides creating shadow, extracts energy in the form of transpiration and evaporation, which accounts for what is known in heat transfer theory as latent heat flux. More energy extracted by the plants means less heat channelled to the lower soil layers. Nevertheless, the concept renders expensive and possibly conflicting with the urban spatial plans.

6.3.3 The Potentialities for the Heat Extraction

Heat extraction or inclusion renders a fit to the purpose solution to the overheating problem. There are two concepts of employing heat extraction to alleviate temperature elevations: (i) extracting heat at the

extraction point and (ii) extracting heat from the piped water.

De Graaf and Van De Ven (2008) have investigated the technical and economic feasibility of an open water system, to supply thermal energy which would compensate the heat demand of a medium sized residential district. In the discussed project, surface water system, termed normally in similar studies ATES[1], was coupled with groundwater wells, where the thermal energy was stored (UTES[2]). As De Graaf and Van De Ven (2008) estimated and Medrano (2008) experimentally validated, the heat and cold wells combined with the aquifer are capable to cool down the surface water by 1.5-1.6°C in the summer period. It is equivocal whether it is feasible to regenerate the drinking water temperature by the same extend as the surface water.

In this thesis we were referring to the latter concept of extracting heat from the gradient between water conveyed in drinking water pipes and the soil enclosure. It was not possible to confirm the feasibility of it. The heat transfer coefficient found for the temperature gradients present during winter in the system was very low. It could not even light up a 60 Watt light bulb. However, the newest temperature time series obtained for the warmer days seem promising and perhaps a bigger heat exchange occurs during the summer days when the atmospheric influence is much bigger.

[1] Aquifer Thermal Energy Storage
[2] Underground Thermal Energy Storage

7

Conclusions and Recommendations

Drinking water temperature and temperature gradients are of utmost importance for temperature-associated chemical, micro-biological and hydrodynamic processes, still temperature variations within the network is an issue not yet accounted in most hydraulic calculations. In this thesis we try to find external parameters influencing the heat exchange between the atmosphere and a drinking water pipe, but we have focused on the hydraulics and its influence on the rate of the heat exchange between drinking water and the soil.

The study was based on previous investigations entailing the drinking water temperature and on the measurements collected during experiment in west part of Diemen Noord in a period between 9th of November 2009 - 23rd of April 2010.

7.1 Conclusions

Which parameters most strongly determine the heat exchange between a pipe and the atmosphere?

Drinking water temperature depends directly on the soil conditions and indirectly on the atmospheric changes. Because of that it covers a spectrum of processes, we have adopted a simplification, such as considering a vertical heat transfer towards the pipe separately from a horizontal heat flux due to transport of the bulk of water in a network. This way it was possible to account for external influences from each layer in vertical: air, soil and pipe.

Air layer The surface heat balance includes many empirical formulations and parameters for which models we have tested rendered insensitive. Namely, there was no sufficient evidence of the strong influence of the wind, moisture fluxes and the urban heat island effects on the thermal state of drinking

water pipes. While both the measurements and the models we have used confirmed a decisive role of the air temperature, precipitation and solar radiation on the drinking water temperature.

Soil layer It has been confirmed with measurements that soil layer introduces the largest thermal resistance and regulates the temperature of the water in pipes. The temperature at the pipe wall is nearly equal the soil temperature at the same depth, although an influence of the heat exchanges due to traversing water were also noticeable, it was rather inconsequential.

The validation of the soil model of Van Der Molen et al. (2008) yielded reasonably good results when it comes to predicting average temperature at the pipe depth. But the model could not correctly account for temperature differences between four sampling locations. The model did not also reflect the variability of the soil temperature but its predictions were persistent (root mean square error $1,5°\mathrm{C}$). The alternate diffusion model, which could represent oscillations of the temperature well, generated twice as big error (root mean square error $3,5°\mathrm{C}$). However, the imprecision of the alternate diffusion model could be eliminated with a better definition of the moisture processes relevant to the soil in the model (sensible and latent heat fluxes).

Groundwater In this thesis an influence of the groundwater has been confirmed with the principle component analysis. The groundwater is having a direct impact on the temperature at the pipe wall. This impact could be bigger than the soil due to a bigger heat capacity.

Synthesis The measurements confirmed a relevance of air temperature, net global radiation, precipitation and the characteristics of the soil to drinking water temperature predictions. However results from this case study demonstrated that the gradient between the soil, pipe wall and the drinking water temperatures was small. It was difficult to determine a clear influence of the hydraulic on the diurnal cycle of the drinking water-soil temperature exchange as according to soil temperature spectrum analysis the diurnal soil interventions did not reach the pipe depth during the experimental period.

How may cooling or heating of drinking water at one location influence the temperatures in the other parts of the drinking water supply network?

The drinking water incoming to a network will adjusts to the pipe wall temperature in an exponential manner. The spatial and temporal scales of this adjustment depends on the transport processes: velocity, viscosity and flow. In order to test how the water temperature will distribute in a network during the heat wave conditions or if we extract heat, it was necessary to lower the hydraulic error. The west part of the Diemen Noord supply network have been optimized according to the balance between measured total

water inflow and domestic and industrial demands. We validated how well the real temperature transport can be simulated in such adopted network. The maximum error at the validation point was $0,08°C$ (RMSE). The maximum network hydraulic modelling error, after calibration, was $1,3m^3/h$(RMSE).

Heat wave scenarios We have tested three possible scenarios of drinking water overheating at heat wave conditions. It occurred that two most influential parameters in the temperature transfer are a gradient between the incoming water and the soil temperatures and water residence time.

Initially, lowering the incoming water temperature yielded decrease in the temperature of the network water but after one day, due to the bigger gradient and bigger heat flux from the soil, the temperature exchange was accelerated and peaks in temperature of $25,5°C$ occurred. The highest temperatures occurred in small diameter pipes at the peripheral parts of a network which are most vulnerable to extraneous heat surges. Apparently, to prevent overheating it would be desirable to have the lowest residence time throughout the whole network; however with respect to drinking water network reliability this condition is not feasible to achieve.

Other Remarks

Finally, overheating and thermal condition of a drinking water in a network has no single cause. In this thesis we investigated the effects of the soil and atmospheric changes on the drinking water temperatures during cold conditions. But it was not feasible to identify unknown extraneous influences that have influenced temperatures measured at location 3.

7.2 Recommendations

The modelling of a pipe in a network is a logical next step to achieve a better understanding of how the heat exchange process evolve in a pipe. In our studies the bulk mean temperature has been calculated according to assumption that it will eventually reach the soil temperature and the length of the heat transition is estimated to be short. More measurements are needed to refute or confirm such assumptions.

In our studies it was proven that water temperatures are affected by a bigger urban energy cycle and therefore climatic elements should be regarded as important aspects in drinking water quality calculations, however, the significant gradients occur during summer. We were not able to prove the influence of the heat urban effect on the soil temperature while the sampling locations were chosen according to their specific urban morphology and surface albedo, so having a potential influence of the heat urban

effect in mind. Secondly, soil temperature diurnal fluctuations have a much bigger frequency and amplitudes during warmer seasons. Therefore, a similar tests should be repeated at Waternet during hot days to verify if the heat and moisture exchange alter at each individual location.

The hydraulic model used in this thesis was adjusted to winter conditions. Demands during summer are presumably much higher. If the demands are higher, there is also more turbulent flow which induces mixing temperatures of the water and pipe wall and cooling of the pipe walls. A follow-up research during summer days could thus yield interesting results.

Analytical models used in this thesis serve well in estimations of the drinking water temperatures. However, the two models remain uncoupled. Additionally, processes contributing to the drinking water temperature have different characteristic heating frequency. If we judge purely from measurements, the time scale relevant for the drinking water temperature calculations is a day or a week. Those scales are also most strongly determined in the system hydraulics. Therefore, a better modelling approach is necessary. Potentially, a partial differential model of the selected part of the system is required.

The soil has a different seasonal, diurnal and weekly heating and cooling frequencies. Those seasonal and week variations are still present at the pipe burial depth causing spatial discrepancies in temperatures. Their inclusion in the modelling is inevitable[1]. A better soil model which address the influence of precipitation and potential extraneous influences is recommended.

[1]The spatial variability can be accounted for by means of GIS analysis. The surface heat balance can be replaced by the infra-red images. The skin temperature obtained from the infra-red images can be used as a initial values for the soil model. Based on initial skin temperatures, a temperature distribution in the vertical can be calculated with a soil diffusion model. This information then can be used to classify the maps, which in turn can be contrasted with a drinking water distribution network. This task fell out of scope of this thesis due to the time frame constraints.

Appendix A

Appendices

A.1 Climate Change Scenarios

Table A.1: Four scenarios for climate change in the Netherlands in 2050 relative to 1990. Two driving forces were selected to construct the scenarios, the change in the atmospheric circulation pattern and the global temperature change. In the + scenarios there is a strong change in the atmospheric circulation pattern. In the other scenarios this change is weak. The G scenarios have a relatively small global temperature increase, the W scenarios have a higher global temperature increase (KNMI, 2006).

		G	G+	W	W+
Global temperature increase in 2050		+1°C	+1°C	+2°C	+2°C
Change of atmospheric circulation		Weak	Strong	Weak	Strong
Winter	Mean temperature	+0.9 °C	+1.1 °C	+1.8 °C	+2.3 °C
	Precipitation	4%	7%	7%	14%
Summer	Mean temperature	+0.9 °C	+1.4 °C	+1.7 °C	+2.8 °C
	Precipitation	3%	-10%	6%	-19%
	Potential Evaporation	3.40%	7.60%	6.80%	15.20%
	Daily cumulative precipitation (T=10 years)	13%	5%	27%	10%

A.2 Solar Intensity determination

The sun is located $1.5 \cdot 10^{11}$m from the earth and emits approximately as a black-body at 5800K, see Figure A.1.

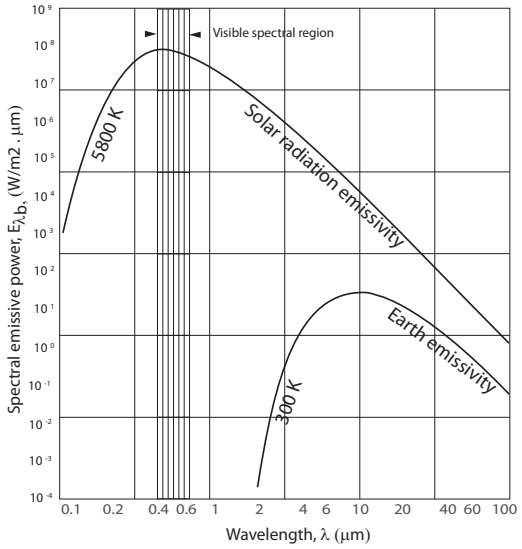

Figure A.1: Spectral black-body emissive power and solar emissive power - Sun emits approximately as a black-body.

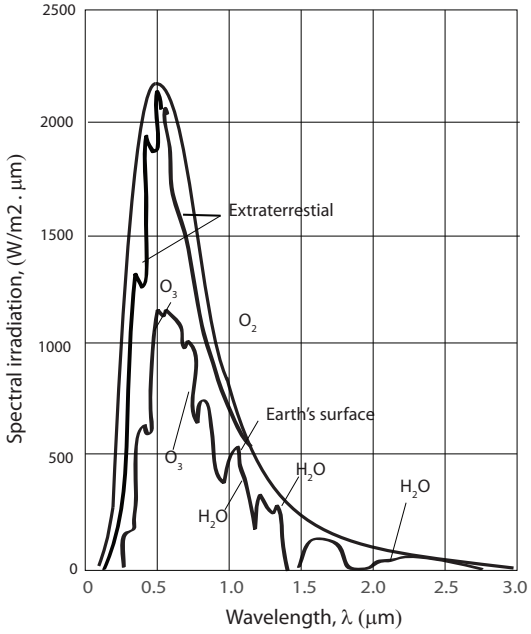

Figure A.2: Spectral distribution of solar radiation. -

A.3 Energy Budget

The first law of thermodynamics allows us to compute the variation of the water temperature and the amount of energy generated over the time interval during the passage of the bulk water. Let us consider a control volume as presented in Figure A.3.

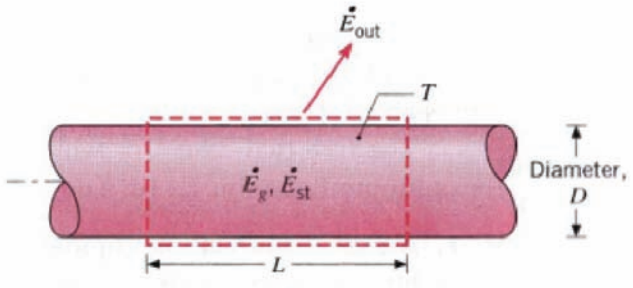

Figure A.3: Energy budget in a pipe. - Thermal and mechanical energy stored by material. The assumptions are that at any time interval the temperature of the pipe is uniform, pipe material has constant properties and conductive exchange between the outer surface of the pipe and the surrounding soil is between a small volume and a large enclosure. Adopted from (Incropera and De Wit, 2002).

Energy Generated in a Pipe

If the inflow and generation of thermal energy exceeds the outflow, there must be an increase in the amount of thermal and mechanical energy stored; if the opposite is true the energy is released. If the inflow and generation equal the outflow, a steady-state condition prevails and there will be no change in the energy stored in the control volume.

Figure A.3 illustrates relevant terms of heat transfer from the pipe towards the ambient soil and the resulting change in thermal energy storage of the pipe material. If bulk water passes there will be energy generation due to internal cooling/heating.

Energy Generated in a Stagnant Water

Let us assume that the temperature of the ambient soil is lower than the incoming water and the pipe wall temperatures. Using equation A.1 we can define the change over the interval of time when water resides in a pipe

$$E_g - E_{out} = \Delta E_{st} \tag{A.1}$$

Energy Generated in a Flowing Water

During the passage of a bulk of water the Equation A.2, which is equivalent to Equation A.6 we can estimate a rate of change in energy storage due to the bulk temperature change.

$$\dot{E}_g + \dot{E}_{in} - \dot{E}_{out} = \dot{E}_{st} \tag{A.2}$$

where $\dot{E}_{st}$is thermal energy generation, $\dot{E}_g$ is thermal and mechanical energy transport across the pipe volume. All terms are measured in joules. A dot indicates a rate.

Essentially, if drinking water enters a pipe at an uniform temperature which is lower then ambient soil then convective heat transfer occurs in direction towards the water (see Figure A.4). If we consider a control volume as prescribed in Figure A.4.

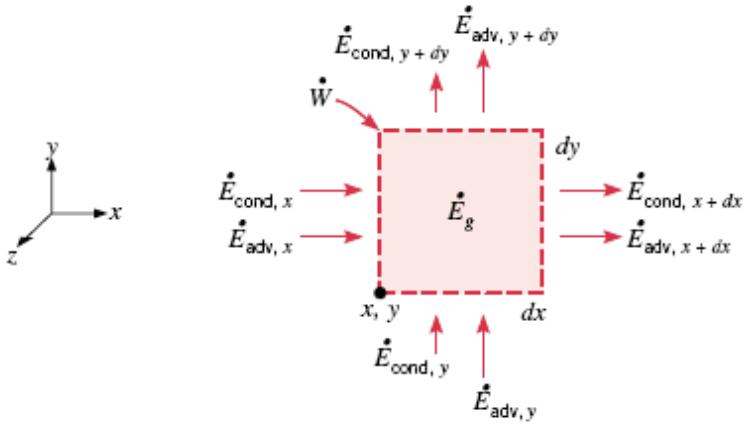

Figure A.4: Differential control volume in a viscous fluid with heat transfer. - Differential control volume ($dx \cdot dy \cdot 1$) for energy conservation in two–dimensional flow of a viscous fluid with heat transfer. Source: (Incropera and De Wit, 2002).

Then, the net rate at which water enters the control volume due to advection is:

$$\dot{E}_{adv,x} - \dot{E}_{adv,x+dx} = -\frac{\delta}{\delta x}\left[\rho u\left(e + \frac{V^2}{2}\right)\right] dxdy \tag{A.3}$$

where $\dot{E}_{adv}$is rate at which net energy enters the control volume, e and $\frac{V^2}{2}$ are thermal and potential energy advected with a bulk motion across the control surface, respectively.

For the conduction, the net transfer of energy into control volume is:

$$\dot{E}_{cond,x} - \dot{E}_{cond,x+dx} = -\frac{\delta}{\delta x}\left(k\frac{\delta T}{\delta x}\right) dxdy \tag{A.4}$$

where $\dot{E}_{adv}$is rate at which net energy enters the control volume, e and $\frac{V^2}{2}$ are thermal and potential energy advected with a bulk motion across the control surface, respectively.

The total energy advected in a tube relates to the difference in temperatures at the inlet and outlet. Water that resides long in a network pipe is in thermal equilibrium with the ambient soil. This equilibrium is disrupted as soon as a new bulk of water of a different temperature passes through.

The energy can be additionally added to the fluid in the control volume by work interaction due to the body and surface forces. The net rate at which work is done on the fluid by forces in the x-direction may be expressed as

$$\dot{W}_{net,x} = (Xu)\,dxdy + \frac{\delta}{\delta x}\left[(\sigma_{xx} - p)\,u\right]dxdy + \frac{\delta}{\delta y}\left(\tau_{yx}u\right)dxdy \tag{A.5}$$

where the first term on the right side represents the work done by the body force, and the remaining terms account for the net work done by the pressure and viscous forces.

The energy conservation requirement in the x-direction may be expressed as

$$\rho c_p\left(u\frac{\delta T}{\delta x} + v\frac{\delta T}{\delta y}\right) = \frac{\delta}{\delta x}\left(k\frac{\delta T}{\delta x}\right) + \frac{\delta}{\delta y}\left(k\frac{\delta T}{\delta y}\right) + \left(u\frac{\delta p}{\delta x} + v\frac{\delta p}{\delta y}\right) + \mu\Phi + \dot{q} \tag{A.6}$$

were $\dot{q}$ is a rate at which thermal energy is generated per unit volume, p represents a reversible conversion between mechanical work and thermal energy and $\mu\Phi$, the viscous dissipation, defined as

$$\mu\Phi = \mu\left\{\left(\frac{\delta u}{\delta y} + \frac{\delta v}{\delta x}\right)^2 + \left[\left(\frac{\delta u}{\delta x}\right)^2 + \left(\frac{\delta v}{\delta y}\right)^2\right]\right\} \tag{A.7}$$

Determining Boundary Conditions

To solve the heat equation A.6, physical conditions existing at the boundaries of the medium need to be determined. Since the heat equation is in second order in spatial coordinates, it needs two boundary conditions for each coordinate. Additionally, if the physical conditions existing at the boundaries of the medium are time dependent, then one initial condition is needed, as the heat equation is first order in time. This is difficult to obtain therefore simplifications and specific conditions prescription are ubiquitous. A convenient alternative is assuming a one dimensional heat flux and fully developed temperature profile.

A.4 Waternet Extraction Water

The drinking water of Waternet is extracted from two sources: the dune area 'Amsterdamse Waterleidingduinen' at Leiduin and from the Bethunepolder near Loosdrecht (See Figure A.5).

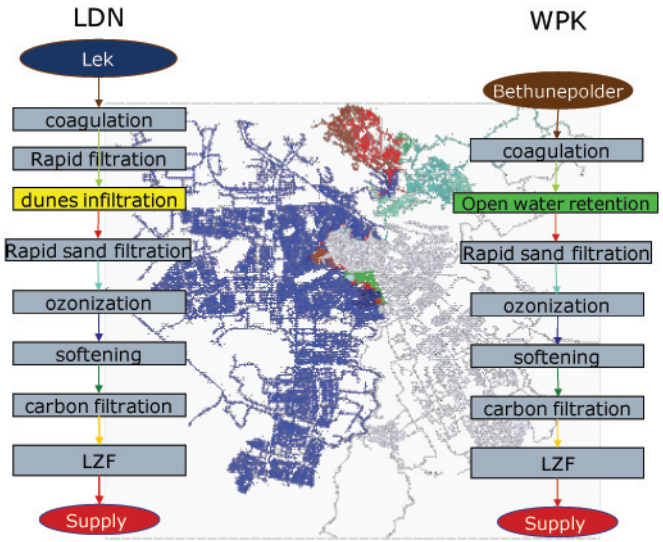

Figure A.5: Comparison of the treatment processes of two types of Waternet water - Comparison of the treatment processes of two types of Waternet water. In the middle a mixing zones are visible. Blue part is a distrubution from Leiduin, white part from the Weesperkarspel. Source:M.Dignum (2008)

The two water have slightly different pre-treatment processes, whereas the post-treatment is almost the same, as shown in Figure A.5. At Leiduin, Rhine water is infiltrated and treated in different steps (coagulation, rapid filtration, dune infiltration, rapid filtration, ozonation, softening, activated carbon filtration).

The water post-treatment is similar to the one at Leiduin and takes place at the treatment plant Weesperkarslpel. The disinfected drinking water is distributed to more than a million clients (households and industries of Amsterdam) in a network with a total length of about 2000 kilometres.

A.4.1 Microbial Stability

As has been researched the two types of water have a different quality, see Figure **??**. The water from the Bethunepolder, treated at Weesperkarspel exhibit lower microbial stability, see Figure A.7. This situation may be related to the high temperature occurrence in the WPK part of the network, Figure A.6.

Figure A.8 illustrates the average temperature difference between regular distribution measuring points and finished water at Weesperkarspel in summer and winter period. In winter, all locations show

higher temperatures relative to the production location, independent of the residence time. In summer, most locations show lower temperatures relative to the production location, except for a few locations with increased temperature. These are: (26) Sniep 28, Diemen; (136) Griend 1-17, Diemen; (149) Gruttoplein 5, Diemen; (139) Pampusweg 26, Muiden; (64) Googweg 9a, Muiderberg. Dependence on residence time is not significant. Source:M.Dignum (2008).

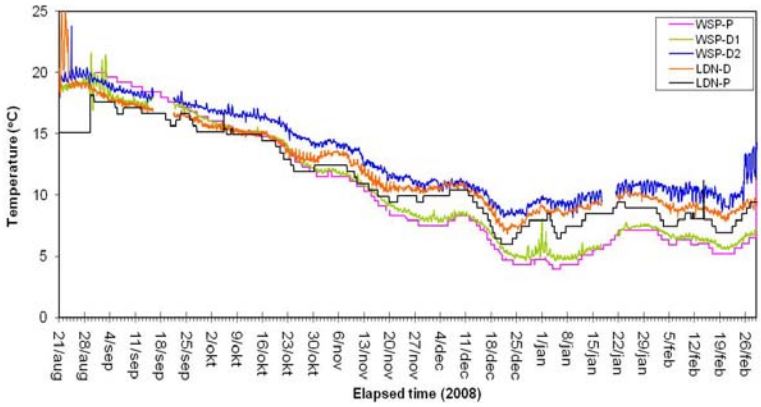

Figure A.6: Temperatures measured during the bio-film monitoring campaign August'08-February'09. Source: M.Dignum(2008). - The temperature values measured along the distribution network (D)during the campaign were compared with the temperatures registered on-line (P) at the same time on the production sites: Leiduin (LD) and Weesperkarspel (WPK).

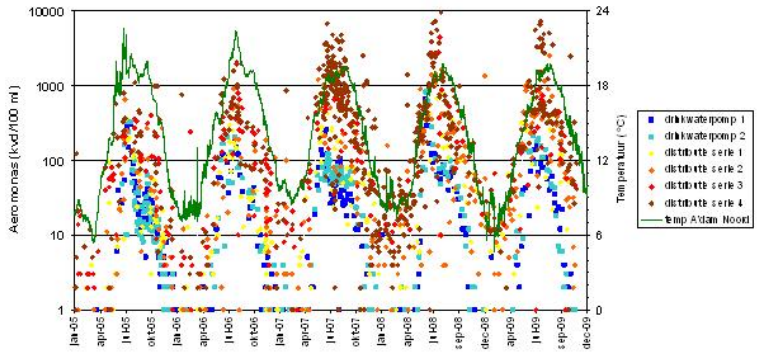

Figure A.7: Correlation between the Aeromonas counts and temperature. - Aeromonas counts at drinking water production station Weesperkarspel and in the distribution network plotted with temperature in Amsterdam North.

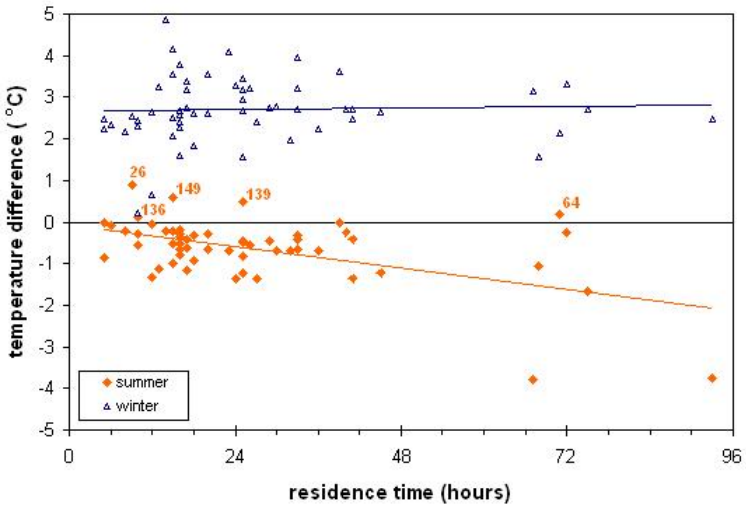

Figure A.8: Average temperature difference between regular distribution measuring points and exit water at Weesperkarspel - Average temperature difference between regular distribution measuring points and finished water at Weesperkarspel in summer and winter period. In winter, all locations show higher temperatures relative to the production location, independent of the residence time. In summer, most locations show lower temperatures relative to the production location, except for a few locations with increased temperature. These are: (26) Sniep 28, Diemen; (136) Griend 1-17, Diemen; (149) Gruttoplein 5, Diemen; (139) Pampusweg 26, Muiden; (64) Googweg 9a, Muiderberg. Dependence on residence time is not significant. Source:M.Dignum (2008).

A.5 Factors Altering Urban Climates

The urbanization alters the natural surface and atmospheric conditions. Cities no matter what their size tend to be warmer than their surroundings. On the broader more rural surrounding land cities produce a heat-island effect on the spatial temperature distribution in an area. The apparent city influence ranges from micro- (e.g. replacing trees with parking lot) to macro-scale (e.g. carbon dioxide effects on global climate by fossil fuel combustion and emission)(see Figure 6). Table A.2 list the aspects that are responsible for the climate alternations.

City size, morphology, land-use configuration, and geographic setting (e.g. relief, elevation, regional climate) dictate the intensity of the heat island, its geographic extent, orientation, and its persistence through time.

The distinct urban forms and their ability of a to have an impact on the local climate have been classified in WMO (2008). This classification give an initial estimation of how the underlying energy, moisture and air movement patterns will be changed in a specific urban structure.

Table A.2: Mechanisms hypothesized to cause the urban heat island effect. Source: Oke, (1997)

Urban Boundary Layer
Anthropogenic heat from roofs and stacks
Entrainment of air scoured from warmer canopy layer
Entrainment of heat from overlying stable air by the process of penetrative convection
Short-wave radiative flux convergence within polluted air
Urban Canopy Layer
Anthropogenic heat from building sides
Greater short-wave absorption due to canyon geometry
Decreased net long-wave loss due to reduction of sky view factor by canyon geometry
Greater daytime heat storage (and nocturnal release) due to thermal properties of building materials
Greater sensible heat flux due to decreased evaporation resulting from removal of vegetation and surface waterproofing
Convergence of sensible heat due to reduction of wind speed in the canopy

Table A.3: Urban climate effects for a mid-latitude city with about 1 million inhabitants (values from summer). Source: Oke (1997)

Variable	Change	Magnitude/comments
Turbulence intensity	Greater	1050%
Wind speed	Decreased	530% at 10 m in strong flow
	Increased	In weak flow with heat island
Wind direction	Altered	110 degrees
UV radiation	Much less	2590%
Solar radiation	Less	125%
Infra-red input	Greater	540%
Visibility	Reduced	
Evaporation	Less	About 50%
Convective heat flux	Greater	About 50%
Heat storage	Greater	About 200%
Air temperature	Warmer	13C per 100 years; 13C annual mean up to 12C hourly mean
Humidity	Drier	Summer daytime
	More moist	Summer night, all day winter
Cloud	More haze	In and downwind of city
	More cloud	Especially in lee of city
Fog	More or less	Depends on aerosol and surroundings
Precipitation		
Snow	Less	Some turns to rain
Total	More?	To the lee of rather than in city
Thunderstorms	More	
Tornadoes	Less	

TABLE 11.1. Simplified classification of distinct urban forms arranged in approximate decreasing order of their ability to have an impact on local climate (Oke, 2004 unpublished)

Urban climate zone [a]	*Image*	*Roughness class*[b]	*Aspect ratio*[c]	*% built (impermeable)*[d]
1. Intensely developed urban with detached close-set high-rise buildings with cladding, e.g. downtown towers	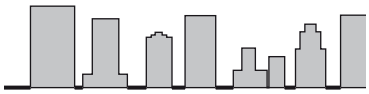	8	> 2	> 90%
2. Intensely high density urban with 2–5 storey, attached or very-close set buildings often of bricks or stone, e.g. old city core		7	1.0–2.5	> 85
3. Highly developed, medium density urban with row or detached but close-set houses, stores and apartments, e.g. urban housing		7	0.5–1.5	70-85
4. Highly developed, low or medium density urban with large low buildings and paved parking, e.g. shopping malls, warehouses		5	0.05–0.2	70-95
5. Medium development, low density suburban with 1 or 2 storey houses, e.g. suburban houses		6	0.2–0.6, p to > 1 with trees	35-65
6. Mixed use with large buildings in open landscape, e.g. institutions such as hospitals, universities, airports		5	0.1–0.5, depends on trees	< 40
7. Semi-rural development, scattered houses in natural or agricultural areas, e.g. farms, estates	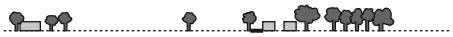	4	> 0.05, depends on trees	< 10

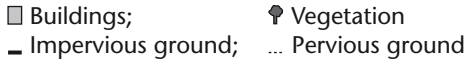

a A simplified set of classes that includes aspects of the schemes of Auer (1978) and Ellesfen (1990/91) plus physical measures relating to wind, and thermal and moisture control (columns on the right). Approximate correspondence between UCZ and Ellefsen's urban terrain zones is: 1 (Dc1, Dc8), 2 (A1–A4, Dc2), 3 (A5, Dc3–5, Do2), 4 (Do1, Do4, Do5), 5 (Do3), 6 (Do6), 7 (none).

b Effective terrain roughness according to the Davenport classification (Davenport and others, 2000); see Table 11.2.

c Aspect ratio = Z_h/W is the average height of the main roughness elements (buildings, trees) divided by their average spacing; in the city centre this is the street canyon height/width. This measurement is known to be related to flow regime types (Oke, 1987) and thermal controls (solar shading and longwave screening) Oke 1981. Tall trees increase this measure significantly.

d Average proportion of ground plan covered by built features (buildings, roads and paved and other impervious areas); the rest of the area is occupied by pervious cover (green space, water and other natural surfaces). Permeability affects the moisture status of the ground and hence humidification and evaporative cooling potential.

A.6 Data Statistics

A.6.0.1 De-trending the Data

It is apparent that the parameter fitting and confidence intervals are bigger for data without trend. There are two methods considered, that remove the trend from the sensor data: the linear regression and the robust linear regression. In both methods, the simple linear and the robust regression, a response variable y is modelled as a combination of constant

$$R = \beta_(1) \cdot f_(1)(x) + ... + \beta_(p) \cdot f_(p)(x) + \epsilon$$

, linear, interaction and quadratic terms formed from two predictor variables x1 and x2. Uncontrolled factors and experimental errors are modelled by ϵ. Given data on $x_(1)$, $x_(2)$ and y, regression estimates the model parameters $\beta_(j)$(j=1,...,p).

Simple, linear regression is based on certain assumptions, the most important of which, is that the errors in the observed response, have a normal distribution. In our case, it is unknown a priori as there are outliers and discontinuities in the signal, that comes from the disruption to the measuring equipment, thus it is possible that the distribution of the errors is asymmetric.

Hence, a suitable fitting method, would be the one that is less sensitive than ordinary least squares to large changes in small parts of the data. In the robust regression outliers have small robust weight, as a consequence, they do not exert a large influence on the fit and are effectively excluded from the robust fit. The method firstly iteratively assign a weight to each data point and compute the model coefficients by the weighted least squares.

A.6.1 Principle Component Analysis

Principle Component Analysis aims at depicting driving variables that govern the behaviour of the system, as depicted in the sketch A.9. It is a method for data reduction that searches for a pattern in the correlations between a large group of observed variables and summarizes a large group of observed variables in a small group of factors that explain the system biggest variability.

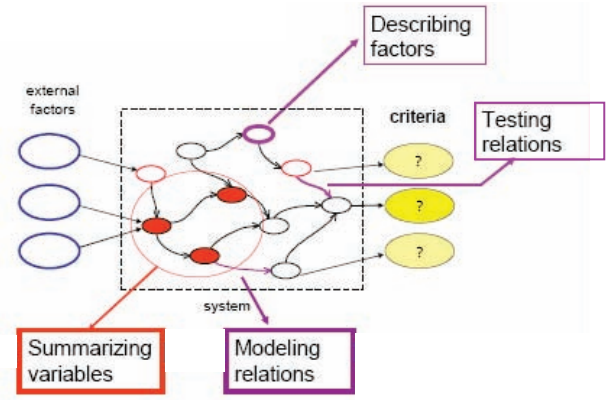

Figure A.9: Principal Component Analysis Method for Reduction of Parameters. - The scheme exemplifies the method of testing relations and simplifying the model by reducing parameters to the most significant to the system performance.

The determinants of the relevant parameters are component coefficients and variances. The components coefficients are linear combination of the original variables, also known as loadings. The time series from the measurements are standardized and used to create a correlation matrix. The largest component coefficients are the principal coefficients. The component variances are vectors containing the variance explained by the principal component.

By definition the mathematical solution to the variance factors, F is:

$$F_1 = \nu_{11}X_1 + \nu_{12}X_2 = \nu_1^T X$$

$$F_2 = \nu_{21}X_1 + \nu_{22}X_2 = \nu_2^T X$$

where each factor is defined by slope ν and vector X (the input variables. Variance of the factor is $var(F_1) = \nu_1^T R \nu_1$. By definition the maximum variance is when: $(R - \lambda I)\nu_1 = 0 \Leftrightarrow |R - \lambda I| = 0$. Thus the two principal components are two systems' Eigenvalues and the vectors are systems Eigenvectors. The final outcome of the analysis is the biplot of principal components distribution, with indication of the variance vectors, the length of which indicated how much a singular component contribute to the principle one.

A.6.2 Correlation Analysis

The scatter correlation plots represent temperature pairs at different location. The horizontal axis represents independent variable and vertical dependent. The graphs shows association of the pair of

the population of variables and its dependency is signified by the McFadden's correlation coefficient, $R^2 = 1 - \frac{ln(dependent)}{ln(independent)}$. The bigger the coefficient the better the correlation.

A.7 Experiment Preparation

A.7.1 Instrumentation

NTC Thermistors

Temperature of soil and drinking water were measured with the NTC 100k Ohm sensors[1]. NTC (Negative Temperature Coefficient) Thermistors are semiconductor resistors in which resistance decreases with increasing temperature. Due to low thermal time constants the thermal resistance changes at an extremely high rate. The accuracy of the NTC thermistor deployed at the Diemen[2] experiment is $\pm 0.2°$C and the nominal resistance of 100 Ω at 0°C. Further in the text we will refer to those instruments NTC 100k Ohm or simply NTC thermistor.

Using a linear relationship between resistance and temperature, the measured resistances can be converted into temperature readings by using Equation A.8, called the Steinhart-Hart equation. In Equation A.8, T is the temperature (in Kelvin) and R is the resistance at T (in Ohms). The values of the constants A, B and C were given by the characteristic NTC curve of the sensor used for this project which can be found at the producers website[3].

$$\frac{1}{T} = A + B\ln(R) + C(\ln(R))^3 \tag{A.8}$$

Due to the large coefficients of resistance, which eliminates the consideration of the resistance of the leads and its changes, elements can be made very small. The deployed sensors were $6\mathrm{mm}$ in diameter and $70\mathrm{mm}$ in length. The NTC thermistor is located at the round end of the aluminium tube and the tube is filled with Bison Kombi, a two-component epoxy glue. A set of 5 sensors was then connected to the data logger (see Figure A.10).

[1] Commercial name: NTC Honeywell Sensor 192-104QET-A01
[2] Manufacturer:Ellitrack
[3] NTC characteristic curve$content.honeywell.com$.

(a) NTC Sensor.

(b) NTC sensor in an aluminium housing (the end of the orange cables).

(c) interior of the data logger.

Figure A.10: Ellitrack temperature sensor system deployed at the experiment in west part of Diemen Noord.

Every ten seconds, the resistance of every of the five connected sensors is measured and the values are converted into corresponding temperatures. Every ten minutes, the minimum, maximum and mean of every sensor is calculated and the values are stored on the registration-cache of the data logger and the measurement-cache is emptied. Every four hours, the registrations (i.e., the minimum, maximum and mean of the ten minute intervals) are sent to the sensor network server via GSM/GPRS and the registration-cache is emptied.

Vented Transducers

Vented transducers commonly known as groundwater divers were installed at a number of piezemeters in order to register the groundwater levels and temperatures. In specific, Mini Diver electrical pressure vented transducers were used (see Figure A.11). The characteristics of the Mini Diver are given in Table A.4.

The Mini-Diver contain electronics consisting of two main components: the force summing device, with respect to the pressure (caused by the water head above the device), and the sensor which converts the output of the force summing device into an electrical signal. Water pressure and hence level is measured with respect to atmospheric pressure. Diver simultaneously registers the date and time, groundwater level and temperature.

Figure A.11: A picture of Mini-Diver; a groundwater temperature and pressure measuring device. - Source: Manufacturer's website. Schlumberger, www.swstechnology.com.

Table A.4: Characteristic of Mini-Diver; a groundwater temperature and pressure measuring device.

Characteristics	Unit	Value
Range	°C	-20 to 80
Min. sample interval	s	0.5
Max. sample interval	h	80
Accuracy	°C	0.1
Resolution	°C	0.01

The water meters deployed at a number of representative households were continuously measuring the specific demands and weekly and daily patterns during the period from 15th of October 2009 till 6th of December 2009. To this end, Actaris Flodis residential jet single jet velocity, turbine type water meters were used (see Figure A.12). The instruments' characteristics are given in Table A.5.

(a) Actaris Flodis water meter with a data logger installed on the top.

(b) Top view of an Actaris Flodis water meter.

Figure A.12: A picture of Actaris Flodis; a domestic water flow meter.

Table A.5: Characteristic of Actaris Flodis water meter. Source: Manufacturer's website. Itron, www.actaris.com.

Characteristics	Unit	Value
Indication range	m^3	99999.99
Minimum scale interval	l	0.05
Typical starting flow rate	l/h	5
Accuracy $\pm 5\%$	l/h	4
Accuracy $\pm 2\%$	l/h	8
Maximum accidental operating temperature	°C	50 (<1(h/day))

A.7.2 NTC Installation

The procedure of installing the sensor S1 and S2 in the pipe and on the pipe wall was as follows:

(i) pavement disposal and excavation to the top of the pipe (see Figure 3.8), (ii) drainage with wells and removal of the top soil layer from the pipe (see Figure 3.8), (iii) locking the adjacent hydrants, (iv) mounting the pipe clamp, into which the sensor (S1) tube can be inserted (see Figure A.13), (v) drilling into the pipe, letting the water drain from the pipe, (vi) mounting the sensor S1 into the insertion tube (see Figure A.13), (vii) installing the insertion tube inside the pipe split ring (see Figure A.15), (viii) fixing the insertion tube on the pipe and insulating the top of the tube with Polythyleen PE and silicon to prevent heat conduction from the soil to the sensor (see Figure A.15), (ix) fasten the tube with the PE cover and strings (see Figure A.15), (x) fasten the sensor S2 on the pipe wall with plastic strings (see Figure A.15).

(a) PVC pipe split ring with opening for the sensor tube.

(b) The PVC pipe split ring is installed on the pipe.

(c) Sensor S1 insertion tube.

Figure A.13: PVC pipe split ring with opening for the sensor tube.

(a) Example of the metal split ring.

(b) Drilling through the pipe.

(c) A remaining piece of PVC from the drilling of the pipe.

Figure A.14: Boring the opening for a sensor S1.

(a) Insulating the top of the tube to prevent heat conduction from the soil to the sensor.

(b) Fasten the tube with the PE cover and strings.

(c) Fasten the sensor S2 on the pipe wall with plastic strings.

Figure A.15: Insulating the top of the sensor's S1 tube.

In Figure 3.8 it can be seen that the sensors mounted in the soil are applied in the undisturbed soil. After sensors S1 and S2 are mounted in a pipe, the excavation is filled with a soil layer until the depth of the first intermediate level, where sensor S4 is installed. At this point, the data logger is covered with an empty gully pot and the excavation is filled again with the next soil layer. Lastly, sensor S5 is mounted near the surface, at around $5\mathrm{cm}$ depth. Thereafter, the last soil layer is placed and the soil in the excavation is mechanically compacted (for about 10 min) (see Figure A.17).

(a) S1 is mounted near the surface.

(b) The data logger is covered with an empty gully pot.

(c) The excavation is filled with the soil layer.

Figure A.16: Earth works at location 2.

(a) The the excavation is filled with another soil layer.

(b) The location 2 after the reconstruction.

Figure A.17: Earth works at location 2.

The only diversion from the procedure was done when equipment was installed at location 4 (see Figure A.18 and Figure A.19). At this site, a high groundwater table occurred. It was decided to monitor the groundwater temperature with the NTC equipment instead in order to obtain a comparison between the measurements obtained from the Mini-Divers in the piezometers and the groundwater temperature as measured near the pipe will be possible.

In addition, under the pavement at location 4 there is a concrete slab of $40\mathrm{cm}$. For this reason, sensor S4 was placed in the grass and sensor S5 just under the concrete slab. Figure 3.8 and Table 3.9 list changes to the standard set-up.

(a) Mounting sensor S1.

(b) Mounting sensor S2 in the groundwater, under the pipe.

(c) Mounting sensor S3 at the top pipe wall and below the concrete slab.

Figure A.18: Sensors set-up at the pipe at location 4.

(a) Mounting sensor S3 at the top pipe wall and below the concrete slab.

(b) The concrete slab above the equipment.

(c) Deploying the sensor S4 in the grass.

Figure A.19: Sensors set-up in the soil at location 4.

A.8 Time Series Spectrum Analysis

The computational basis of spectral analysis is Fourier Transform (FT), which translate time based data into the frequency-based information. The FT transforms the data vector x of a length n into vector y of length n by the use of the component ω, which is called complex nth root of unity. The transform basic equations is as follows

$$y_{p+1} = \sum_{j=0}^{n-1} \omega^{jp} x_{j+1} \tag{A.9}$$

where:

$$omega = e^{-2\pi i n^{-1}} \tag{A.10}$$

Data in the vector x, is the data obtained from the sensors. Data points in this vector are spaced-apart

by a constant interval in time, dt=1/fs, where fs is the sampling frequency of 10 minutes. The output signal y, is complex-valued. The absolute value of the output at the index 1+p measures the amount of frequency f=p(fs/n) present in data.

A.9 Soil Model Sensitivity Analysis

Before we use the soil model at Waternet conditions we performed a sensitivity analysis. The sensitivity analysis directed at the soil model parameters reduction, was based on the modelled temperatures time series at the 0.75m depth and temperatures measured at the same depth during the experiment in Breda. The reference data was the output of the model. However, the training data set was very closely correlated with measurements; so closely that it deviated not more than 5% from the measurements. This reference temperature time series were used further in the statistical analysis.

The default soil thermal properties were based on the data measured on site and reported in (Van Der Molen et al., 2008). Those soil properties correlate well with the characteristics of the dry sand (Oke, 1997). The default regional albedo value was also taken from the measured data and correlates well with the albedo of a bare soil (Oke, 1997).

The meteorological data were obtained from the portable meteorological station deployed during the Breda experiment at a standard screen level (1.5m). These data were used to calculate the solar radiation balance, heat fluxes and temperatures at different soil layers.

Analysis Procedure

The model sensitivity test was conducted as follows: (i) the best fitted simulation was defined and the resulting parameters were taken as a reference values, (ii) a single model input (or related set of model inputs) is varied from the reference case, while holding all other inputs constant, (iii) the simulated values are subjected to the same statistical analysis as used in (Arnfeld and Grimmond, 1997). The tests main objective is to evaluate to which degree the temperature at the burial depth depends on the manipulated variable(or set of variables).

Sensitivity Indices

The sensitivity analysis is based on three main indices Nash Sutcliffe (N&S), Root Mean Square Error (RMSE) and Root Mean Square Error Biased (RMSEB). N&S parameter gives an indication of fit between the time series of the reference and changed situation. RMSE is unbiased indicator of aggregate root mean square error between the predicted and modelled values. RMSEB is a biased indicator. We

consider the model sensitive to the parameter if a small change in the parameter value rises the reference RMSE by more than +/- 5% or upsets the N&S coefficent. The test is done by increasing or decreasing the parameters values by 50% and verifying the percentage of the output error.

Table A.6: The soil model sensitivity to changes in the atmospheric values[1]. .

		Model	Change	Value	Unit	RMSE*	RMSEB**	NS***
transition layer	z_0	0.15	133%	0.2	m	0.06	0.06	0.02
			53%	0.08	m	0.00	0.00	0.00
roughness layer	h_{RL}	10	50%	5	m	0.23	0.23	0.08
			150%	15	m	0.00	0.00	0.00
conduction resistance	R_g	30	5%	32	-	0.02	0.02	0.01
			50%	15	-	0.37	0.37	0.15
			150%	45	-	0.35	0.35	0.14
global radiation	$K\downarrow$	154.7	131%	203.3	$\mathrm{W/m^2}$	1.01	1.01	0.52
			108%	166.5	$\mathrm{W/m^2}$	0.42	0.42	0.21
wind speed	u	1.8	208%	3.75	$\mathrm{m/s}$	0.37	0.37	0.15
air temperature	T_∞	288.88	100.7%	290.83	K	0.67	0.67	0.41
			97.1%	280.38	K	7.28	7.28	0.99

A summary of the outputs of the soil model sensitivity analysis. The ranges of the parameters values are taken from the: (Blokker and Pieterse-Quirijns, 2009) and (De Graaf and Van De Ven, 2008). The change column indicates the percentage of the parameters' value change as compared to the reference value of the same parameter. NS*** parameter gives an indication how well the time series of the reference and changed situation fit. RMSE* is unbiased indication, a root mean square error between the predicted and modelled values. RMSEB** is a biased indicator measured in the same units as the variable it refers to.

Table A.7: The soil model sensitivity to changes in the albedo values [1].

	Surface	Value	RMSE*	NS***
Albedo	Model	0.16		
	Asphalt	0.05	0.27	0.10
		0.2	0.02	0.01
	Concrete	0.1	0.11	0.04
		0.35	0.53	0.22
	Dry soil	0.4	0.72	0.31
	Short grass	0.26	0.19	0.06

The soil model sensitivity to changes in the albedo values. The albedo values taken from Oke (1981) are the most common surfaces that occur in a city. The table is a summary of the outputs of the sensitivity analysis runs with the indication of the magnitude of change (change) in the parameter value as compared to the reference value of the same parameter (model). NS*** parameter gives an indication how well the time series of the reference and changed situation fit. RMSE* is unbiased indication, a root mean square error between the predicted and modelled values. RMSEB** is a biased indicator measured in the same units as the variable it refers to.

Table A.8: The soil model sensitivity to changes in the soil thermal values. [2]

Subsurface	ρ	c	k	RMSE*	NS***
	$\mathrm{kg/m^3}$	$\mathrm{J/kg\ K}$	$\mathrm{W/m\ K}$		
Model	1.6	1.06	2.03		
Dry soil clay	1.6	1.42	0.25	0.71	0.47
Dry soil sand	1.4	0.83	0.15	0.96	0.78
Moistured soil sand (w=0.12)	1.7	1.3	0.25	1.02	0.83
Saturated soil sand (w=0.25)	2.08	1.67	2	0.19	0.07
Apshalt	2.11	1.94	0.75	0.84	0.62
Dense concrete slab	2.4	2.11	1.51	0.77	0.48

The soil model sensitivity to changes in the soil thermal values. The table is a summary of the outputs of the sensitivity analysis runs with the indication of the magnitude of change (change) in the parameter value as compared to the reference value of the same parameter (model). NS*** parameter gives an indication how well the time series of the reference and changed situation fit. RMSE* is unbiased indication, a root mean square error between the predicted and modelled values (has the same units as listed in a first row.

Table A.9: Observed and modelled temperature time series (before and after the trend removal).

	Observed Location 1		Modelled Location 1		Observed Location 2		Modelled Location 2	
	original	cleaned	original	cleaned	original	cleaned	original	cleaned
mean	9.47	0.00	10.30	0.00	9.12	0.00	10.45	0.00
std	0.93	0.67	0.74	0.69	1.12	0.89	0.74	0.69
min	7.36	-1.26	8.66	-1.22	6.29	-1.93	8.78	-1.22
max	10.70	1.30	11.24	1.04	10.75	1.70	11.39	1.04
	Observed Location 3		Modelled Location 3		Observed Location 4		Modelled Location 4	
	original	cleaned	original	cleaned	original	cleaned	original	cleaned
mean	9.73	0.00	10.45	0.00	8.98	0.00	10.35	0.00
std	1.11	0.88	0.74	0.69	1.37	1.15	0.74	0.70
min	7.18	-1.66	8.79	-1.22	5.52	-2.50	8.71	-1.22
max	11.37	1.72	11.40	1.04	11.31	2.31	11.29	1.04

A.10 Residuals of modelling

A.11 Correlation plots

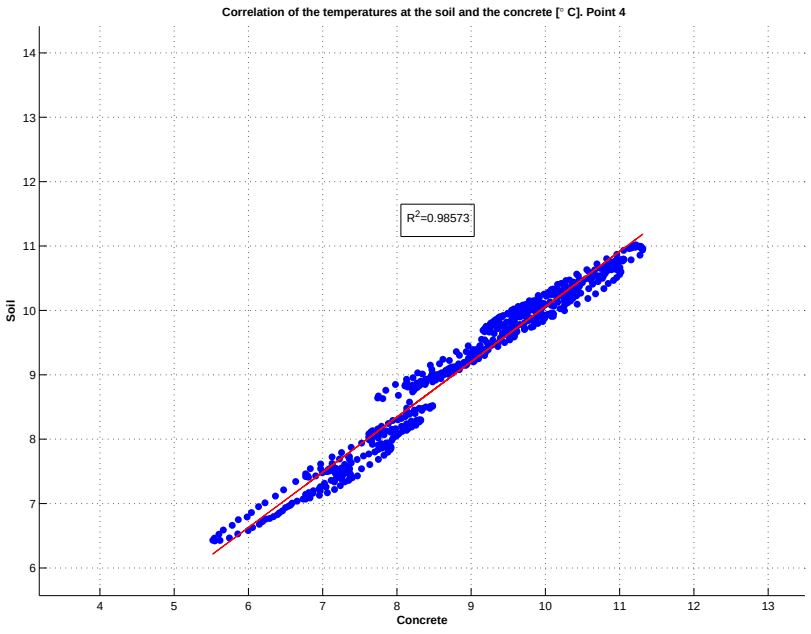

Figure A.20: Concrete vs. pipe wall. -

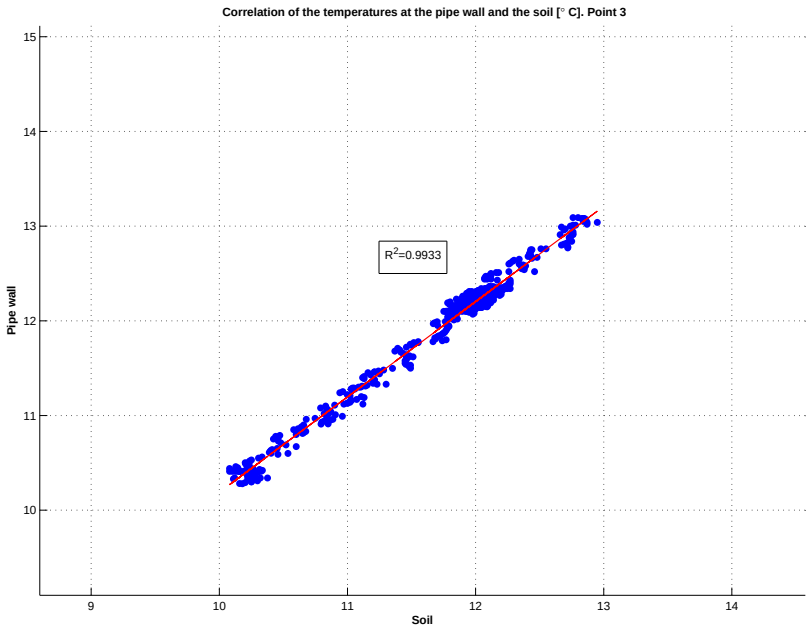

Figure A.21: Pipe wall vs. soil. -

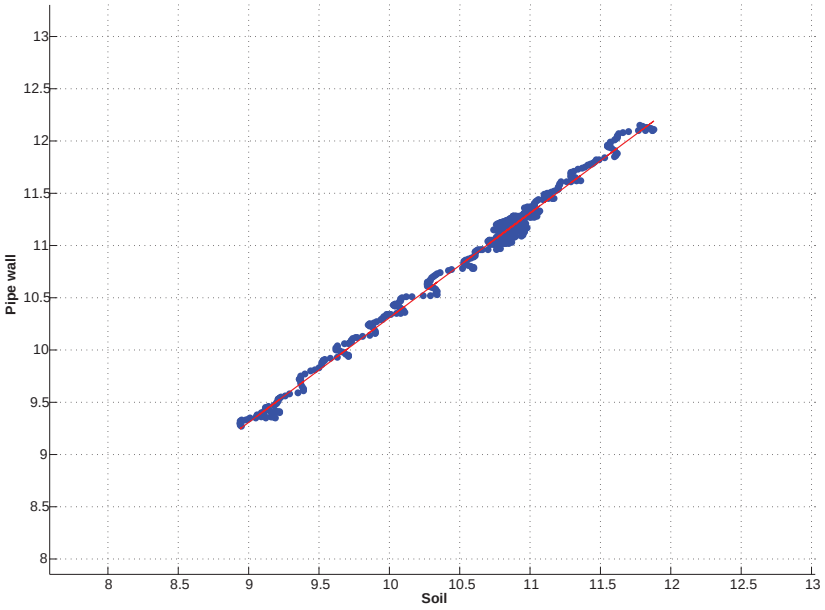

Figure A.22: Pipe wall vs. soil. -

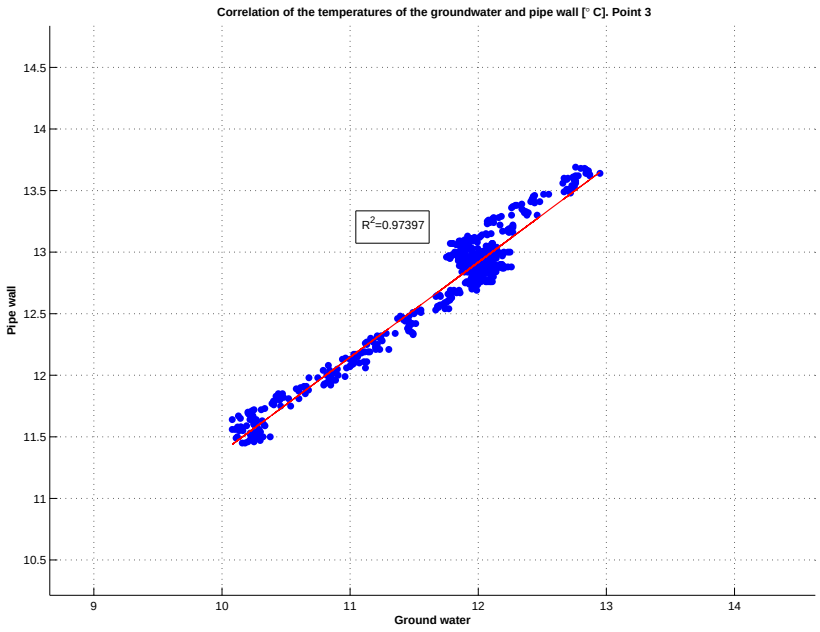

Figure A.23: Pipe wall vs. groundwater. -

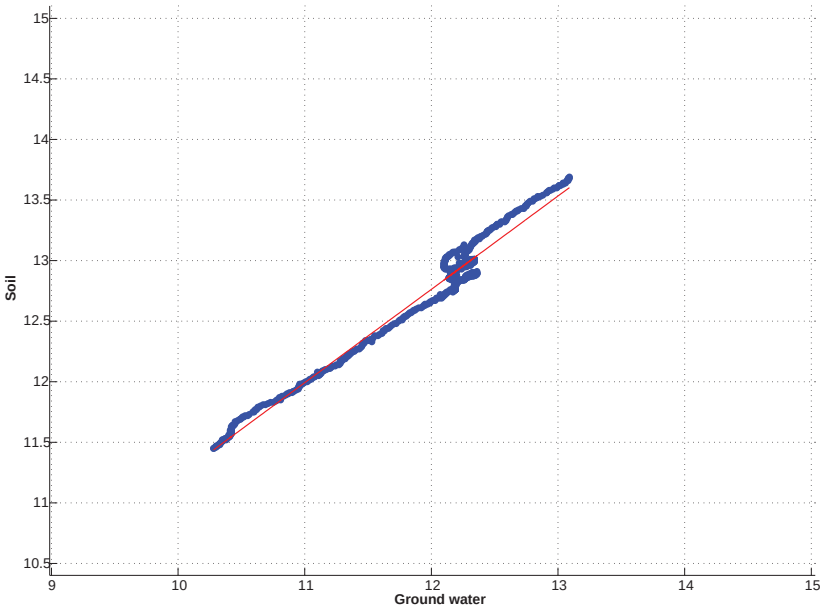

Figure A.24: Soil vs. groundwater. -

A.12 MATLAB Codes

```
function [k_soil]=Johansen75(n,theta)

unitweight= 2.7e3;                    %density {kg/m3]
q = 0.92;                             %quartz content
Sr= theta./n;                         %degree of saturation
densitydry= (1-n)*unitweight;
ex = (n-theta);
kdry = ((0.135*densitydry)+64.7)/(2700-(0.947*densitydry));
ki = 2.2;                             %thermal conductivity of ice [W/m/K]
kw = 0.57;                            %thermal conductivity of water [W/m/K]
kq = 7.7;                             %thermal conductivity of quartz [W/m/K]
if q > 0.2;
   ko =2.0;                           %thermal conductivity of other minerals [W/m/K]
else
   ko =3.0;                           %thermal conductivity of other minerals [W/m/K]
end
ks = kq^(q)*ko^(1-q);                 %thermal conductivity of solids [W/m/K]
ksat = ks^(1-n).*ki.^(ex).*kw.^(ex);
if  Sr>0.05 ;
   Ke=0.7*log(Sr)+1;                  %Kersten number
else
    Ke=log(Sr)+1;
end
k_soil = (Ke.*(ksat-kdry))+kdry;
end
```

Figure A.25: MATLAB code to calculate the conductivity based on (Peters-Lidard, 1998) -

```
%discretization
%%%soil layers
z_gnd     = [0:0.05:2.50]';            % [m]      soil grid levels
%%%timestep hours
dt=10*60;                              % [min]    timestep minutes
dz=0.05;                               % [m]      spatial (depth) step (m)

%set start and end of simulation
Tstart    = datenum('07.11.2009 24:00','dd.mm.yyyy HH:MM');
Tend      = datenum('05.12.2009 23:00','dd.mm.yyyy HH:MM');
Tmodel=Tstart:(1/(24*60)):Tend;

%%%surface characteristics

%calculating the thermal capacity of the skin
eps_concrete=0.91;                     % [-]      emisivity
c_concrete=1.51e3;                     % [J/kg/K]  specific heat capacity
rho_concrete=1.2e3;                    % [kg/m3]   density
k_concrete=2.11;                       % [W/m/K]   thermal conductivity at 25C
C_concrete=c_concrete*rho_concrete;    % [J/m3/K]  thermal capacity

%calculating the thermal capacity of the skin %assume soil moisture profile %ground water table at 0.95 m
%soil moisture content under the asphalt 0.2*porosity
%exponential decay
n=0.1; % porosity
exponent=log(0.1*n/n)/0.75;
theta=n-0.1*n*exp((z_gnd).*exponent); %water content

%calculating the thermal capacity of the soil
rho_soil =2.65e3;                      % [kg/m3]   soil density
rho_w =1.0e3;
c_soil=1.942e3;                        % [J/kg/K]  the mass specific heat of the soil
c_w=4.186e3;
% C_soil=c_soil*rho_soil;              % [j/m3/K]   thermal capacity
C_soil=c_soil*rho_soil+c_w*rho_w*(theta);
% k_soil=5;
k_soil=Johansen75(n, theta);           % [W/m/K]thermal conductivity

%%%estimation of heat capacities and thermal conductivties in the profile %with 0.1m thick concrete tile
C=NaN(length(z_gnd),1);
% C(1:2)=C_concrete;
C(1:end)=C_soil;
k=NaN(length(z_gnd),1);
% k(1:2)=k_concrete;
k(1:end)=k_soil(1:end);%(3:end);

%load initial values load('T_obs_101.mat')
%soil temperature
Tsoil=NaN(length(z_gnd),length(Tmodel));
G=NaN(length(z_gnd)-1,length(Tmodel));
%set boundary conditions %assume toplayer has surface temperature
Tsoil(1,:)=Sensor51_I;

%assume there is a temperature of the pipe wall at 0.5m %depth
% Tsoil(10,:)=Sensor31_I;

%assume there is a temperature of the groundwater at 0.7m %depth
Tsoil(end,:)=gwttemperature1_I;

%set initial conditions assume exponential decay from T(1,1) to groundwater at 0.70m %determine exponential decay
xponent=log(gwttemperature1_I(1,1)/Sensor51_I(1,1))/0.05;
% Tsoil(:,1)=Sensor51_I(1,1).*exp(z_gnd);
Tsoil(:,1)=Sensor51_I(1,1).*exp(xponent*z_gnd);

%ground flux
for t=2:length(Tmodel)
    G(:,t)=k(2:end).*(Tsoil(1:end-1,t-1)-Tsoil(2:end,t-1))./dz;
    Tsoil(2:end-1,t)=Tsoil(2:end-1,t-1)+(G(1:end-1,t)-G(2:end,t)).*dt./(dz*C(2:end-1));
end
```

Figure A.26: MATLAB code to calculate the soil temperature based on (Peters-Lidard, 1998) -

```
[TITLE]
Temperature exchange with pipe wall for the average soil temperature on 15/11/09-22/11/09.
Sources changed into flowpaced as results were high. Nusselt from D-B.

[OPTIONS]
 AREA_UNITS M2          ;Surface concentration is mass/m2
 RATE_UNITS MIN         ;Reaction rates are temperature/s
 SOLVER    RK5         ;5-th order Runge-Kutta integrator
 COUPLING   FULL
 TIMESTEP   10          ;60 sec (1 min) solution time step
 RTOL      0.001       ;Relative concentration tolerance
 ATOL      0.0001      ;Absolute concentration tolerance

[SPECIES]
 BULK T_water   C       ;Temperature in Celsius
 WALL T_wall    C       ;Temperature in Celsius

[COEFFICIENTS]
 CONSTANT b      -0.0002   ;Average temperature at wall / ground = 11.34 C
 CONSTANT Pr     9         ;Prandtl number, water at 10 C
 PARAMETER alpha           ;temperature diffusivity coefficient, water 10C

[TERMS]
 Nu  0.027 * Pr^0.33 * Re^0.8 ;Nusselt number for Re > 2300
; underestimate for laminair flow, in this case only one of 1440 Re < 2300, 8 times Re < 4000
 kk  4*alpha*Nu/D^2       ;constant in rate equation

[PIPES]
  ;Temperature of water
 RATE   T_water   kk*(T_wall - T_water)
 RATE   T_wall    T_wall + (b*T_wall)

[TANKS]
 RATE   T_water   kk*(T_wall - T_water)

[SOURCES]

 MASS  A132634  T_water  1 T1WC
 MASS  A048193  T_water  1 T3WC
 MASS  A060447  T_water  1 T4WC


[QUALITY]
;Initial conditions (= 0 if not specified here)
GLOBAL  T_water   10.97
NODE A044088  T_water     10.96
NODE A044872  T_water     11.28
...
[PARAMETERS]
     1 alpha      1.20E-07
B052348 alpha          1.20E-07
B052349 alpha          1.20E-07
...
[PATTERNS]
T1W1            1.01    1.02    1.02    1.02    1.03    1.03
T1W1            1.03    1.02    1.02    1.01    0.99    0.98
...
```

Figure A.27: MATLAB code to calculate the network temperature based on (Rossman, 2000) -

A.13 Modelled Water Residence Times

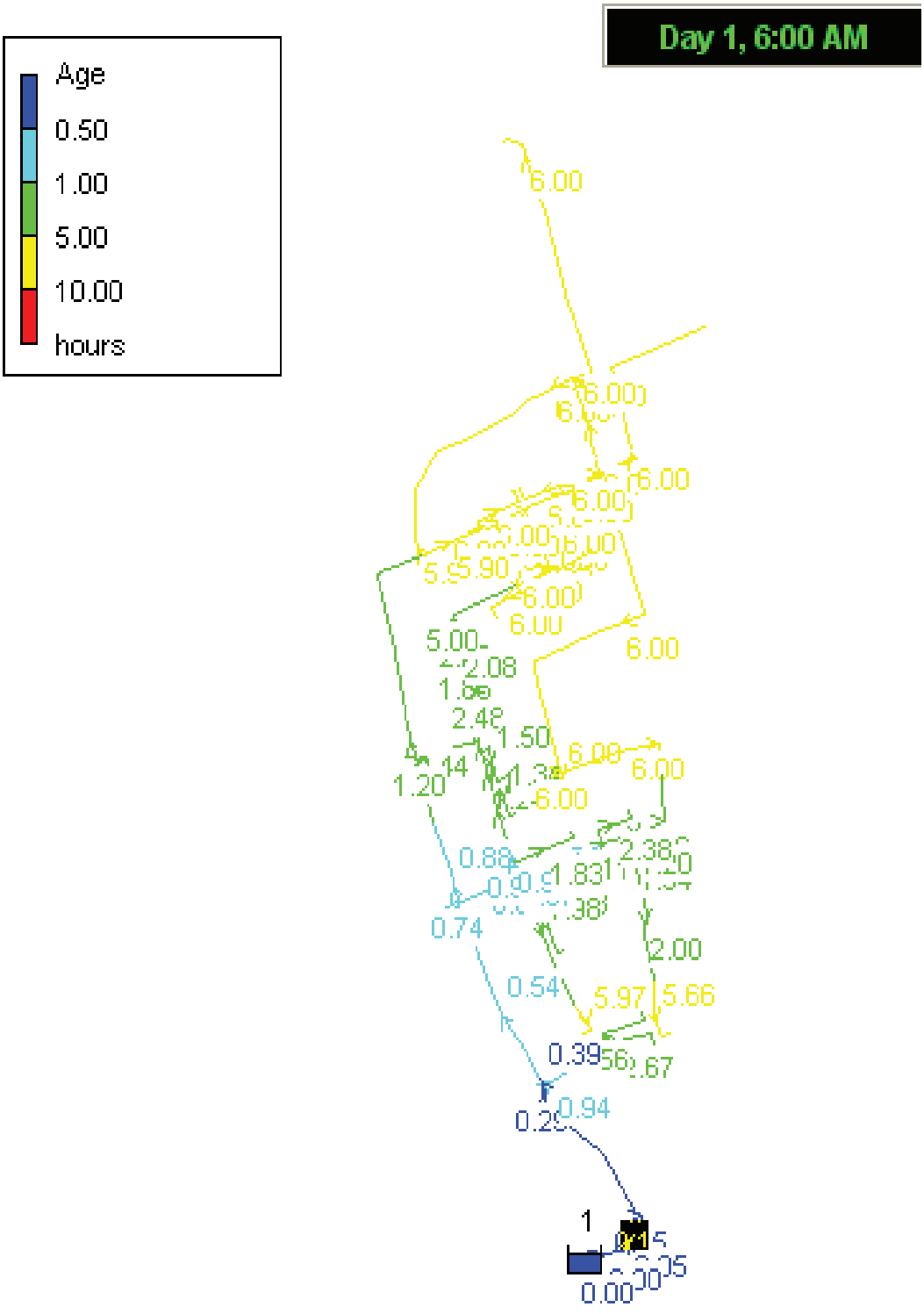

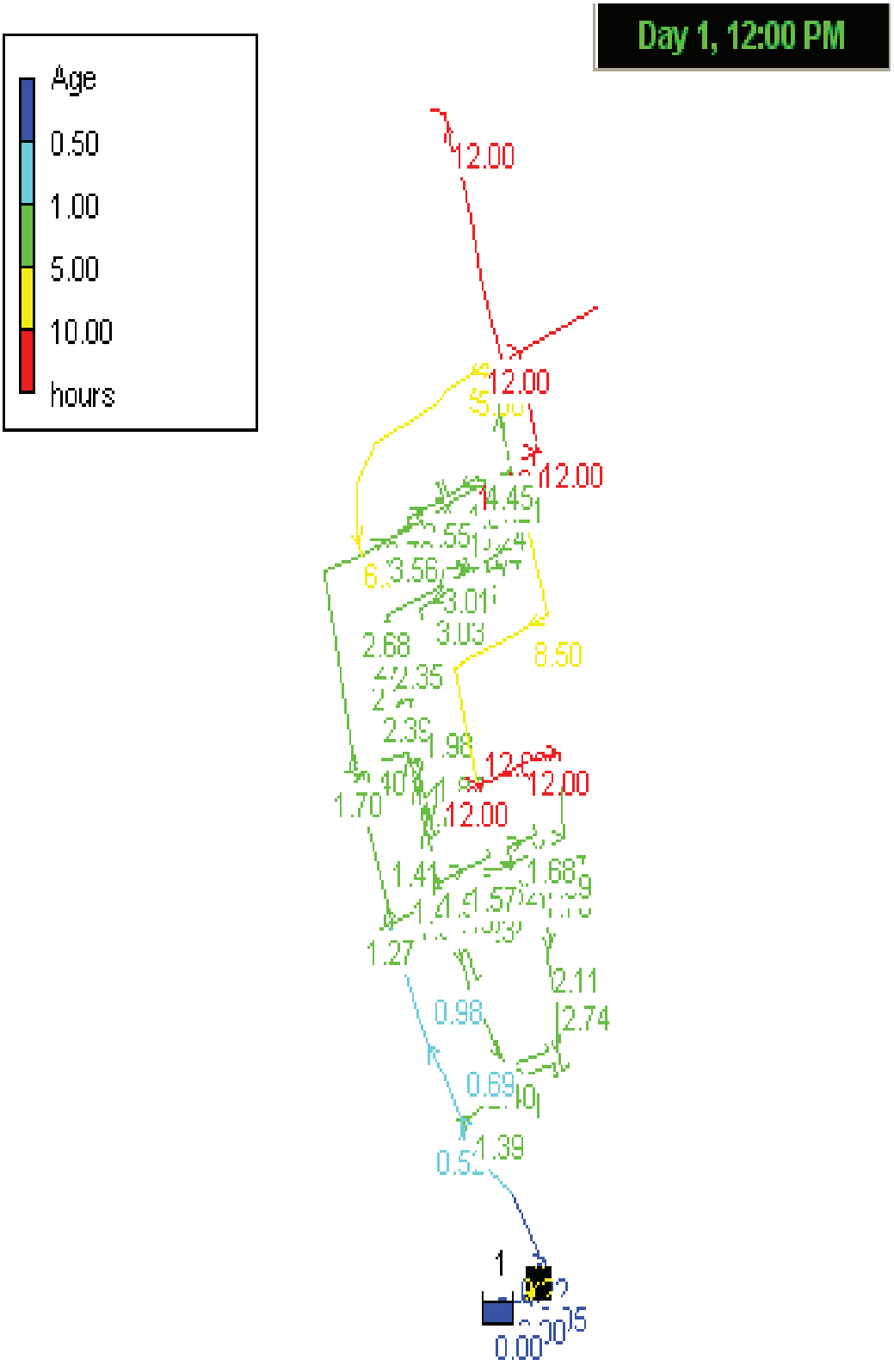
Day 1, 12:00 PM
Age
0.50
1.00
5.00
10.00
hours
12.00
12.00
12.00
4.45
3.56
3.01
3.03
2.68
2.35
8.50
1.98
12.00
12.00
1.70
1.41
1.68
1.57
1.27
2.11
2.74
0.98
0.69
1.39
0.52
1
0.00

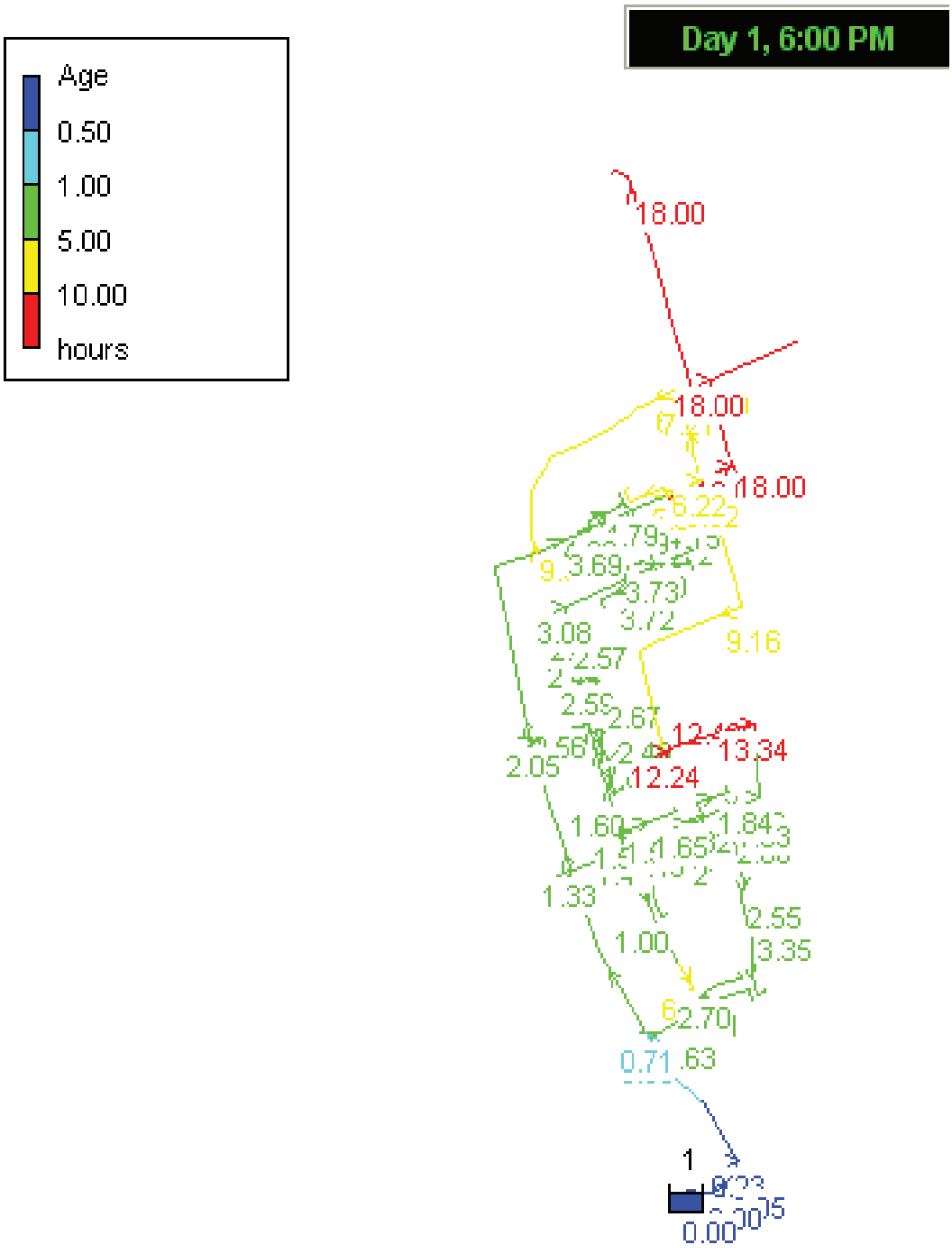
Age
0.50
1.00
5.00
10.00
hours
Day 1, 6:00 PM
18.00
18.00
18.00
9.16
13.34
12.24
2.05
1.33
1.00
3.35
2.55
0.71
1
0.00

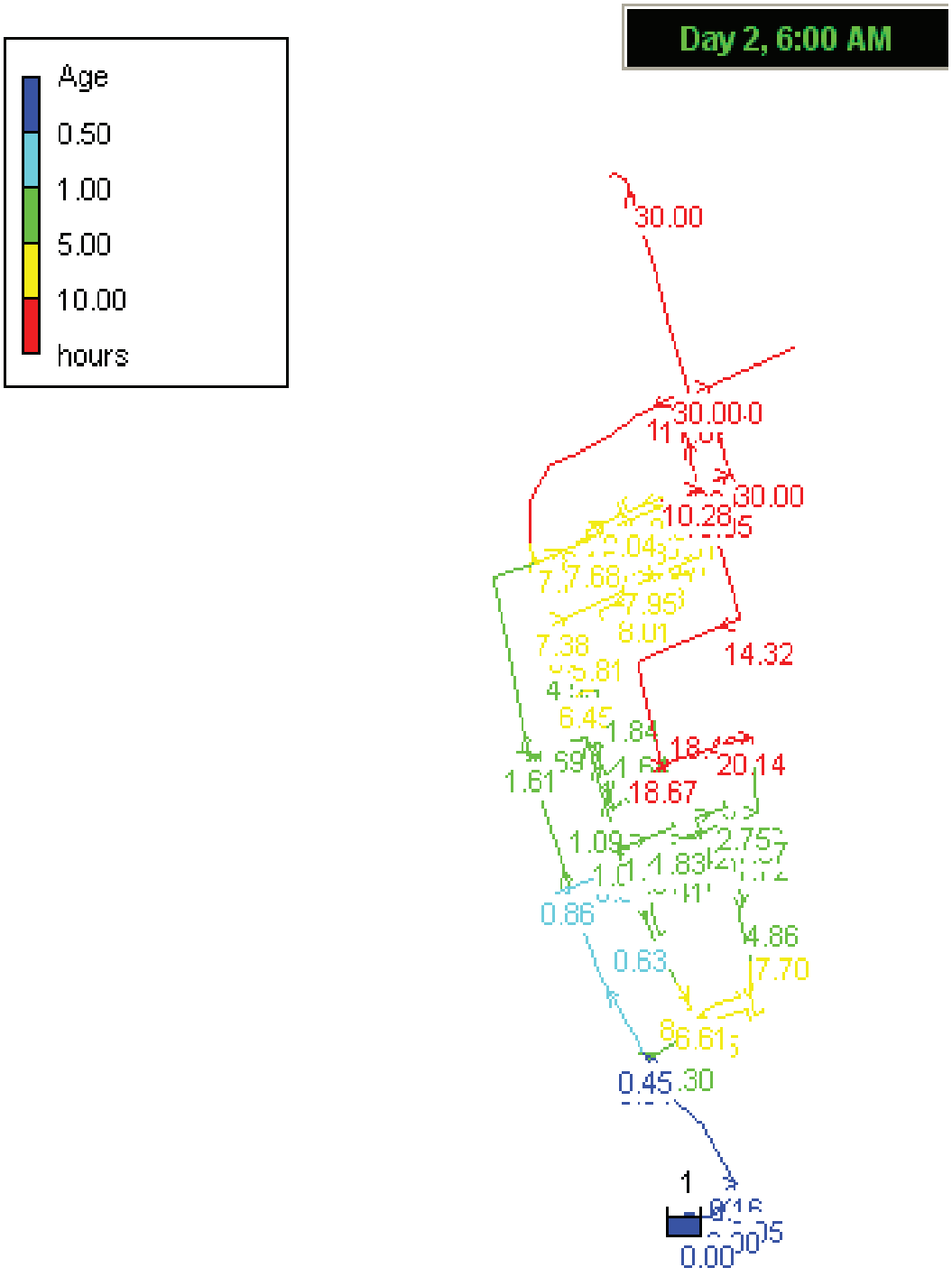
Age
0.50
1.00
5.00
10.00
hours
Day 2, 6:00 AM
30.00
30.00
30.00
10.28
14.32
20.14
18.67
1.61
1.09
0.86
0.63
4.86
7.70
0.45
0.00

List of Figures

List of Tables

List of Symbols

Latin upper case

A	Area, m^2
A_o	Amplitude of the sinusoidal temperature variation, °C,K
C	Volumetric heat capacity of soil, $\mathrm{J/m^3\ K}$
C_D	Drag coefficient, -
D	Diameter, m
D_h	Thermal diffusion coefficient, $\mathrm{m^2/s}$
D	Diffuse solar radiation, $\mathrm{W/m^2}$
E	Thermal plus mechanical energy, J; emissive power, $\mathrm{W/m^2\ \mu m}$
E^{tot}	Total energy, J
$\dot{E}_g$	Rate of energy generation, W
$\dot{E}_{in}$	Rate of energy transfer into a control volume, W
$\dot{E}_{out}$	Rate of energy transfer out a control volume, W
$\dot{E}_{st}$	Rate of increase of energy stored within a control volume, W
Gr	Graetz number, -
I	Thermal inertia, $\mathrm{J/m^2\ K\ s^{0.5}}$
K^*	Net shortwave radiation, $\mathrm{W/m^2}$
$K\uparrow$	Reflected solar radiation, $\mathrm{W/m^2}$
$K\downarrow$	Global solar radiation, $\mathrm{W/m^2}$
L	Characteristic length, m
L^*	Net longwave radiation, $\mathrm{W/m^2}$
$L\uparrow$	Upward terrestrial radiation, $\mathrm{W/m^2}$
$L\downarrow$	Downward atmospheric radiation, $\mathrm{W/m^2}$
Nu	Nusselt number, -
P	Perimeter, m, population, [cap]
P_{atm}	Atmospheric pressure, Pa
P_o	Reference atmospheric pressure, at sea level, Pa
Pr	Prandtl number, -
Re	Reynolds number, -
$R_{c,t}$	Thermal contact resistance, $\mathrm{K/W}$
R_g	Resistance for conduction at air-surface interface, $\mathrm{s/m^2}$
S	Direct solar radiation, $\mathrm{W/m^2}$
S_r	degree of saturation, -
T	Temperature, °C,K
Q	Discharge, $\mathrm{m^3/s}$, required water supply, $\mathrm{m^3/h}$
Q^*	Net all-wave radiation, $\mathrm{W/m^2}$
Q_f	Anthropogenic heat emission, ($Qfv + Qfh + Qfm$), $\mathrm{W/m^2}$
Q_e	Latent heat flux, $\mathrm{W/m^2}$
Q_h	Sensible heat flux, $\mathrm{W/m^2}$

ΔQ_s	Net heat storage in a city, $\mathrm{W/m^2}$
ΔQ_a	Net advection into or out of the city, $\mathrm{W/m^2}$
U	Overall heat transfer coefficient, $\mathrm{W/m^2}$

Latin lower case

c	Mass specific heat of the soil, $\mathrm{J/kg\ K}$
c_h	Specific heat capacity, $\mathrm{J/kg\ K}$
d	Depth, m
e	Residual error, -
e_o	Vapour pressure, hPa
f	Pattern factor, [-]
h	Convection heat transfer coefficient , $\mathrm{W/m\ K}$
h_{RL}	Height of transition layer air column, m
k	Thermal conductivity , $\mathrm{W/m\ K}$
k_{dry}	Thermal conductivity of a dry soil , $\mathrm{W/m\ K}$
k_{sat}	Thermal conductivity of a saturated soil, $\mathrm{W/m\ K}$
k_s	Solids thermal conductivity, $\mathrm{W/m\ K}$
n	Porosity, -
r	Radius, m
r_{ah}	Aerodynamic resistance, $\mathrm{s/m}$
q	Heat transfer rate, W; quartz content, -
$\dot{q}$	Rate of energy generation per unit volume, $\mathrm{W/m^3}$
$q`$	Heat transfer per unit length, $\mathrm{W/m}$
q''	Heat flux, $\mathrm{W/m^2}$
t	Time, s
x, y, z	Rectangular coordinates, m
x_t	State variable at time step t, -
$x_{fd,t}$	Thermal entry length, m
$\hat{x}_t$	Estimate of the state variable x_t
$\bar{x}$	Sample mean, -
u	Wind velocity, $\mathrm{m/s}$
u_*	A friction wind velocity, $\mathrm{m/s}$
v	Fluid velocity, $\mathrm{m/s}$
z_H	Roughness layer hight, m

Greek lower case

α	Albedo, -
δ	Thermal boundary layer thickness, m; soil temperature variations damping depth, m
ϵ	Emissivity coefficient, -
λ	Wavelength, $\mu\mathrm{m}$
μ	Viscosity, $\mathrm{kg/s\ m}$
ψ_m	Correction function for heat, -
ψ_h	Correction function for momentum, -
ψ_{sky}	Sky view factor,
ϕ	Volume fraction, -; azimuthal angle, rad

ω	Angular frequency of the temperature variation, $\mathrm{rad/s}$
θ	Volumetric soil moisture content, -; zenith angle, rad

Constants

C_p	Specific heat capacity of air, 1.01×10^3 J/kg K
k_i	Thermal conductivity of ice, 2.2 W/m K
k_w	Thermal conductivity of water, 0.57 W/m K
κ	Von Karman constant, 0.41 -
g	Acceleration due to gravity, 9.81 m/s^2
σ	Stefan Boltzman constant, 5.67×10^{-8} W/m^2 K^4
ρ	Air density, 1.2×10^3 kg/m^3
ρ_s	Soil density, 2.7×10^3 kg/m^3
ρ_w	Water density, 1.0×10^3 kg/m^3

Subscripts

ATM	Atmosphere
RL	Roughness layer
SS	Soil surface
av	Average
D	Diameter
d	Daily
dom	Domestic
dw	Drinking water conditions
fc	Forced convection
fd	Fully developed conditions
ind	Industrial
lam	Laminar flow conditions
$0, t$	Start of a control volume at time step t
s	Surface conditions
$stag$	Stagnant water conditions
w	Weekly
$z0h$	Value of the variable at the roughness height
∞	Free stream conditions

Subscripts

‘	Fluctuating quantity

References

N.H. Abu-Hamdeh. Thermal properties of soils as affected by density and water content. *Biosystems Engineering*, 86(1):97–102, 2003.

H. Akbari, M. Pomerantza, and H. Tahaa. Cool surfaces and shade trees to reduce energy use and improve air quality in urban areas. *Solar Energy*, 70:295310, 2001.

A.J. Arnfeld and C.S.B. Grimmond. An urban canyon energy budget and its application to urban storage heat flux modelling. *Energy and Buildings*, 27:6168, May 1997.

M. Blokker and E.J. Pieterse-Quirijns. Modelling temperature in the drinking water distribution system. May 2009.

G. Bollrich. *Technische Hydromechanik 1*. Verlag Bauwesen, 2000.

L. Bouaziz. Mogelijke risico's voor de drinkwatervoorziening ten gevolge van een temperatuurverhoging van het oppervlaktewater, 2009.

W. Brutsaert. *Evaporation into the Atmosphere: Theory, History and Applications (Environmental Fluid Mechanics)*. Springer, 1982.

R. De Graaf and F. Van De Ven. Exploring the technical and economic feasibility of using the urban water system as a sustainable energy source. *Thermal Science*, 12(4):35–50, 2008.

P.J. De Moel, J.Q.J.C. Verberk, and J.C. Van Dijk. *Drinking Water.Principles and Practices*. World Scientific Publishing Co. Pte. Ltd, 2006.

E.E. Geldreich. *Microbial Quality of Water Supply in Distribution Systems*. CRC Press, 1996.

V. Gnielinski. *International Journal of Chemical Engineering*, 16(359), 1976.

F.P. Incropera and D.P. De Wit. *Fundamentals of Heat and Mass Transfer*. John Willey and Sons, fifth edition, 2002.

IPCC. Climate change 2007: Synthesis report. contribution of working groups i, ii and iii to the fourth assessment report of the intergovernmental panel on climate change. Technical report, Intergovernmental Panel on Climate Change, 2007.

W.M. Kays and H.C. Perkins. *Handbook of Heat Transfer, Fundamentals*, chapter 7. McGraw-Hill, 1985.

P. Korevaar, G. Menelik, and C. Dirksen. *Elements of soil physics*. University of Wageningen, Wageningen, the Netherlands, 1983.

REFERENCES

E. Aparicio Medrano. M. sc. thesis: Urban surface water as energy source and collector, 2008.

R.C. Neville. *Solar Energy Conversion*. Elsevier, second edition, 1995.

B. Offerle, C.S.B. Grimmond, and T.R. Oke. Parametrization of net all-wave radtiation for urban areas. *Journal of Applied Meteorology*, 42:1157–1173, 2003.

T.R. Oke. Canyon geometry and the nocturnal urban heat island. comparison of scale model and field observations. *International Journal of Climatology*, 1:237–254, 1981.

T.R. Oke. The energetic basis of the urban heat island. *Royal Meteorological Society Quarterly Journal*, 108(455): 1–24, 1982.

T.R. Oke. Urban climates and global environmental change. *Applied Climatology: Principles and Practice*, pages 273–287, 1997.

C. D. Peters-Lidard. The effect of soil thermal conductivity parameterization on surface energy fluxes and temperature. *Civil and Environmental Engineering*, 1998.

L.A. Rossman. *Epanet 2, Users Manual*. U.S. Environmental Protection Agency, Cincinnati, OH, 2000.

M. Rutten. M. sc. thesis: Forecasting cooling water problems in the river rhine, 2006.

H.H.G. Savenije. *CT4431.Hydrological Modelling*. Delft University of Technology, 2007.

S.E. Schwartz. Heat capacity, time constant, and sensitivity of earth's climate system. *Atmospheric Science Division, Brookhaven National Laboratory*, 2007.

E.N. Sider and G.E. Tate. *Industrial Engineering Chemistry*, 28(1429), 1936.

M. Slesser. *Dictionary of Energy*. Schocken Books, New York, 1982.

S.C. Steele-Dunne, M.M. Rutten, D.M. Krzeminska, M. Hausner, S.W. Tyler, T.A. Bogaard, and N.C. van de Giesen. Feasibility of soil moisture estimation using passive distributed temperature sensing. *Water Resources Research*, 46, 2010.

J. Van De Vossenberg, P.W.J.J. Van Der Wielen, and D. Van Der Kooij. Literatuurstudie naar opportunistisch-ziekteverwekkende micro-organismen die zich kunnen vermeerderen in drinkwater. Technical Report BTO(s) 2009.001, Kiwa Water Research, 2009.

M. Van Der Molen, H. Kooi, E.F.P.A. Smulders, and S.G.J.Heijman. Warmteindringing in de bodem. Technical Report BTO 2008.053, Kiwa Water Research, 2008.

Waterleidingbesluit, 1960.

R.H.S. Winterton. *International Journal of Heat Mass Transfer*, 41(809), 1998.

WMO. *Guide to Meteorological Instruments and Methods of Observation*. Chairperson, Publications Board, World Meteorological Organization (WMO), seventh edition, 2008.

J.J.G. Zwolsman. Impacts of climate change on river water quality and drinking water production in the netherlands. Technical Report L806, Kiwa Water Research, 2008.